The Pennsylvania State University

The Graduate School

Department of Mechanical and Nuclear Engineering

REACTIVE MOLECULAR DYNAMICS SIMULATIONS OF LITHIUM SECONDARY BATTERIES - INTERFACES AND ELECTRODES

A Dissertation in

Mechanical Engineering

by

Md Mahbubul Islam

Submitted in Partial Fulfillment
of the Requirements
for the Degree of

Doctor of Philosophy

December 2016

The dissertation of Md Mahbubul Islam was reviewed and approved* by the following:

Adri C.T. van Duin
Professor of the Department of Mechanical and Nuclear Engineering
Dissertation Advisor
Chair of Committee

Donghai Wang
Associate Professor of the Department of Mechanical and Nuclear Engineering

Hosam Fathy
Associate Professor of the Department of Mechanical and Nuclear Engineering

Lasse Jensen
Professor of the Department of Chemistry

Karen A. Thole
Professor of Mechanical Engineering
Head of the Department of Mechanical and Nuclear Engineering

*Signatures are on file in the Graduate School

ABSTRACT

Over the last two decades, lithium-based batteries have revolutionized the energy storage technologies. Li-ion batteries have found widespread use in portable electronics and electric vehicle applications. However, a detailed understanding of the battery chemistry, especially the formation of a solid electrolyte interphase (SEI)—a thin passivation layer which is generated during the first charge cycle due to the reduction of electrolytes—is still elusive. The mass scale commercialization of electric vehicles requires the storage capacity beyond the conventional Li-ion batteries, which spurred research interests towards Li-S technologies. Li-S batteries are attractive for their very high capacity and energy density, but their commercial application has been thwarted due to several critical limitations stemming from electrolyte dissociation chemistry and electrode material properties. To investigate the current issues associated with the Li-ion and Li-S batteries and to find possible countermeasures, we used both a newly developed computational tool eReaxFF and the standard ReaxFF reactive molecular dynamics simulations in the following research areas:

1) We developed a computational method, eReaxFF, for simulating explicit electrons within the framework of the standard ReaxFF reactive force field method. We treat electrons explicitly in a pseudoclassical manner that enables simulation several orders of magnitude faster than quantum chemistry (QC) methods, while retaining the ReaxFF transferability. We describe in this thesis the fundamental concepts of the eReaxFF method, and the integration of the Atom-condensed Kohn-Sham DFT approximated to second order (ACKS2) charge calculation scheme into the eReaxFF. We trained our force field to capture electron affinities (EA) of various species. As a proof-of-principle, we performed a set of molecular dynamics (MD) simulations with an explicit electron model for representative hydrocarbon radicals. We establish a good qualitative agreement of EAs of various species with experimental data, and MD simulations with eReaxFF agree well with the corresponding Ehrenfest dynamics simulations. The standard ReaxFF

parameters available in literature are transferrable to the eReaxFF method. The computationally economic eReaxFF method will be a useful tool for studying large-scale chemical and physical systems with explicit electrons as an alternative to computationally demanding QC methods.

2) A detailed understanding of the mechanism of the formation of SEI is crucial for designing high capacity and longer lifecycle lithium-ion batteries. The anode side SEI is primarily comprised of the reductive dissociation products of the electrolyte molecules. Any accurate computational method to study the reductive decomposition mechanism of electrolyte molecules is required to possess an explicit electronic degree of freedom. In this study, we employed our newly developed eReaxFF method to investigate the major reduction reaction pathways of SEI formation with ethylene carbonate (EC) based electrolytes. In the eReaxFF method, a pseudo-classical treatment of electrons provides the capability to simulate explicit electrons in a complex reactive environment. Our eReaxFF predicted simulation results of the EC decomposition reactions are in good agreement with the quantum chemistry data available in literature. Our MD simulations capture the mechanism of the reduction of the EC molecule due to the electron transfer from lithium, ring opening of the EC to generate EC^{-}/Li^{+} radicals, and subsequent radical termination reactions. Our results indicate that the eReaxFF method is a useful tool for large-scale simulations to describe redox reactions occurring at electrode-electrolyte interfaces where quantum chemistry based methods are not viable due to their high computational requirement.

3) Li-S batteries still suffer several formidable performance degradation issues that impede their commercial applications. The lithium negative electrode yields high anodic capacity, but it causes dendrite formation and raises safety concerns. Furthermore, the high reactivity of lithium is accountable for electrolyte decomposition. To investigate these issues and possible countermeasures, we used ReaxFF reactive molecular dynamics simulations to elucidate anode-electrolyte interfacial chemistry and utilized an *ex-situ* anode surface treatment with Teflon coating. In this study, we employed Li/SWCNT (single-wall carbon nanotube) composite anode instead of

lithium metal and tetra (ethylene glycol) dimethyl ether (TEGDME) as electrolyte. We find that at a lithium rich environment of the anode-electrolyte interface, electrolyte dissociates and generates ethylene gas as a major reaction product, while utilization of Teflon layer suppresses the lithium reactivity and reduces electrolyte decomposition. Lithium discharge from the negative electrode is an exothermic event that creates local hot spots at the interfacial region and expedites electrolyte dissociation reaction kinetics. Usage of Teflon dampens initial heat flow and effectively reduces lithium reactivity with the electrolyte.

4) Sulfur cathodes of Li-S batteries undergo a noticeable volume variation upon cycling, which induces stress. In spite of intensive investigation of the electrochemical behavior of the lithiated sulfur compounds, their mechanical properties are not very well understood. In order to fill this gap, we developed a ReaxFF interatomic potential to describe Li-S interactions and performed MD simulations to study the structural, mechanical, and kinetic behavior of the amorphous lithiated sulfur (a-Li_xS) compounds. We examined the effect of lithiation on material properties such as ultimate strength, yield strength, and Young's modulus. Our results suggest that with increasing lithium content, the strength of lithiated sulfur compounds improves, although this increment is not linear with the lithiation. The dependence of the mechanical properties and failure behavior on the loading rate of the amorphous lithiated sulfur compositions was also studied. The diffusion coefficients of both lithium and sulfur were computed for the a-Li_xS system at various stages of Li-loading. A Grand canonical Monte Carlo (GCMC) scheme was used to calculate the open circuit voltage (OCV) profile during cell discharge. The calculated OCV is consistent with prior experimental results. Our ReaxFF potentials also reproduced experimentally observed volume expansion of a-Li_xS phases upon lithiation. The Li-S binary phase diagram was constructed using genetic algorithm based tools. These simulation results provide insight into the behavior of sulfur-based cathode materials that are needed for developing high-performance lithium-sulfur batteries.

TABLE OF CONTENTS

LIST OF FIGURES

LIST OF TABLES

ACKNOWLEDGEMENTS

First, I would like to express my deepest gratitude to my incredible advisor, Prof. Adri van Duin, for his excellent mentorship and guidance. His support, inspiration and scientific input throughout the course of this research work were invaluable. Working with him has always been an honor and pleasure for me. I am thankful for his kind patience over the period and for putting his trust on me when it was most needed. In future, I hope to treat my students with the same level of compassion, kindness and respect that he has shown towards me.

I would like to thank my Ph.D. committee members Donghai Wang, Hosam Fathy, and Lasse Jensen for their time and valuable insights to help augment the quality of this work. I also like to acknowledge my collaborators Oleg Borodin and Marco Olguin from the Army Research Lab and Grigory Kolesov from the Harvard University. I gratefully thank my summer intern mentor Sumathy Raman for her mentorship during and post internship periods.

I want to express my gratitude and deepest appreciation to my elder brother, Mahmudul. You were always a shoulder-to-cry-on, someone to talk to whenever I needed any suggestions. Undoubtedly, I couldn't think big without your thoughtful guidance. Your advices since my elementary school has always been a beacon in my journey. Thank you vaiya for all of your support! I am extremely thankful and grateful to my parents for their patience, support, and unconditional love. You are my greatest source of inspiration and driving force to step ahead. I extend my sincere gratitude to my incredible siblings for their support to achieve my goal. I really feel blessed to have such love and care from my family members. I am grateful to my wonderful niece for her time to provide me much-needed distractions and accompanying me through the instant messaging. Thank you Seenthia!

My experience at PSU could not have been more enjoyable without my friends at State College. I am especially grateful to my roommates Mamun, Faruk, and Masud. Thank you guys for

accompanying me on this amazing journey. You were always excellent and made my life more meaningful at State College. You all will be dearly missed!

I am surely blessed to have a lot of friends since my childhood, who are now, in reality, spread over the continents; however, I never felt we are 'really' separated. Nirjhor, my close confidant, for any crucial decision making, I never felt I am alone, you were always on my side for any consultation or advice. Thank you for your support! Whenever I felt apathetic, a phone call to Hamim would give me a new motivation to move on. Thanks dost! I gratefully acknowledge generous supports and scientific discussions with Chowdhury. I also like to thank all my friends back home; their inspirations were always a big motivation for me. I am thankful to the BSA-PSU community for the support and to make my life little more 'engaging' during my stay at State College.

My labmates were always awesome, without their kind assistance I would surely have to struggle a lot. I gratefully acknowledge kind assistance from Kaushik and Sriram. I thank Chenyu for helping me to find my summer internship at ExxonMobil. I would like to thank Jonayat, Joon, Alireza, and Sungwook for their kind support.

Finally, my utmost gratitude goes to the Almighty God for the wisdom, healthy life, and strength with which He has endowed me to conduct my research works over the course of my Ph.D. study.

Chapter 1

Introduction

1.1 Motivation

Ever-increasing energy demand along with the technological advancements is raising concerns over the current storage of fossil fuels and their detrimental impact on the environment. During the last two centuries, the world's dependence on fossil fuels has become a primary cause of increasing carbon dioxide level in the atmosphere. Issues like climate pollution, global warming, rapidly diminishing fossil fuel sources are forcing the current civilization to exploit unlimited resource of renewable energies, such as solar and wind.[1] Moreover, in order to bring forth diversification of energy resources, as well as having zero local emissions and to improve urban air quality, all electric and plug-in hybrid electric vehicles (EV), and renewable energy based 'smart' grids have become an evident necessity. The internal combustion engines are known as a major source of urban air pollution caused by the combustion of gasoline.[2] In this regard, EV technologies are being considered as a viable alternative to power the transport sector to mitigate environmental degradation. However, the key component to impact the EV technology is the battery, which yet need to satisfy the requirements of the driving range, safety, and cost. Therefore, rechargeable energy storage device technologies are evolving as a major technological challenge.[3] At present, among the myriad energy storage technologies, lithium batteries are the principal contender for the automotives and 'smart' grids. However, batteries with higher energy density, enhanced safety and longer cycling life than the existing lithium-ion technology are needed for large-scale applications.[4]

1.2 What is a Battery?

A battery is a device consisting of one or more electrochemical cells that transforms stored chemical energy into electrical energy. Each cell consists of a positive (cathode) and a negative (anode) electrode, separated by an electrolyte solution (an ionic conductor which is also an

electronically insulating medium) containing dissociated salts.[5] The electrical energy stored in a battery is the product of capacity and voltage and is determined by the cell electrochemistry and electrode material properties.[6] The electrical energy delivered from a cell is contingent on the change in free energy due to chemical reactions that occur during cell discharging. Key components of a typical battery are shown in Figure 1-1. During discharging, electrons are released from the anode and flow towards the cathode through the external circuit, while at the same time, ion transport across the electrolyte from the anode to the cathode ensures electro-neutrality. In general, batteries are classified into two broad categories: primary batteries that irreversibly transform chemical energy to electrical energy, which are used once and disposed, and secondary batteries are rechargeable and can be used multiple times.

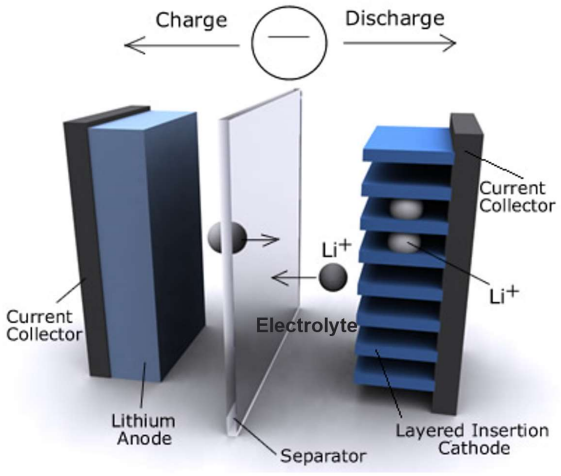

Figure 1-1 Schematic of the components of a Li secondary battery.

(http://www.sunrisegolfcarts.com/Lithium-vs-SLA-Batteries-Article-s/1957.htm)

1.3 History of Rechargeable Batteries

The earliest commercial primary (non-rechargeable) lithium batteries were introduced in the 1970s with a 3V lithium metal as an anode.[7] Li metal was favored as an anode material because it is the most electropositive (–3.04 V versus standard hydrogen electrode), lightest (equivalent

weight=6.94 $gmol^{-1}$, and specific gravity =0.53 gcm^{-3}) metal. In 1972, Whittingham at Exxon launched a rechargeable battery project using layered TiS_2 and Li metal as a positive, and a negative electrodes, respectively, and lithium perchlorate in dioxolane as electrolytes. Despite a superior performance of the layered cathode material, the battery encountered severe shortcomings from a Li-metal/liquid electrolyte combination because of the deleterious Li-dendrite growth at the lithium metal anode during electrodeposition, which led to the hazard of catastrophic fire.[7] A breakthrough in the Li- battery technology has been achieved in the late 1970s with the discovery of a passivating layer at the anode-electrolyte interface. When Li- metal comes in contact with the organic solvents, it forms a thin film, which is a primary reason for the stability of the batteries. In 1979, Peled coined the term 'Solid Electrolyte Interphase' (SEI) and emphasized that the rate limiting step is the migration of lithium ions through this interfacial film. To overcome the issues of dendrite growth and safety hazard, alternate approaches for the negative electrode were investigated and which led to various other types of secondary batteries.

In the mid-1980s NiCd secondary batteries became widespread, and they began to supplant earlier generation primary and Li-metal based batteries for small electric appliances.[8] However, due to the detrimental impact of Cadmium on the environment, NiMH secondary batteries were gradually favored over NiCd batteries in the late 1980s. Over the same period, extensive research efforts performed by Goodenough et al.[9] on layered cathode materials (Li_xMO_2, where M is Co, Ni, or Mn) and Scrosati et al.[10], Murphy et al.[11] on insertion anode materials laid the foundation of modern Li-ion batteries. Finally, in June 1991, Sony Corporation commercialized the first modern $C/LiCoO_2$ Li-ion cell by exploiting the developed technology for the high performance layered cathode material and the highly reversible, low voltage Li intercalation–deintercalation based carbonaceous material.[7] Since then, compact and lightweight Li-ion batteries have been ubiquitously used in consumer electronics such as mobile phones, cameras, and laptop computers.[12] A comparison of the energy densities of commonly available rechargeable batteries is shown in

Figure 1-2. Battery technologies beyond the Li-ion batteries, for example, Na-ion, Li-air, and Zn-air are also being considered as potential candidates to meet the demand of future energy storage.

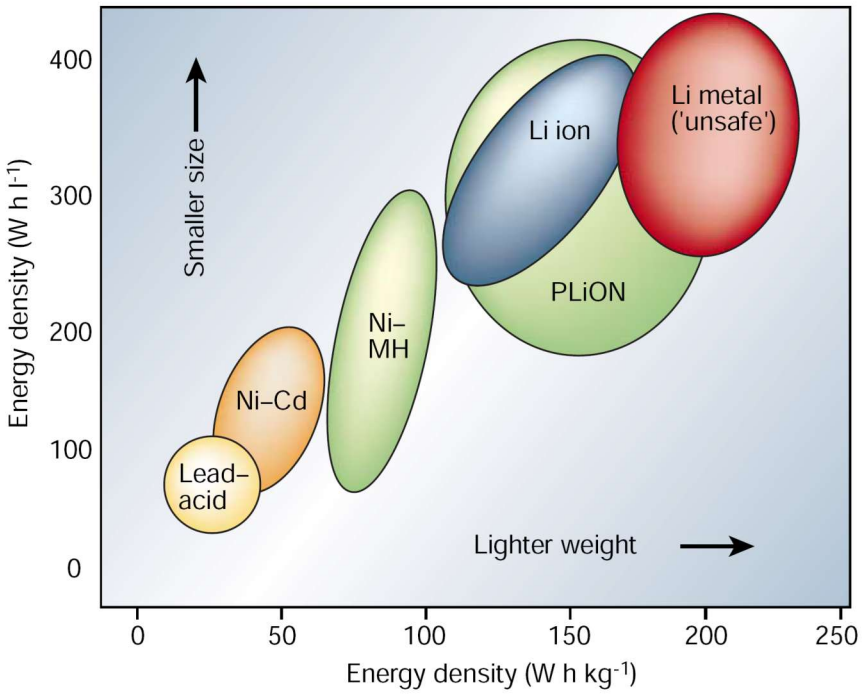

Figure 1-2 Comparison of various rechargeable battery technologies in terms of volumetric and gravimetric energy density[7]

1.4 Lithium-ion Batteries

The advancement in the Li-ion batteries achieved in the last two decades allowed their large-scale applications, such as electrification of transportation, micro grids for storing electricity generated from various renewable energy sources. The novel characteristics of the Li-metal such as (i) the lowest reduction potential of any elements yields the highest cell potential, (ii) the lightest metal available in the periodic table, enables high gravimetric and volumetric capacities for Li-based batteries. A typical commercial Li-ion battery is comprised of a transition metal oxide cathode, a graphitic anode, and carbonate-based electrolytes. Figure 1-3 represents a schematic of

a Li-ion battery system. Different subsystems of a Li-ion battery are briefly described in the following sections.

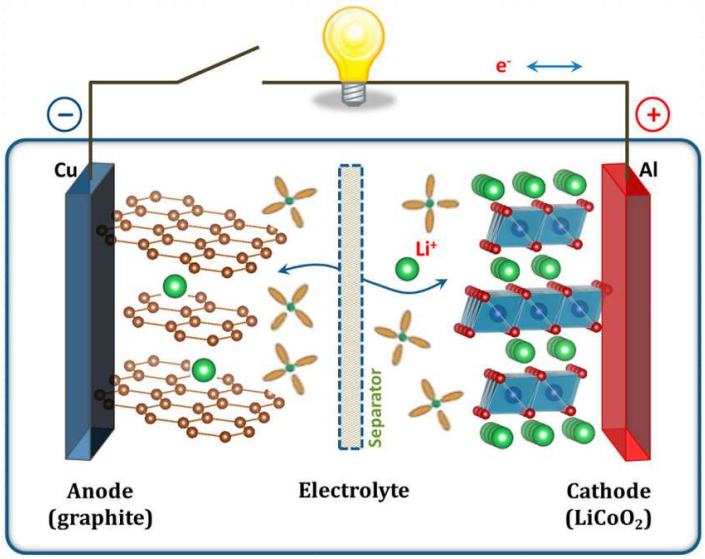

Figure 1-3 Schematic of a Li-ion battery system[13]

1.4.1 Anode Materials

Although the first generation of the Li-ion batteries were designed using Li-metal anodes, the usage of Li-metal was ceased rapidly because of the safety concerns. The carbon-based materials are the most ubiquitously used anode materials for the commercial Li-ion batteries. The process of Li-intercalation and deintercalation into graphitic material maintains its two dimensional (2D) mechanical stability. Carbon possesses attractive properties of low cost, abundance in nature and low delithiation potential vs. Li, and high Li diffusivity.[14] In the graphite anode, 1 Li atom per 6 carbon can be stored, which results in a theoretical capacity of 372 $mAhg^{-1}$. During Li intercalation, graphite undergoes around 10% increase in its interlayer spacing. Such a volume change may cause a fracture in the anode-SEI, thus degrades cell performance.

Despite the widespread use of graphitic anode materials, high capacity 'conversion type' anode material, such as Si is now under extensive scrutiny. Si has received the most attention owing

to its extremely high gravimetric and volumetric capacity, low cost, abundance, non-toxicity, and chemical stability. However, upon lithiation, silicone forms Li_xSi_y alloys, and these alloys are notorious for their colossal volume change of around 300% at a fully lithiated state.[15] Such volume change during charging-discharging destroys the SEI protective coating, and exposes fresh electrolytes to the anode, thus continuous electrolyte dissociation leads to the rapid capacity fading. The capacity of the other available anode materials is shown in Figure 1-4.

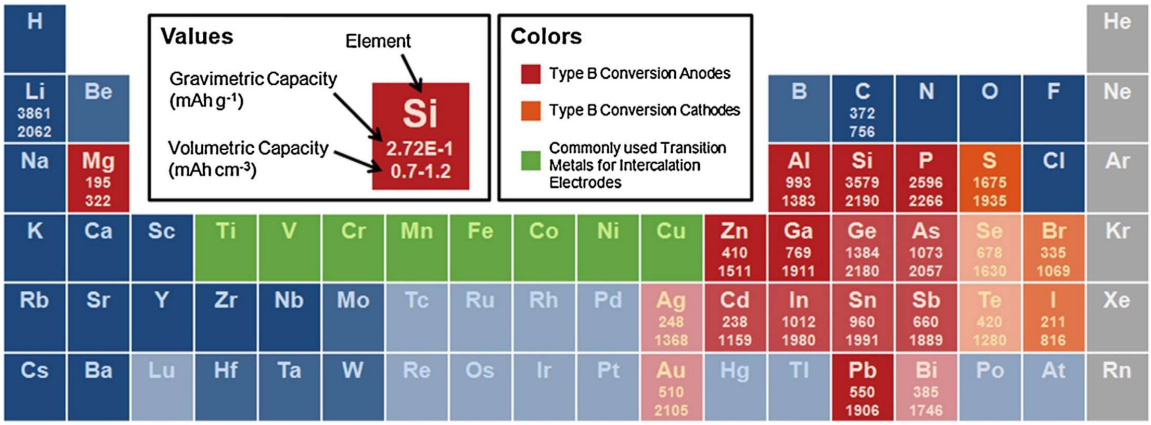

Figure 1-4 Capacities of elements that may be used as an electrode material for Li-based rechargeable batteries.[14]

1.4.2 Cathode Materials

Intercalation cathode materials are the most prevalent in LIBs. Intercalation is a process where guest atoms can be inserted into and removed from the host material reversibly without a change in the crystal structure. The intercalation compounds can be divided into several categories based on their crystal structures, such as layered, olivine, spinel and tavorite. The layered structures are the earliest and the most popular form of intercalation compounds for the cathode materials. Layered $LiCoO_2$ (LCO), with an *R3m* rhombohedral structure, has been widely used in LIBs over the last two decades, because of its relatively high theoretical specific capacity of 274 $mAhg^{-1}$, high theoretical volumetric capacity of 1363 mAh cm^{-3}, high discharge voltage, and good cycling

performance.[16] LCO also possesses a number of shortcomings, including high cost, low thermal stability, and rapid capacity fade at a high discharge rate. The higher discharge rate induces crystal distortion from the hexagonal to monoclinic symmetry leading to performance deterioration.

$LiMnO_2$ (LMO) has been studied as a potential alternative to the LCO cathode owing to its relatively lower cost and lesser toxicity. However, the application of LMO cathode has been plagued because of (i) during Li-extraction the layered structure has a tendency to convert into spinel structure and (ii) dissolution of Mn into the electrolyte solvents causes loss of Mn. Mn^{2+} is soluble in electrolytes and degrades anode SEI stability. The orthorhombic LMO with a rock salt crystal structure has a capacity of 274 $mAhg^{-1}$ in the voltage range of 2.0-4.5V.[17] Crystal structures of the various cathode materials are shown in Figure 1-5.

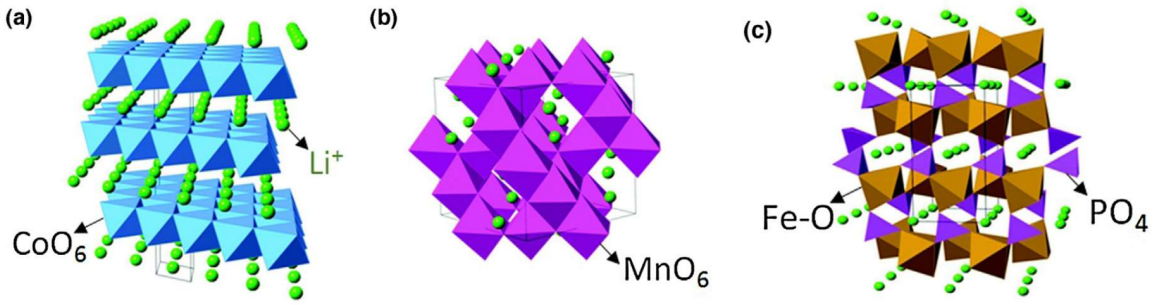

Figure 1-5 Crystal structures of representative intercalation cathodes: structure of (a) layered ($LiCoO_2$), (b) spinel ($LiMn_2O4$), (c) olivine ($LiFePO4$)[18]

The three-component Ni-Co-Mn system $Li[Ni_xCo_xMn_x]O_2$ (NCM) demonstrates excellent electrochemical properties because of the synergetic contributions from the stable electrochemical characteristics of $LiCoO_2$, high capacity of $LiNiO_2$ and the thermal stability and low cost of manganese in $LiMnO_2$. The $LiNi_{1/3}Co_{1/3}Mn_{1/3}O_2$ is the common form of NCM and is widely used in Li-ion batteries. It exhibits a superior charge/discharge characteristics that can produce batteries with a long life and enhanced safety. Although this material has a capacity similar to the $LiCoO_2$,

this combination is promising because of minimal volume change during charging-discharging, good performance, safety, and lower cost.[17]

$LiMn_2O_4$ (LMO) is a representative spinel cathode material. The LMO has received attention due to the benefits of a reduced cost, availability, and environmental friendliness of Mn. However, the long-term cyclability of LMO is hindered because of the irreversible side reactions with electrolytes, oxygen loss from the delithiated LMO, Mn dissolution, and phase transformation to the tetragonal $Li_2Mn_2O_4$ at the surface.[19] The dissolution problem can be suppressed with a surface coating of ZnO,[20] metal doping,[21] Mn-rich layered coating, and by forming a stable SEI.[22]

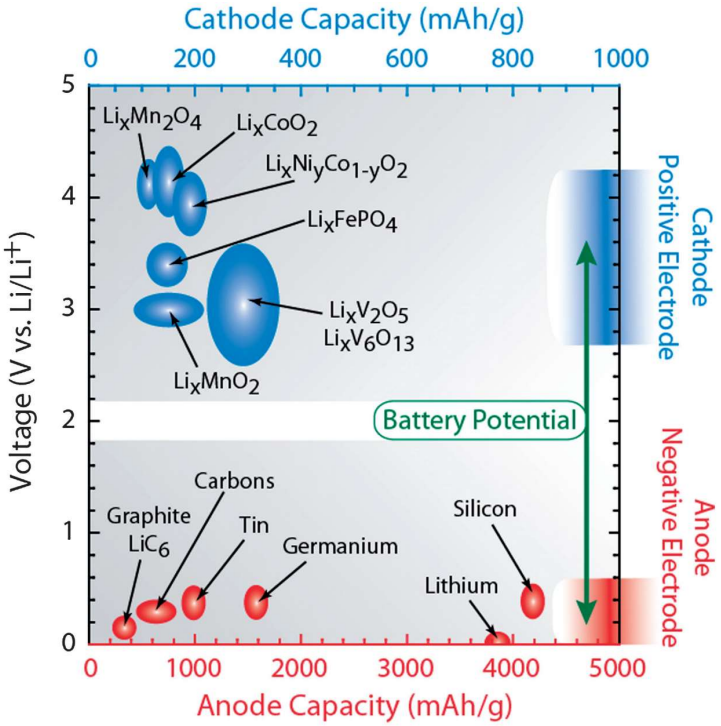

Figure 1-6 Capacity and the operating potential of various electrode materials[23]

$LiFePO_4$ (LFP) has an olivine-type of structure with a symmetry group of *Pmnb*. Iron is one of the most abundant metal in the earth crust, cheaper and more environmentally friendly than cobalt. LFP is known for its thermal and chemical stability and high power capability. The gravimetric and volumetric capacity of LFP is 170 mAh g^{-1}, and 589 mAh cm^{-3}, respectively.[14] The

disadvantage of the LFP is a low electronic conductivity and slow diffusion of Li-ions, and a relatively low average voltage of 3.4V. The lower ionic and electronic conductivity can be improved by reducing LFP particle size and coating with various conducting agents such as carbon or silver nanoparticles. The lower operating cell potential is advantageous to prevent electrolyte decomposition, thus maintains high energy density and stable cycling. The charging (delithiation) reduces the volume of LFP by approximately 6.8%, which is compatible with the increase in the volume of the graphitic anode material.[17] The capacity of the available cathode materials is shown in Figure 1-6.

1.4.3 Electrolyte Solvents

Typical compositions of LIB electrolytes are based on the mixture of two or more organic solvents and solutions of one or more lithium salts. The mixed solvent formulation is required because of the diverse and often contradicting requirements of the electrolyte properties which can hardly be satisfied by any individual compound, for example, high dielectric constant versus high fluidity. Therefore, to obtain various properties simultaneously, solvents of very different physical and chemical natures are often used together. A suitable electrolyte should have characteristics of good ionic conductivity, high chemical stability, low cost, and safety. Solvents with low melting point, high boiling point, low vapor pressure, low viscosity, and ability to dissolve salts to sufficient concentration are highly desirable for an efficient performance of a Li-ion cell.

The most commonly used electrolytes are a mixture of one or more alkyl carbonates, such as ethylene, dimethyl, diethyl, and ethyl methyl carbonates (EC, DMC, DEC, EMC, respectively), and $LiPF_6$ salt.[24–27] The alkyl carbonate solvents are chosen due to their higher oxidative/reductive stability at the operating potential of the transition metal oxide cathode, as well as graphitic anode. They also possess other properties, such as high polarity, a reasonable operating temperature range, low toxicity, and adequate safety features.[27] Especially, EC has an excellent dielectric property, its

dielectric constant (ε =89) is even higher than water (~ε=79). However, a relatively higher melting point of EC (~36 ºC) makes it unfavorable as a room temperature electrolyte solvent. Linear carbonates (such as DMC) differ from their cyclic cousins by their low melting points, low viscosity, and low dielectric constant. However, their ability to form homogeneous mixtures with EC at any ratio makes them an excellent co-solvent to be used with the EC to obtain the desirable properties of low-melting-temperature, low viscosity, and higher ionic conductivity.

Ionic liquid based electrolytes have received attention in recent years due to their negligible vapor pressure, excellent thermal and electrochemical stability, dissolution with many organic and inorganic compounds, and low flammability.[28] For high voltage spinel cathodes, tetramethylene sulfone (TMS or sulfolane)-based electrolytes were reported to have a high oxidative stability and a good cycling ability.[29]

1.4.4 Working Principles of a Li-ion Battery

The operating mechanism of a Li-ion battery can be explained as follows: during battery charging, transition metal oxide based cathode material oxidizes, for example, in $LiCoO_2$, the oxidation number of Cobalt increases from +3 to +4, and releases Li^+. The Li^+ transports through the electrolyte towards the graphitic anode. In the anode, in the presence of superfluous electrons, Li^+ get reduced and intercalates into the graphite layer as a Li-metal. The discharging process operates in an opposite way. When battery electrodes are connected through an external circuit, Li atom in the anode oxidizes to give up its electron and convert to Li^+. The electron flows through the outer circuits and arrives at the cathode. The Li^+ again diffuses back to the cathode, where it get reduced, and transition metal restores its oxidation state, as such the oxidation number of Cobalt in $LiCoO_2$ decreases from +4 to +3.

1.4.5 Solid Electrolyte Interphase

It is well-known that during the first charge cycle of LIBs, anodic reduction of the electrolytes creates a thin passivation layer consists of different organic and inorganic compounds which prevents decomposition of the electrolytes in the subsequent cycles. It also leads to the irreversible loss of Li, therefore, detrimentally affect the capacity of the battery.[30] In an ideal case, this layer has an electron transference number, t_e=0, and high ionic conductivity so that during battery operation, lithium ions can easily migrate through the layer to intercalate into and deintercalate from the graphitic anode. This essential passivation layer was named as a Solid Electrolyte Interphase (SEI) layer by Peled.[31] The properties of the SEI layer significantly affect the LIBs cycling ability, lifetime, capacity retention, high power density, rate capability, and safety.[32–34] The SEI should have an excellent mechanical strength and flexibility so that it allows the expansion and contraction of the graphite lattice during the reversible intercalation/deintercalation process. The lower solubility of the SEI to the electrolytes is desirable to limit continuous consumption of the lithium. The SEI formation is significantly contingent upon the organic solvents used in a battery. For example, SEI is formed in an EC solvent, however, no such layer has been observed when propylene carbonate (PC) is used unless suitable additives like vinylene carbonates (VC) are added in it. At an overcharged condition, SEI formation is also possible at the cathode-electrolyte interface due to the cathodic oxidation of the electrolytes.[35]

Given the high technological importance, extensive research efforts have been devoted to study the SEI formation mechanism as well as its chemical compositions using a wide variety of advanced computational and experimental techniques, but detailed chemistry remains elusive.[7,36] Major difficulty in studying the SEI is the lack of computational facilities to meet the required length and time scale for molecular modeling and devoid of proper *in-situ* characterization techniques[37] while the battery is in operation.

During battery cycling, electrolyte reduction and oxidation occur at the anode and cathode surfaces, respectively. In the current Li-ion battery technology, cathode materials operate at an average potential of 4V versus Li/Li^+, while commonly used electrolytes reduction and oxidation potentials are below 2V and around 6V, respectively.[17] Thus, anodic reduction of the electrolytes causes SEI formation at the anode-electrolyte interfaces. However, application of high voltage cathodes invoke oxidative decomposition of electrolytes; therefore, SEI may form at the cathode-electrolyte interface as well. Numerous mechanisms have been proposed in literature for explaining the intricate chemistry of the SEI formation. Besenhard et al.[38,39] proposed that an electrolyte solvent can co-intercalate into the graphitic anode to form a graphitic intercalation compound, and the decomposition products determine further reaction behavior. Aurbach et al.[40] claimed that the initial surface film controls the nature of subsequent reactions. However, a detailed mechanistic picture is still under debate. Understanding of the electrolyte decomposition reactions is the key aspect of studying the SEI formation mechanism.

1.5 Lithium-Sulfur Batteries

Li-S cell is typically comprised of lithium negative electrode, elemental sulfur-carbon composite positive electrode, organic electrolytes, and a porous separator between electrodes.[41] Figure 1-7 shows a schematic representation of a lithium-sulfur cell. The Li-S cell operates quite differently than the intercalation based Li-ion batteries. The fundamental chemistry is based on the redox reaction of $16Li + S_8 \rightarrow 8Li_2S$, with an average cell voltage of 2.2V with respect to Li/Li^+.[42] During discharge, lithium cleavages sulfur-sulfur bond and opens S_8 ring to produce a series of lithium polysulfides of general formula Li_mS_n ($1 \leq n \leq 8$, $m=1,2$). The higher ($3 \leq n \leq 8$) order polysulfides can spontaneously diffuse through the electrolytes thus increases the viscosity of the electrolytes.[41]

During charging, larger molecular weight polysulfides generated at the sulfur cathode migrate through the separator to the lithium anode and reduce to the lower order polysulfides. These compounds diffuse back to the cathode and re-oxidize to generate higher order polysulfides instead of converting to the elemental sulfur, thus create a 'shuttle mechanism'. This shuttling process causes an internal current which leads to self-discharge and a severe drop in coulombic efficiency.[43] The two end products of the elemental sulfur reduction are Li_2S_2 and Li_2S. They are insoluble in the electrolytes and precipitates from the solution to passivate both positive and negative electrode surface and deters electrochemical reversibility,[42,44,45] buildup impedance layer,[46] and causes active mass loss.[42]

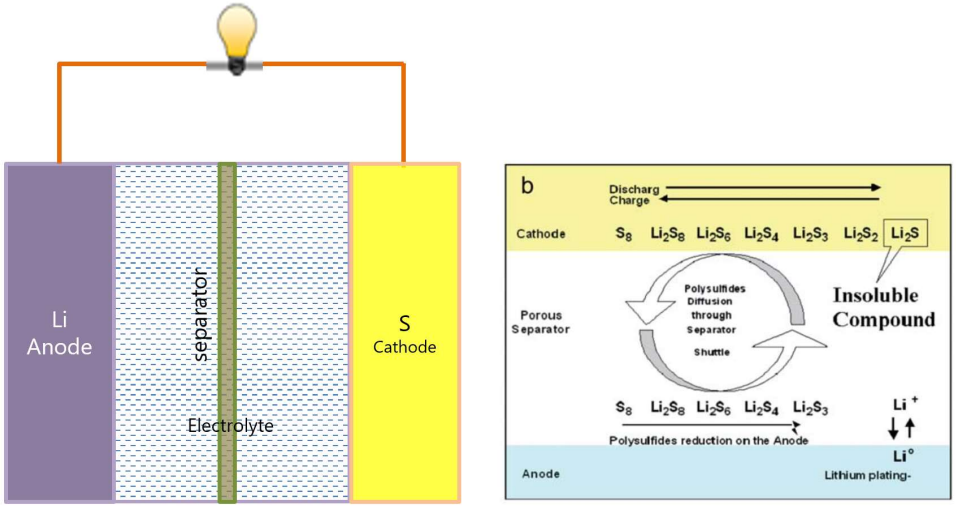

Figure 1-7 (a) Schematic of Lithium-sulfur cell (b) Lithium-sulfur cell operation scheme[41]

Ether-based electrolytes, such as, tetra(ethylene glycol) dimethyl ether (TEGDME),[47,14–20] poly(ethylene glycol) dimethyl ether(PEGDME),[43] tetrahydrofuran (THF),[48] and 1,3-dioxolane (DOXL)[49–51] and lithium bis-tri-fluoromethane sulfonamide (LiTFSI),[52] lithium trifluoromethane sulfonate ($LiCF_3SO_3$)[47,49] salts are commonly used in Li-S batteries. Often times, a single solvent is unable to meet the requirements of an electrolyte. Therefore, a mixture of multiple solvents is used, for example. TEGDME/THF,[48] TEGDME/DOXL.[49]

The commercialization of the Li-S batteries has been thwarted owing to a number of performance limiting issues, such as high lithium reactivity and dendrite formation at the anode surface. Ingress and egress of lithium ion into and from the sulfur cathode causes periodic volume expansion and compression of the cathode material and responsible for the stress-induced failure. A detailed description and the limitations of the current lithium sulfur battery technologies are provided in the Chapter 5 and 6.

1.6 Overview of this Work

The objective of this research is to explore interfacial chemistry and electrode properties of Li-batteries using reactive molecular dynamics (MD) simulations. Despite a significant amount of experimental effort, detailed mechanisms of the intricate interfacial chemistry have not been explored comprehensively. The atomistic simulations can effectively enlighten the issues pertinent to the battery chemistry and the change in electrode properties during battery cycling. Several DFT based *ab-initio* MD simulations for investigating electrolyte decompositions at the electrode-electrolyte interfaces have been reported in recent literature.[53–59] However, applications of the quantum chemistry (QC) based methods are extremely limited by the length and time-scale that are required to predict the complex processes occurring at the Li-battery interfaces. Therefore, large-scale MD simulations are necessary to address the issues associated with the interfaces of Li-batteries. Reactive force field (RFF) based methods are computationally cheap and can simulate reactions, therefore providing an attractive alternative to QC methods. In general, RFF-based methods are several orders of magnitude faster than QC methods and can handle systems with bigger length and time scales which is essential for investigating battery systems. ReaxFF is a reactive force field method, capable of describing reactions in nanoseconds of simulation in a length scale of nanometers while retaining most of the accuracy of DFT methods.[60] However, the absence of an explicit electronic degree of freedom limits the application of the ReaxFF method in

describing interfacial redox reactions of Li-ion batteries. Therefore, a comprehensive investigation of the interfacial oxidation and reduction reactions associated with the electrolyte decomposition and the formation of SEI requires an extension of the capability of the ReaxFF method to incorporate an explicit electron or hole description.

In this work, we developed an explicit electron version of the ReaxFF method, which we refer as 'eReaxFF' method. We parameterized eReaxFF force fields for studying electron dynamics in model hydrocarbon radicals and the reduction chemistry of ethylene carbonate for elucidating the SEI formation mechanism.

In addition to the eReaxFF method, standard ReaxFF potential has also been employed to study the effect of an *ex-situ* treatment on the electrolyte dissociation chemistry and mechanical responses of sulfur cathode materials of Li-S cell. The battery systems considered herein involve Li/S/C/H/O/F interactions. For this purpose, a ReaxFF force field has been developed using DFT data to describe Li-F interactions and merged with the previous C/H/O/S force field to study anode-electrolyte interfaces in Li-S battery. Furthermore, Li-S ReaxFF parameters were also developed for investigating the properties of sulfur cathode materials upon lithiation.

This dissertation is organized as follows: after a brief introduction to the current state of lithium batteries in Chapter 1, Chapter 2 provides a detailed description of the energy functional of the ReaxFF method. The fundamental concepts of the explicit electron description in the eReaxFF method and a proof of principle application of the eReaxFF method are presented in Chapter 3. In Chapter 4, a detailed understanding of the interfacial chemistry of the Li-ion batteries is described, and the application of the eReaxFF method in simulating the SEI formation reactions is delineated. The Li-F force field development followed by molecular dynamics simulations on the effect of Teflon coating on the electrolyte dissociations in a Li-S battery are presented in Chapter 5. In Chapter 6, development of a Li-S force field and its application in investigating the structural,

mechanical, and kinetic behavior of the amorphous lithiated sulfur (a-Li_xS) compounds are described. Finally, Chapter 7 summarizes the conclusions and the outlook for future work.

Chapter 2

ReaxFF Reactive Force Field

2.1 Overview

ReaxFF is a general bond order[61,62] (BO) based empirical force field method which allows bond breaking and formation during simulations. In ReaxFF, forces on each atom are derived from the following energy expression

$$E_{system} = E_{bond} + E_{over} + E_{under} + E_{lp} + E_{val} + E_{tor} + E_{vdWaals} + E_{Coulomb} \quad (2.1)$$

where partial energy contributions include bond, over-coordination penalty and under-coordination stability, lone pair, valence, and torsion, non-bonded interactions van der Waals, and Coulomb energies, respectively.

ReaxFF uses the concept of bond orders to determine the bonded interactions among all atoms in a system. BOs are calculated from the interatomic distance and updated in every iteration. Since all the connectivity dependent interactions, i.e. valence and torsion energy are BO dependent, their energy contribution diminishes upon bond breaking. In non-reactive force fields, non-bonded interactions i.e. van der Waals and Coulomb are usually calculated between atom pairs that are not involved in a bond or not sharing a valence angle. However, in a reactive environment, atomic connectivity changes during a simulation and it is awkward to setup such an exclusion rule, therefore, in ReaxFF non-bonded interactions are calculated between all the atom pairs irrespective of their connectivity. To avoid Coulomb catastrophe, any excessive short distance non-bonded interactions are screened by using a shielding term in the van der Waals and Coulomb energy expressions. To eliminate any discontinuity in the non-bonded interaction energies, a seventh order taper function is employed.[63] The geometry dependent charge calculation schemes, Electronegativity Equalization Method (EEM)[64] and Atom-condensed Kohn-Sham DFT approximated to second order (ACKS2)[65] are used for charge calculation.

2.2 Description of the ReaxFF Energy Functional

Bond Order and Bond Energy (E_{bond})

ReaxFF assumes that bond order is a function of inter atomic distance between two atoms and is obtained using equation (2.2). In calculating the bond orders, ReaxFF distinguishes between contributions from sigma bonds, pi-bonds and double-pi-bonds.

$$BO'_{ij} = exp\left[p_{bo,1}\left(\frac{r_{ij}}{r_0}\right)^{p_{bo,2}} \right] + exp\left[p_{bo,3}\left(\frac{r^{\pi}_{ij}}{r_0}\right)^{p_{bo,4}} \right] + exp\left[p_{bo,5}\left(\frac{r^{\pi\pi}_{ij}}{r_0}\right)^{p_{bo,6}} \right] \quad (2.2)$$

where and are the partial contributions of σ, π- and double π-bonds between atoms i and j , r_{ij} is the distance between i and j , r_o^{σ} , r_o^{π} , and $r_o^{\pi\pi}$ are the bond radii of σ, π- and double π-bonds, respectively, and p_{bo} terms are empirical parameters fit to experimental or quantum data. The corrected bond orders are used for calculating bond energy which is given by equation (2.3).

$$E_{bond} = -D_e^{\sigma}.BO_{ij}^{\sigma}.exp\left[p_{be1}\left(1-\left(BO_{ij}^{\sigma}\right)^{p_{be2}}\right) - D_e^{\pi}BO_{ij}^{\pi} - D_e^{\pi\pi}BO_{ij}^{\pi\pi} \right] \quad (2.3)$$

where, p_{be1} , p_{be2} ,D_e^{π}, $D_e^{\pi\pi}$are force field parameters

Lone Pair Energy (E_{lp})

Lone pair, Δ_i^e is the difference between the total number of electrons in the outer shell and the sum of bond orders around the atomic center. The number of lone-pairs around an atom is calculated using equation (2.4b). The lone pair energy penalty is given by:

$$\Delta_i^{\ e} = -Val_i^{\ e} + \sum_{j=1}^{neighbor(i)} BO_{ij} \quad (2.4a)$$

$$n_{lp,i} = int\left(\frac{\Delta_i^{\ e}}{2}\right) + exp\left[-p_{lp1}.\left(2 + \Delta_i^{\ e} - 2.int\left\{\frac{\Delta_i^{\ e}}{2}\right\}\right)^2 \right] \quad (2.4b)$$

$$\Delta_i^{lp} = n_{lp,opt} - n_{lp,i} \tag{2.4c}$$

$$E_{lp} = \frac{p_{lp2}\Delta_i^{lp}}{1+\exp\left(-75\times\Delta_i^{lp}\right)} \tag{2.4d}$$

Where Δ_i^{lp} is the deviation from the optimal lone pair to the calculated lone pair and p_{lp1}, p_{lp2} are the force field parameter.

Overcoordination

An overcoordination, Δ_i, is calculated using following equation. For an overcoordinated atom (Δ_i>0), equation (2.5b-c) attributes an energy penalty on the system.

$$\Delta_i = -Val_i + \sum_{j=1}^{neighbor(i)} BO_{ij} \tag{2.5a}$$

$$E_{over} = \frac{\sum_{j=1}^{nbond} p_{ovun1}.D_e^{\sigma}.BO_{ij}}{\Delta_i^{lpcorr} + Val_i}.\Delta_i^{lpcorr}.\left[\frac{1}{1+exp\left(p_{ovun2}.\Delta_i^{lpcorr}\right)}\right] \tag{2.5b}$$

$$\Delta_i^{lpcorr} = \Delta_i - \frac{\Delta_i^{lp}}{1+p_{ovun3}.exp\left(p_{ovun4}.\left\{\sum_{j=1}^{neighbors(i)}\left(\Delta_j - \Delta_j^{lp}\right).(BO_{ij}^{\pi} + BO_{ij}^{\pi\pi})\right\}\right)} \tag{2.5c}$$

Where, Δ_i^{lpcorr} is the corrected overcoordination considering the deviation from the optimal number of lone pairs.

Undercoordination

For an undercoordinated atom (Δ_i<0), the energy contribution for the resonance of the π-electron between bonded under-coordinated atomic centers are taken care using equation (2.6).

E_{under} is only important when the bonds between under-coordinated atom *i* and its under-coordinated neighbors *j* have partly π-bond character.

$$E_{under} = -p_{ovun5}.\frac{1-\exp\left(p_{ovun6}.\Delta_i^{lpcorr}\right)}{1+\exp\left(-p_{ovun2}.\Delta_i^{lpcorr}\right)}.\frac{\Delta_i^{lp}}{1+p_{ovun7}.exp\left(p_{ovun8}.\left\{\sum_{j=1}^{neighbors(i)}\left(\Delta_j-\Delta_j^{lp}\right).(BO_{ij}^{\pi}+BO_{ij}^{\pi\pi}\right\}\right)} \tag{2.6}$$

The additional terms related to the the over and undercoordination energy functional which are developed for the eReaxFF method are described in the Chapter 3.

Valence Angle Energy (E_{val})

The bond order dependent form is utilized for calculating valence angle energy. The equilibrium angle Θ_0 for Θ_{ikj} used in equation (2.7) depends on the sum of π-bond orders around the central atom j. Valence angle energy is expressed by

$$E_{val} = f_7\left(BO_{ij}\right)\times f_7\left(BO_{kj}\right)\times f_8\left(\Delta_j\right)\times\left\{p_{val1}-p_{val1}exp\left[-p_{val2}\left(\Theta_0\left(BO\right)-\Theta_{ijk}\right)^2\right]\right\} \tag{2.7}$$

The exact functional forms of f_7 and f_8 can be found in ref [100] where p_{val1} and p_{val2} are force field parameters.

Torsion Angle Energy (E_{tor})

Torsion angle energy term is dependent on bond order like bond and angle energy term. It disappears when BO approaches to 0. The torsion angle energy term is expressed as follows.

$$E_{tor} = f_{10}\left(BO_{ij},BO_{jk},BO_{kl}\right)\times sin\Theta_{ijk}\times sin\Theta_{jkl}\times$$
$$\left[\frac{1}{2}V_1.\left(1+cos\omega_{ikjl}\right)+\frac{1}{2}V_2\times\exp\left\{p_{tor1}\left(BO_{jk}^{\pi}-1+f_{11}\left(\Delta_j,\Delta_k\right)\right)^2\right\}\left(1-cos2\omega_{ijkl}\right)+\frac{1}{2}V_3\left(1+cos3\omega_{ijkl}\right)\right] \tag{2.8}$$

Van der Waals Interaction Energy (E_{vdW})

To account for van der Waals interactions, distance-corrected Morse potential is chosen. By considering the shielded interaction, excessively high repulsions between bonded atoms and atoms sharing a valence angle are avoided.

$$E_{vdWaals} = Tap \times D_{ij} \times \left\{ exp\left[\alpha_{ij} \left(1 - \frac{f_{13}\left(r_{ij}\right)}{r_{vdW}} \right) \right] - 2 \times exp\left[\frac{1}{2} \alpha_{ij} \left(1 - \frac{f_{13}\left(r_{ij}\right)}{r_{vdW}} \right) \right] \right\} \tag{2.9a}$$

where Tap is a taper term which circumvents energy discontinuities when charged species move in and out of the non-bonded cutoff radius.

$$f_{13}\left(r_{ij}\right) = \left[r_{ij}^{p_{vdW}} + \left(\frac{1}{\gamma_w} \right)^{p_{vdW}} \right]^{\frac{1}{p_{vdW1}}} \tag{2.9b}$$

Coulomb Interaction Energy ($E_{Coulomb}$)

Coulomb interactions are calculated for each pair of atoms. A shielded Coulomb-potential is used to adjust orbital overlap between atoms at close distance. The EEM method uses following set of equations for the calculation of atomic charges:

$$\frac{\partial E}{\partial q_1} = \chi_1 + 2 q_1 \eta_1 + C. \sum_{j=1}^{n} \frac{q_j}{\left(r_{1,j} + (\frac{1}{\gamma_{1,j}})^3 \right)^{\frac{1}{3}}}$$

$$\frac{\partial E}{\partial q_2} = \chi_2 + 2 q_2 \eta_2 + C. \sum_{j=1}^{n} \frac{q_j}{\left(r_{2,j} + (\frac{1}{\gamma_{2,j}})^3 \right)^{\frac{1}{3}}}$$

……

$$\frac{\partial E}{\partial q_n} = \chi_n + 2q_n\eta_n + C.\sum_{j=1}^{n}\frac{q_j}{\left(r_{n,j} + (\frac{1}{\gamma_{n,j}})^3\right)^{\frac{1}{3}}}$$

$$\sum_{i=1}^{n} q_i = 0 \tag{2.10}$$

where χ, η, γ, r, and q are atom electronegativity, hardness, shielding, the interatomic distance, and atomic charge, respectively. The columbic interactions are calculated as

$$E_{coulomb} = Tap.C.\frac{q_i q_j}{\left[r_{ij}^3 + \left(\frac{1}{\gamma_{ij}}\right)^3\right]^{1/3}} \tag{2.11}$$

where, Tap is the seventh order taper function.

Electron-nuclear Interaction Energy

For describing explicit electron and core charge interaction, following functional form is introduced in the ReaxFF description:

$$E_{nuc(i)-elec(j)} = -\frac{1}{4\pi\varepsilon_o}\beta\sum_{i,j}\frac{Z_i}{R_{ij}}erf\left(\sqrt{2\alpha}R_{ij}\right) \tag{2.12}$$

Where Z_i is the nuclear charge, R_{ij} is the distance between electron and nucleus, and α (gaussian exponent), β are constant. The details of the eReaxFF method is discussed in the Chapter 3.

Chapter 3

eReaxFF: A Pseudoclassical Treatment of Explicit Electrons within Reactive Force Field Simulations

Part of this chapter also published in ref,[66] authored by Md Mahbubul Islam, Grigory Kolesov, Toon Verstraelen, Efthimios Kaxiras, and Adri CT van Duin. Md Mahbubul Islam performed all the eReaxFF simulations, analyzed results and wrote the paper.

3.1 Introduction

Electrons, which are intrinsically of a quantum nature, govern all forms of molecular structures and chemical reactions. In order to investigate the mechanism of chemical reactions and physical properties of substances at an atomistic level, computational chemistry has been used extensively as a complement to experimental techniques over at least the last four decades. Historically, the development of computational methodologies for describing chemical reactions at an atomistic scale has primarily concentrated on quantum chemistry (QC) methods. These methods, which possess explicit electronic degrees of freedom, provide the most accurate and detailed description of chemical reactions, but their inherent complexity in formalism and high computational cost limit applications to relatively small length- and time-scales. Empirical formalisms have been introduced in QC methods to improve computational efficiency, at the expense of accuracy. Approximate QC based methods—for example, density functional theory (DFT) or Tight-Binding (TB) schemes—have been developed as computationally advantageous alternatives to truly *ab initio* methods. Even with such approximations, non-adiabatic dynamics using time-dependent DFT are quite expensive and are limited to a relatively small number of atoms (~1000) and short time scales (~1 ps).[67,68]

Force field (FF) based methods have also been developed as an alternative to QC methods. FF methods use simplified functional forms and provide much better computational performance, enabling simulations to access much larger scales, of order nanometers in length and nanoseconds in time. However, most of the available force field methods provide a substitute for the electronic structure and are typically nonreactive in nature, implying the absence of explicit electrons and their impact on system geometry and energy, as well as the inability to simulate bond breaking and formation. To bridge the gap between minimal computational cost and the ability to simulate reactions, a genre of force field methods known as 'reactive force fields' was developed. The reactive force field methods[60,62,69,70] possess the capability of simulating reactions on-the-fly, however, the implicit treatment of electrons is inadequate for the description of many physical systems, such as redox reactions of rechargeable battery interfaces, polarization behavior in ferro-/piezo-electric materials, and solar cells. An accurate description of these phenomena requires an explicit treatment of electron degrees of freedom, which must be within the classical framework of the classical potentials.

Recently, a number of force field methods have been developed that include aspects of explicit valence electrons, like the electron force field (eFF)[71,72] and LEWIS[73–75] force field. The eFF has been parameterized only for a limited number of elements in the periodic table, and the primary application areas are materials that are subjected to extreme pressure and temperature apart from the complexity of the reactive systems.[71,72] The ability of the LEWIS method to describe atomic electron affinities (EA) and ionization potentials (IP) of the first three row elements is encouraging, still such description for molecules is not available.[76,77] The low-temperature dynamics of liquid water[73,75] and prediction of ground state configurations of some chemical species[78] indicate the promising capabilities of the LEWIS method, but, the challenge of describing complex reactions, or high-temperature dynamics with an acceptable level of accuracy is yet to be demonstrated. There also exists alternate methods to couple covalent and electrostatic interactions

through split-charge equilibration (SQE)[79,80] for describing charge transfer in reactive dynamics,[81] without an explicit electron treatment. To the best of our knowledge, no classical force field method with access to explicit electrons has been employed to simulate complex reactive events.

The standard ReaxFF (denoted as '*ReaxFF*') reactive force field method[60,82] covers a broad range of elements in the periodic table with a good track record of wide application areas.[82–86] It has proven a reliable tool for performing longer-scale reactive molecular dynamics (MD) simulations that involve complex chemistry at surfaces and interfaces.[86–88] ReaxFF has relatively sophisticated schemes to treat electrons in its energy functional—not explicitly rather implicitly it accounts for the effect of electron distribution in chemical bonding. Such as an over- or under-coordination energy term performs by evaluating the difference between the number of electrons around an atom involved in a bonded interaction and the number of valence electrons of the atom. A polarizable charge calculation scheme obtains charges on every atom based on atomic electronegativity and hardness, and a lone-pair term includes the energy effects of breaking up a lone electron pair on an atom.[82] ReaxFF is computationally significantly less intensive than DFT or TB methods and is capable of nanoseconds of MD simulations with millions of atoms.[89] The lack of an explicit electron description limits the applications of the ReaxFF in redox chemistry or in describing polarization behavior in bulk materials, despite its success in a wide range of systems.[15,87,90–93] The inability of ReaxFF to give accurate EAs or IPs for various molecules restricts its applicability to the description of redox reactions.[94] A detailed investigation of electron flow associated reactions or electron dynamics requires further extensions to the ReaxFF concept.

To extend the ReaxFF method, we introduce an explicit electron-like or hole-like particle description into this method. The treatment of an explicit electron within the classical framework can only capture the "particle" nature of the "wave-particle dual" nature of the electron. The wave properties are treated implicitly in the functionals of the ReaxFF method. This electron version of the ReaxFF method will be addressed as 'eReaxFF'. In this study, we perform the force field

training, and as a proof of concept we consider two model hydrocarbon radicals and study electron transfer (ET) dynamics to compare our eReaxFF results with those obtained from Ehrenfest dynamics simulations.

This chapter is organized as follows. In section 3.2, we introduce the general theory of the eReaxFF method and implementation of the Atom-condensed Kohn-Sham DFT approximated to second order (ACKS2)[65] charge calculation scheme. Section 3.3 describes the relevant force field training results. In section 3.4, we present an application of the eReaxFF method to the model hydrocarbon radicals that includes highlights from the eReaxFF MD simulations and a comparison with the Ehrenfest dynamics results.

3.2 Computational Methods

3.2.1 General Theory of eReaxFF

We developed our eReaxFF method within the basic framework of the ReaxFF. All 2-, 3-, and 4-body and nonbonded interaction terms of ReaxFF are retained. Next, we added new energy functionals to compute pairwise electrostatic interactions for explicit electrons and modified existing over- and under-coordination energy terms.

We incorporated a limited pseudo-classical explicit electron/hole degrees-of-freedom scheme that is complementary to the implicit treatment of electrons in the bonded interactions of ReaxFF. The electron or hole is represented as an additional particle that carries a -1 (electron) or +1 (hole) charge, respectively. The nuclei are treated as point charges and electrons as Gaussian wave functions ($\psi \infty \exp(-\alpha(r-r')^2)$). The energy is a function of the position of the electron and atomic-centers, and depends on the spread of the Gaussian function, α. The pairwise electrostatic interaction between the electron and core-charge is described as[71]

$$E_{nucl(i)-elec(j)} = -\frac{1}{4\pi\varepsilon_o}\beta\sum_{i,j}\frac{Z_i}{R_{ij}}\mathrm{erf}\left(\sqrt{2\alpha}R_{ij}\right) \quad (2)$$

where Z_i is the nuclear charge, R_{ij} is the distance between the electron and nucleus, α (Gaussian exponent), and β are constants that depends on the atom type. The core-charge is the charge corresponding to the atomic number of an atom. Electron-electron interactions are treated through Coulomb point charges, and short-range Gaussian repulsion functions.

In ReaxFF, valency and number of lone-pair electrons are treated as constants for an atom type. It is necessary to allow changes in the atom valency and number of lone pair of electrons when explicit electron/hole degrees of freedom are introduced into the system. The diffuse nature of an added explicit electron/hole and its relation to a particular atom is described as a function of the distance between electron/hole and the nuclear position of the host atom. We chose an exponential function to determine the number of electrons in the host atom, at the same time, this function ensures that an electron can virtually split itself among its neighboring atoms, that is, it resembles a partial delocalization in a molecule. This function has the following form:

$$n_{el} = exp\left(-p_{val}.R_{ij}^{\ 2}\right) \tag{3}$$

where R_{ij} is the distance between the atom-center and the electron/hole and p_{val} is a general parameter in the force field.

The effect of an explicit electron in the vicinity of an atom can be explained as follows: an electron uptake by an oxygen atom, for instance, decreases its valency and increases its number of valence electrons by one. This changed oxygen atom behaves like a pseudo-fluorine atom, that is, it acquires an electron configuration similar to that of fluorine. The acceptance of a hole acts in the opposite manner, the number of outer shell electrons is reduced, and the valency of the oxygen atom increases from two to three, thus the electron deficient oxygen atom resembles the electron configuration of nitrogen. Accordingly, we have established a set of rules in the eReaxFF code that dictates the effect of explicit electron/hole on the respective atom types. The atom valency and the

number of lone-pair electrons become a dynamic variable, and they are evaluated at every step of the dynamics.

In ReaxFF, the bonded and non-bonded interactions are calculated independently, that is, charge is not coupled with the number of valence electrons of an atom type which is used in bond order correction and over- and under-coordination energy terms. For example, a Li^+-dimer is, in principle, able to make a Li-Li bond—despite the positive charge—as the number of valence electron remains one. With the charge-valency coupling, the Li^+-Li^+ bond is additionally counteracted by the over-coordination terms, as the positively charged Li-atom loses its valence electron. In our eReaxFF implementation, the explicit charges of an atom are coupled with the atom valency and the over- and under-coordination energies are calculated based on the corrected valence electrons.

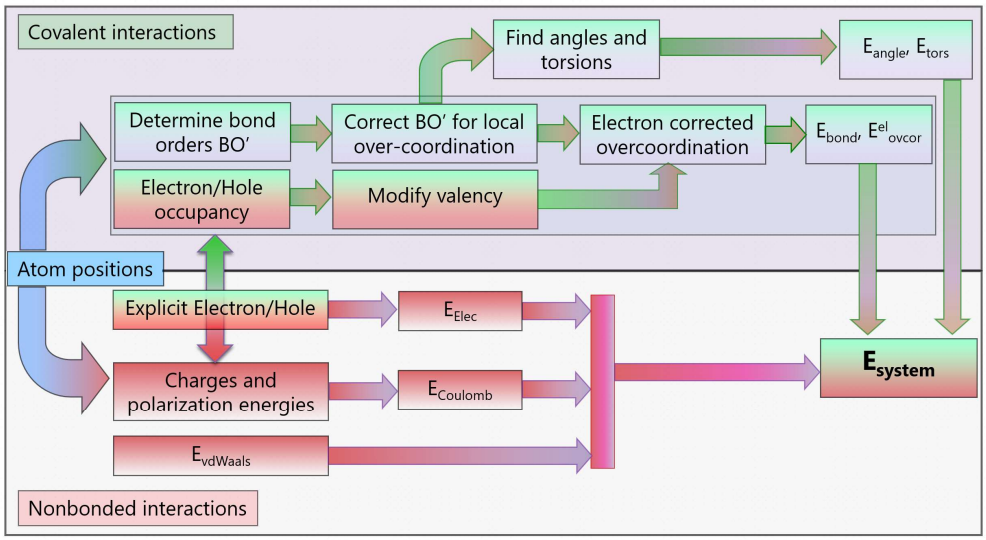

Figure 3-1 Flow diagram of the eReaxFF method: the covalent and nonbonded interactions are coupled through the explicit electron/hole.

Modification in the number of valence electrons of an atom type modifies the degree of over- or under-coordination (Δ_i), thus corresponding energy penalties. We explain how the degree

of over- or under-coordination is calculated below. A decrease in the valency of an atom at an existing bonding environment increases the over-coordination, resulting in a larger over-coordination energy penalty, and therefore reduces the BO associated with the atom and weakens relevant bonds. For example, in a methane molecule, an electron uptake by the carbon will decrease its valency from four to three, and at this bonding situation the carbon atom is further over-coordinated by ~1 which leads to a significant over-coordination energy penalty, and total bond order of carbon reduction to ~3.0 resulting in the elongation of C-H bonds.

In our eReaxFF implementation, the amount of modified degree of over- or under-coordination used in the corresponding energy penalty calculation is designed as a function of both atom and bond types, that is, it is contingent on the atom type as well as on the local bonding environment. This atom and bond-type dependent treatment of over- and under-coordination enable the eReaxFF method to capture EAs or IPs of various species using the same set of atomic-Gaussian parameters. The modified over- and under-coordination energy functionals are given by:

$$\textit{Degree of over-coordination},\ \Delta_i = -Val_i + \sum_{j=1}^{neighbor(i)} BO_{ij} \tag{4(a)}$$

$$\textit{Bond type dependency},\quad f_{bond} = n_{el} \cdot \frac{\sum_{j=1}^{nbond} BO_{ij} \cdot p_{ij}^{xel1}}{\sum_{j=1}^{neighbor(i)} BO_{ij}} \tag{4(b)}$$

$$\textit{Atom type dependency},\quad f_i = exp(-p_i^{xel2} \cdot f_{bond}) \tag{4(c)}$$

$$\textit{Explicit electron correction},\ \Delta_i^{xel} = \Delta_i . \exp(-p_i^{xel2} . n_{el} \cdot \frac{\sum_{j=1}^{nbond} BO_{ij} \cdot p_{ij}^{xel1}}{\sum_{j=1}^{neighbor(i)} BO_{ij}}) \tag{4(d)}$$

$$\Delta_i^{lpcorr} = \Delta_i^{xel} - \frac{\Delta_i^{lp}}{1 + p_{ovun3}.exp\left(p_{ovun}.\left\{ \sum_{j=1}^{neighbors(i)} \left(\Delta_j^{xel} - \Delta_j^{lp} \right).\left(BO_{ij}^{\pi} + BO_{ij}^{\pi\pi} \right) \right\} \right)} \quad 4(e)$$

$$E_{over} = \frac{\sum_{j=1}^{nbond} p_{ovun1}.D_e^{\sigma}.BO_{ij}}{\Delta_i^{lpcorr} + Val_i}.\Delta_i^{lpcorr}.\left[\frac{1}{1 + \exp\left(p_{ovun2}.\Delta_i^{lpcorr} \right)} \right] \quad 4(f)$$

$$E_{under} = -p_{ovun5}.\frac{1 - exp\left(p_{ovun6}.\Delta_i^{lpcorr} \right)}{1 + exp\left(-p_{ovun2}.\Delta_i^{lpcorr} \right)}.\frac{\Delta_i^{lpcorr}}{1 + p_{ovun7}.exp\left(p_{ovun8}.\left\{ \sum_{j=1}^{neighbors(i)} \left(\Delta_j^{xel} - \Delta_j^{lp} \right).(BO_{ij}^{\pi} + BO_{ij}^{\pi\pi} \right) \right\} \right)} \quad 4(g)$$

We used new functional forms for an explicit electron correction on the degree of over-/under-coordination. It is essential to choose a functional form that is efficient in computation and smoothly differentiable to ensure energy conservation. The former condition is satisfied by using simple exponentials, and the latter is ensured since the functional form is analytically differentiable. The explicit electron correction depends on the BOs and the electron occupancy of the host atom. The bond type parameter (p_{ij}^{xel1}) and the corresponding BOs are used to adjust the number of electrons available to the host atom (Eq. 4(b)). The atom type dependency is introduced through Eq. 4(c), where p_i^{xel2} is an atom type parameter. Finally, the explicit electron correction on the Δ_i is expressed in Eq. 4(d) as Δ_i^{xel}. The Δ_i^{xel} is used in Eq. 4(e), 4(f), and 4(g) to calculate the explicit electron modified over- or under-coordination energy penalty. In our current eReaxFF implementation, a variable valency is considered in the over- and under-coordination and lone-pair energy functionals. In future developments, variable valency will be extended to the three and four body terms, that is, the valence angle and torsion energy expressions. The flow scheme of the eReaxFF method is shown in Figure 3-1. The fictitious mass of the electron and hole are assigned as equivalent to that of a hydrogen atom (1 a.m.u). Two other computational methods—eFF[7] and

LEWIS[9]—where electrons are treated semi-classically, also uses 1 a.m.u as a mass of the electron. The eReaxFF code is currently available only in a serial version, and a parallel implementation in the commercial Amsterdam Density Function (ADF)[95] package is planned.

3.2.2 ACKS2 Charge Calculation Scheme

The EEM method—widely used within the ReaxFF approach—is known for its spurious long-range charge transfer, for instance, between two or more molecules, even when they are well-separated.[96] It allows charge to be redistributed over all atoms as if the total system is an electric conductor.[97,98] The long-range charge transfer of the EEM scheme is problematic for the eReaxFF method, as it impedes the accurate charge description of the reduced/oxidized molecules. The metallic polarizability of the EEM charges results in an almost complete charge compensation of the explicit electrons or holes. The ACKS2 charge calculation scheme[65] largely eliminates the issue of unrealistic long-range charge smearing. Therefore, we implemented this method in our eReaxFF code.

Just like the EEM energy, the ACKS2 energy is quadratic in the atomic charges. Additional variables and quadratic energy terms are introduced to control the range over which charge can delocalize:

$$E_{\mathrm{ACKS2}} = \min_{\substack{\{q_i\} \\ \sum q_i = \sum q_i^0}} \left[\sum_{i=1}^{natom} \chi_i q_i + \frac{1}{2} \sum_{\substack{i=1 \\ j=1}}^{natom} \eta_{ij} q_i q_j + \max_{\substack{\{u_i\} \\ \sum u_i = 0}} \left[\sum_{i=1}^{natom} u_i (q_i - q_i^0) + \frac{1}{2} \sum_{\substack{i=1 \\ j=1}}^{natom} X_{ij} u_i u_j \right] \right]$$

The variables are q_i (atomic charges) and u_i (fluctuations in the atomic Kohn-Sham potential) and are recomputed at each time step for the current geometry. The first two terms are identical to the EEM energy in the conventional ReaxFF, whereas the last two terms are new and account for non-local contributions to the electronic kinetic energy.[65] In ReaxFF, χ_i and η_{ii} are atomic parameters, which are fixed for every chemical element in the calibration process. The

parameter q_k^0 is a reference charge: it is zero for all atoms and it is set to -1 or $+1$ for the explicit electron or hole, respectively. The remaining matrix elements depend on the interatomic distance R_{ij} as follows:

$$\eta_{ij} = \frac{1}{4\pi\varepsilon_0} \frac{1}{\sqrt[3]{R_{ij}^3 + (\gamma_i\gamma_j)^{-3/2}}}$$

$$X_{ij} = X_{\text{soft}} \left(\frac{2R_{ij}}{C_i + C_j}\right)^3 \left(1 - \frac{2R_{ij}}{C_i + C_j}\right)^6 \quad \text{when} \quad R_{ij} < (C_i + C_j)/2$$

$$X_{ij} = 0 \quad \text{when} \quad R_{ij} \geq (C_i + C_j)/2$$

$$X_{ii} = -\sum_{\substack{j=1 \\ j \neq i}}^{natom} X_{ij}$$

The off-diagonal element η_{ij} represents the Coulomb interaction with short-range damping controlled by the atomic parameters γ_i and γ_j.[99] The off-diagonal element X_{ij} can be interpreted as a bond softness (or atom pair softness): it determines to what extent atom i and j can exchange charge directly. In the bonding region, X_{ij} increases with increasing R_{ij} until it reaches its maximum, X_{soft}, and then goes smoothly to zero at the cutoff $(C_i + C_j)/2$. The atomic softness cutoff parameters C_i and the universal softness parameter X_{soft} are fixed in the calibration procedure, with the cutoff parameters remaining short-ranged.

The energy penalty for a direct charge transfer between atoms i and j is quadratic in charge transfer and is proportional to $1/X_{ij}$.[65] When X_{ij} is zero, charge transfer must pass through intermediate atoms, with similar energy penalties for all intermediate atom pairs. When no intermediate pairs are present, for example, between two separated molecules, no charge transfer is allowed, and the total charge of each isolated fragment is equal to the sum of the reference charges of the constituting particles. When two distant atoms reside in the same macromolecule,

the number of required intermediate pairs, and thus also the energy penalty for charge transfer, scales linearly with the interatomic distance, which effectively inhibits long-range charge transfer.

The constrained minimization and maximization in the ACKS2 energy can be carried out simultaneously by solving a set of linear equations, which is similar to the EEM scheme. In addition, constraints are added to fix the charge of the explicit electron or hole, to -1 or $+1$, respectively. When some (or even all) X_{ij} elements go to zero, the equations remain well behaved, which is attractive compared to the BOP/SQE model, in which charge transfer is disabled by letting a bond-hardness parameter diverge to $+\infty$.[97] The polarization catastrophe can be avoided by imposing the following inequalities on the parameters: $\eta_{ii} > \frac{\gamma_i}{4\pi\varepsilon_0}$ and $X_{\text{soft}} > 0$. Under these conditions, the matrices η_{ij} and X_{ij} are guaranteed to be positive and negative semi-definite, respectively, for any possible geometry. As such, the minimum and maximum in the ACKS2 energy are well defined.

Originally, the ACKS2 model was derived from Kohn-Sham DFT and only included fluctuating atomic charges (and their conjugate potential variables). Recently, it was shown that a similar formalism can be derived from any variational electronic structure theory and that the ACKS2 model is easily extended with atomic multipole moments.[65]

Although EEM and ACKS2 are conceptually similar, EEM-based ReaxFF force fields still need to be refitted to work with the ACKS2 method. Fortunately, given the similarities between EEM and ACKS2 similarities, this refitting is relatively straightforward – as the EEM-based ReaxFF parameters are typically a very good initial guess for the ACKS2/ReaxFF parameters. Apart from this EEM/ACKS2 transition, the current eReaxFF implementation is fully transferable with the ReaxFF parameter sets available in literature.

3.3. Force Field Training

The accuracy of the description of reduction reactions depends primarily on the ability of the force field method to reproduce EAs of various chemical species. We trained our eReaxFF force field to reproduce the EAs of various saturated, unsaturated, and radical species. The objective of choosing all three types of species is to demonstrate that eReaxFF can describe EAs in a wide range of bonding environments. The optimization of the parameters was performed via a successive one-parameter search technique[100] to minimize the following expression for the error

$$Error = \sum_{i}^{n} \left[\frac{(x_{i,lit} - x_{i,eReaxFF})}{\sigma_i} \right]^2$$

where x_{lit} is the target value for the EA, x_{eReaxFF} is the eReaxFF calculated value, and σ_i is the weight assigned to data point, i.

We performed training to optimize only those parameters that are related to the explicit electron description, that is, the atomic-Gaussian, as well as atom and bond parameters as they appear in Eq. 4(d) and retained all other original ReaxFF parameters. In eReaxFF, the electron affinity is defined as:

$$EA(X) = E_X - E_X^- + E_{el}$$

where E_X and E_X^- are the energy of a species in a neutral state, and in a state with an additional electron, respectively, and E_{el} is the energy of an electron. In ReaxFF simulations, the EA is calculated by subtracting the energy of a negatively charged species from the neutral one with the constraint of setting the molecular charge equal to -1e. In eReaxFF simulations, the EA is calculated by adding an electron to a molecule. In our description, the electron is a negatively charged particle, therefore, it is mostly localized at a particular site in the molecule during geometry optimization. As described in the previous section, a limited degree of delocalization is still

available among the neighboring atoms through the modification of their valence. This delocalization influences the local chemistry of the molecule. Quantum calculations indicate a higher-degree of delocalization of the added electron over the entire molecule, compared to the eReaxFF method. This particular limitation is a result of the treatment of the electron as a pseudo-classical particle.

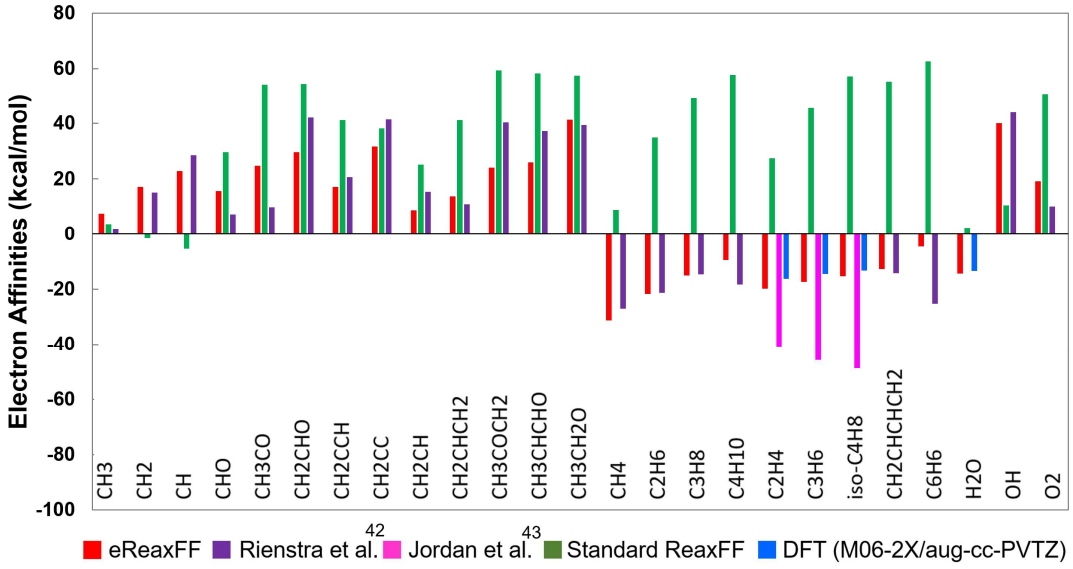

Figure 3-2 Electron affinity data of various species as calculated using the eReaxFF method and comparison with the experimental[101,102] and DFT data.

The eReaxFF force field training results of the EAs of various species are summarized in Figure 3-2 and compared to both ReaxFF and literature data.[101,102] eReaxFF qualitatively reproduces the literature data of the EAs, while the ReaxFF completely fails to capture EAs of most of the species considered in the training set. eReaxFF significantly underestimates the EAs of the three unsaturated species, ethylene, propene, and iso-butene, compared to experimental data.[102] To investigate this discrepancy, we performed DFT calculations with the M06-2X/aug-cc-PVTZ basis set functional implemented in the Jaguar 7.5 program,[103] which exhibits that DFT also underestimates the EAs of these three species. Interestingly, eReaxFF results are in reasonable

agreement with the DFT predicted results. Overall, eReaxFF provides an improved description of the EAs for a wide variety of species, which indicates that it can be effectively used to study electron dynamics in hydrocarbon-related species. We next employ this newly developed force field to investigate electron transfer (ET) in model hydrocarbon radicals. The physical effects that dictate the ET can be explained using Marcus theory of the electron transfer.[104] According to this theory, the rate of ET is determined by the electronic coupling between initial and final states, <i|H|f>, the difference of their Gibbs free energies, the reorganization energy, and the temperature. In molecular dynamics method, the entropic and thermal contributions are incorporated directly, while force-field approaches parameterize the potential energies. In addition to improving on the latter, in eReaxFF, we attempted to parametrize and fit the effect of electronic coupling via the introduction of explicit electron and associated electron-nuclear interaction parameters.

3.4. Results and Discussions

3.4.1 eReaxFF MD Simulations

We chose two representative hydrocarbon radicals, $C_{12}H_{19}^{\cdot}$ and $C_{14}H_{23}^{\cdot}$, to study electron dynamics, both of which consist of a conjugated part (polyacetylene), an aliphatic chain, and a radical site. These molecules are shown in Figure 3-3. To model an excited state, we inject an electron at the conjugated part of the radicals. Structural relaxation simulations were carried out using NVT (constant volume, temperature)-MD simulation at T = 1K temperature. In the MD simulations, electrons are treated as classical particles, and Newton's equations of motion are solved using the velocity Verlet algorithm.

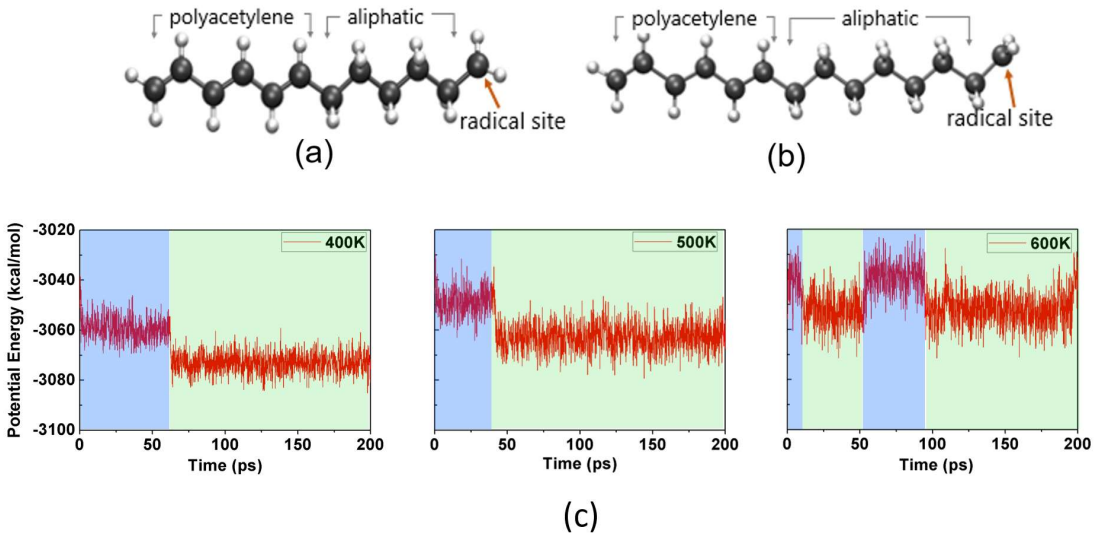

Figure 3-3 The radicals used for the eReaxFF MD simulations (a) $C_{12}H_{19}^{\bullet}$ and (b) $C_{14}H_{23}^{\bullet}$ (c) Potential energy profiles from the eReaxFF MD simulations on $C_{12}H_{19}^{\bullet}$ at three different temperatures, 400K, 500K, and 600K. Blue and green shaded regions indicate electron localization on the polyacetylene/aliphatic and radical sites, respectively. Color scheme: black: carbon, and white: hydrogen

We investigated the effect of temperature on the time-scale required for the electron to transfer from the polyacetylene to the radical site. The latter corresponds to the ground-state configuration for the electron in these species. We conducted NVT MD simulations at three different temperatures, 400K, 500K, and 600K with a Berendsen thermostat[105] and a damping constant of 100fs. An MD time step of 0.1fs was used. The potential energy profiles during the simulation of the $C_{12}H_{19}^{\bullet}$ radical at different temperatures are shown in Figure 3-3c. The electron diffuses to the polyacetylene or aliphatic chain at these temperatures with similar energy jumps. The localized electron at the radical site has a significantly lower energy than at the other two sites. From our MD simulations, we find a relatively faster ET from the polyacetylene part to the beginning of the aliphatic chain. Subsequently, the electron experiences slightly higher stability at

the intersection of these two chains which reduces the ET rate from the intersection to the radical site. The increase in temperature enhances the probability of the electron to overcome the potential well, hence to transfer to the radical site. The potential energy profile at 600K shows that, due to the higher thermal energy at this high temperature after the initial transfer of the electron from the polyacetylene to the radical site, the electron continues to hop between the three parts, polyacetylene, aliphatic, and radical sites. In Figure 3-4a we present the time-averaged electron localization around the contact point of the polyacetylene and aliphatic chains at different temperatures. With increasing temperature, electron localization around the contact point decreases, which illustrates the shorter time-scale requirement for ET at an elevated temperature. In Figure 3-5a we present the time-scale required for the full ET process from the aliphatic to the radical site at various temperatures. Temperature plays a significant role in reducing the time-scale required for ET process. Snapshots from the ET process on the $C_{12}H_{19}^{\bullet}$ radical are shown in Figure 3-5b.

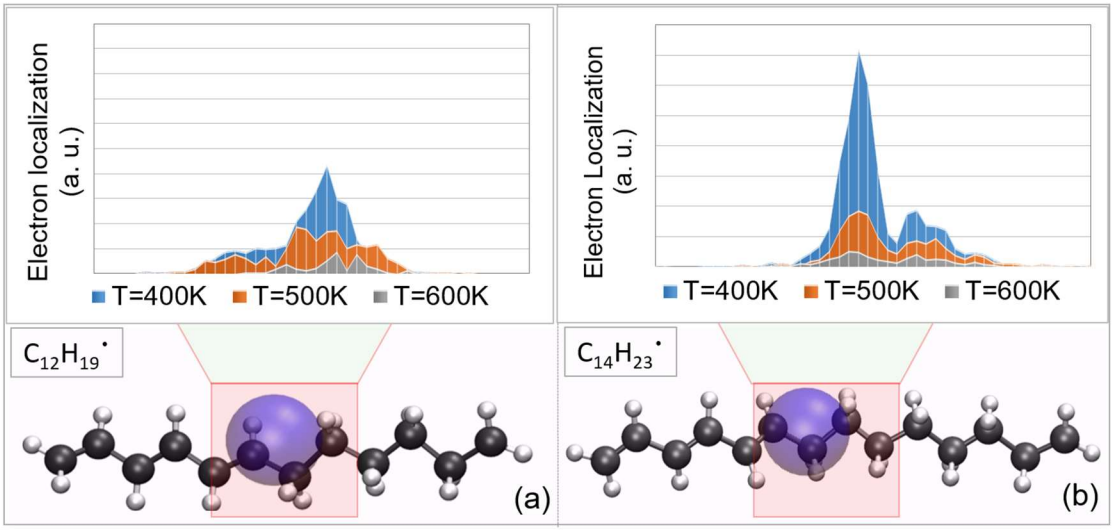

Figure 3-4 Time-averaged electron localization around the contact point of the conjugated and aliphatic chains of the (a) $C_{12}H_{19}^{\bullet}$ and (b) $C_{14}H_{23}^{\bullet}$ radicals at three different temperatures, 400K, 500K, and 600K. The blue sphere represents the electron.

We also studied the effect of aliphatic chain length on the ET dynamics by considering two hydrocarbons with different length aliphatic chains, $C_{14}H_{23}^{\bullet}$ and $C_{12}H_{19}^{\bullet}$. Figure 3-5a illustrates these effect: the increase in the aliphatic chain length slows down the ET. In a similar vein, Figure 3-4 shows the time-averaged electron localization around the contact point between the conjugated and aliphatic chains is higher in the radical with longer aliphatic chain. This higher electron localization can be attributed to the slower ET rate. Moreover, the longer aliphatic chain increases the diffusion length for the electron to arrive at the radical site, which also contributes to the larger time-scale required for the ET to the radical site. Likewise, in the $C_{12}H_{19}^{\bullet}$ case, increasing the temperature decreases the electron localization around the contact point, which results in an accelerated ET at higher temperatures.

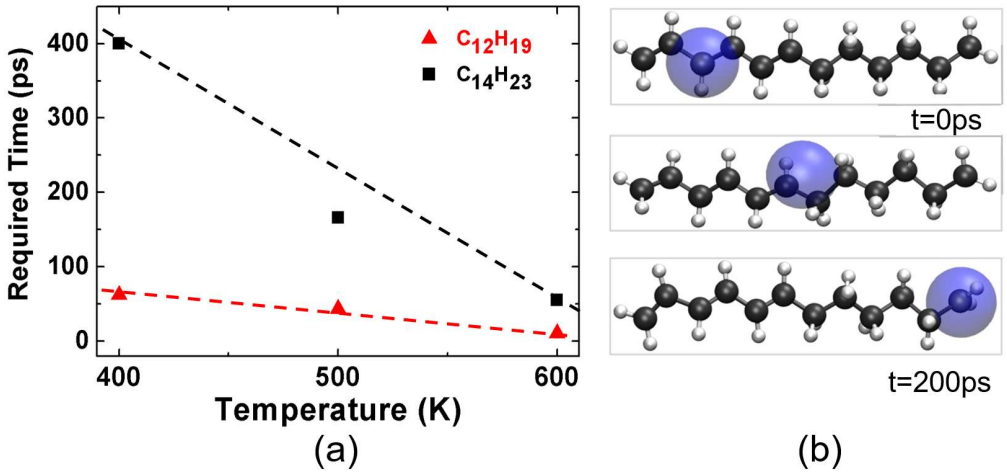

Figure 3-5 (a) The time-scale required for an electron to transfer from the polyacetylene to the radical site at different temperatures for the $C_{12}H_{19}^{\bullet}$ and $C_{14}H_{23}^{\bullet}$ radicals (b) Snapshots of typical localization of an electron in the $C_{12}H_{19}^{\bullet}$ radical during MD simulations.

3.4.2 Ehrenfest Dynamics Simulations

In order to provide a qualitative validation of our eReaxFF MD simulation results, we carried out Ehrenfest dynamics simulations on the $C_{12}H_{19}^{\bullet}$ radical. The process of electron injection

is simulated using non-adiabatic excited state dynamics based on time-dependent density functional theory (TDDFT) and Ehrenfest dynamics (ED) for the ions[68,106–109]. In this approach, the nuclei are treated as classical particles,[110] while the electronic system is treated quantum-mechanically with real-time time-dependent density functional theory (rt-TDDFT).[45]

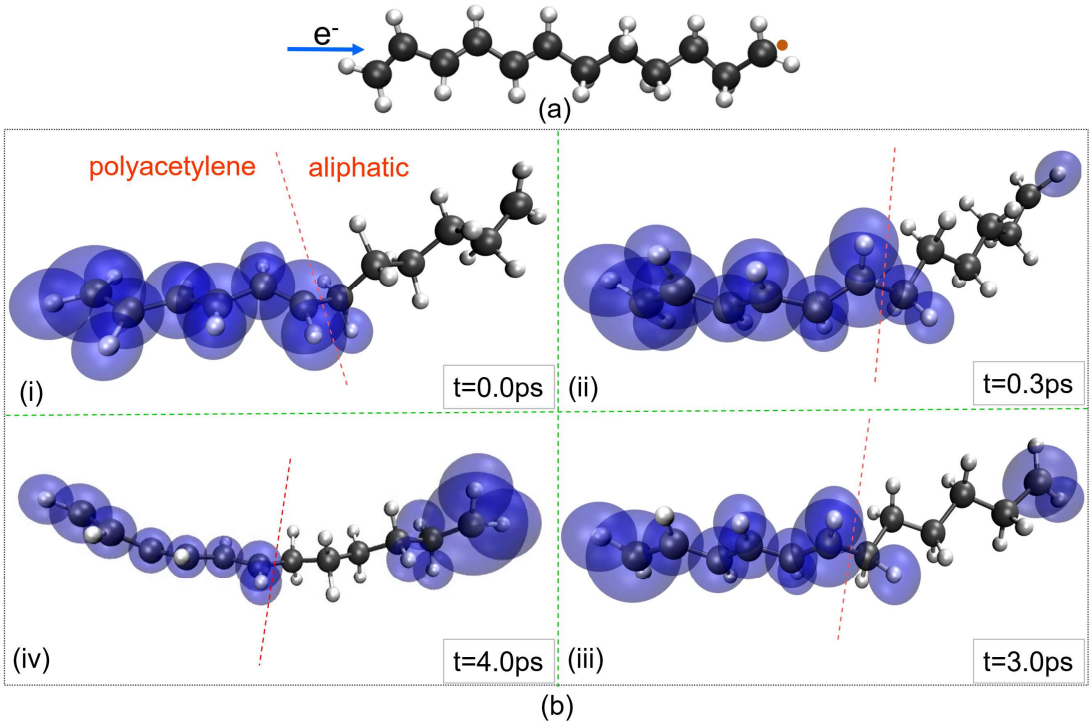

Figure 3-6 (a) Electron injection process into $C_{12}H_{19}^{\bullet}$ within ED-rt-TDDFT. The unpaired electron is depicted as an orange circle and is localized at the rightmost atom in the aliphatic part of the $C_{12}H_{19}\bullet$ radical. An electron is injected into the conjugated side of the radical. (b) Hirshfeld charge during the ED-rt-TDDFT at 600K. Blue spheres represent the Hirshfeld atomic charge referenced to the neutral radical; the size of these blue spheres is proportional to the charge: i) t=0 ps, start of the Ehrenfest dynamics; the charge is mostly localized on the polyacetylene part of the radical. ii) t=0.3 ps, initial -0.1 $|e|$ is transferred to the aliphatic chain. iii) t=3.0 ps, about -0.2 $|e|$ charge is transferred the aliphatic chain. iv) t=4.0ps, about -0.5 $|e|$ charge is transferred to the aliphatic chain, and a significant portion is localized at the radical site.

For the ED-rt-TDDFT simulations, we prepared the radical $C_{12}H_{19}^{\bullet}$ by running ground-state MD simulations for 1.0 ps at 600 K. Then we introduced one extra electron into the system and found the electronic ground state without relaxing the geometry. Next, we simulated the electron injection (schematically presented in Figure 3-6a) into the polyacetylene part of the molecule by exciting the electron from the ground state of $C_{12}H_{19}^{-}$ into the first excited state. In the ground state about 0.6 of the extra electron charge is located on the aliphatic part of the radical molecule and 0.4 on the conjugated part. By exciting the molecule into the first excited state about -0.5 |e| is transferred to the conjugated part. We show in Figure 3-7, the obtained excited state as charge-density difference of the excited and ground states.

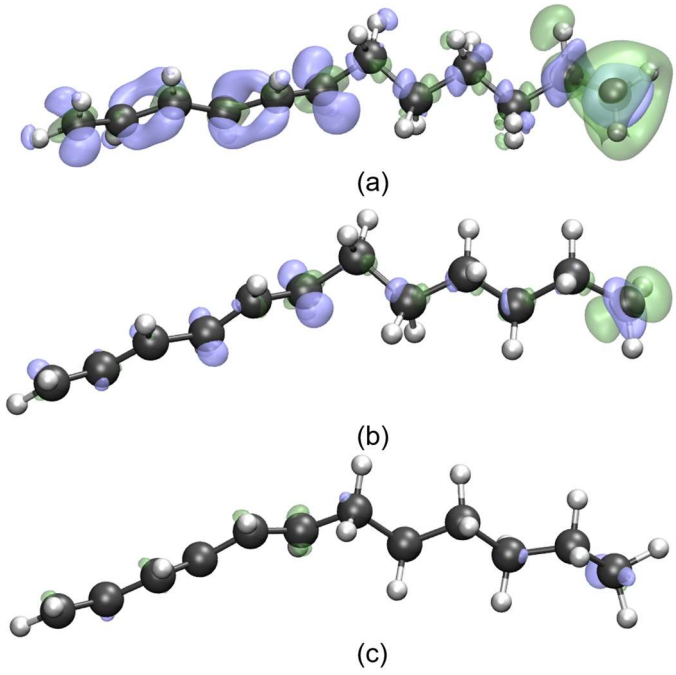

Figure 3-7 Charge-density difference between the time-propagated density and the ground state at: (a) the start of the trajectory; (b) just before the fast electron transfer; and (c) just after the fast electron transfer. Blue color depicts the excess of the negative charge (‘electron’), green color depicts its depletion (‘hole’).

We then run ED-rt-TDDFT for ~4.0 ps with 25 as (attosecond) time steps at 600K and monitored the Hirshfeld charge on each atom. During the simulation, numerical errors were monitored and the accumulated error was found to be small (total energy drift of 0.05 eV). We present snapshots of charge dynamics in Figure 3-6. Initially, the excited electron is localized in the polyacetylene part; after about 0.3ps −0.1 |e| of charge is transferred to the adjacent CH_2 groups in the aliphatic part, with a small amount of charge appearing on the radical site (terminal CH_2 group); subsequently, the transfer is slow, steady and almost linear in time, and at 3.0 ps about -0.2 |e| is transferred to the aliphatic side. In Figure 3-8 we show the time-dependent excess Hirshfeld charge, apportioned into the polyacetylene and aliphatic (which includes radical site) parts.

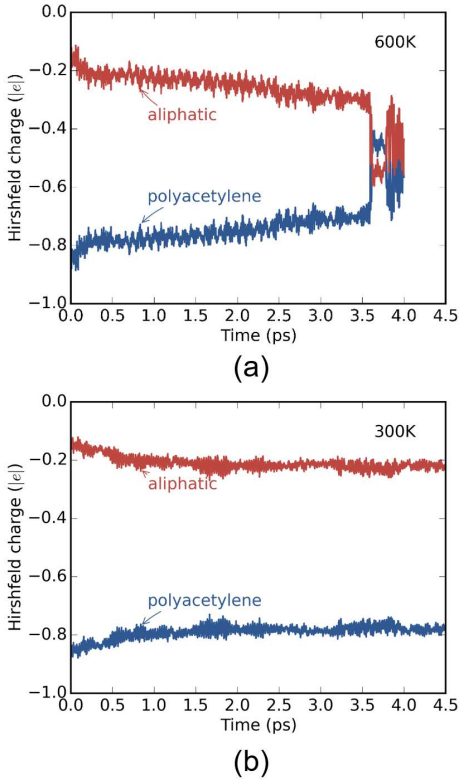

Figure 3-8 Hirshfeld charge on the polyacetylene and aliphatic chains of the radicals at (a) T= 600K, and (b) T= 300K. The higher slope of the charge profile at 600K indicates faster electron transfer rate compared to the 300K simulation.

The most interesting feature of the 600K trajectory is the ultra-fast electron transfer which is observed at about 3.5 ps time in trajectory. At this time about -0.2 |e| is transferred in a time interval of <7 fs. The analysis of potential energy surfaces around this point of the trajectory reveals that the system passes through the conical intersection of the first-excited and ground-state potential energy surfaces (see Figure 3-9), which facilitates the ultra-fast electron transfer. We also observe that before passing through the conical intersection the electronic wavepacket already has substantial ground state character as can be seen in Figure 3-7b. After the crossing the ground state retains the same character as before, while the electronic densities of the time-propagated and ground-state systems are virtually indistinguishable, see Figure 3-7c, although the wavepacket retains some of the excited-state character which is manifested in coherent oscillations at the end of trajectory, see Figure 3-8a.

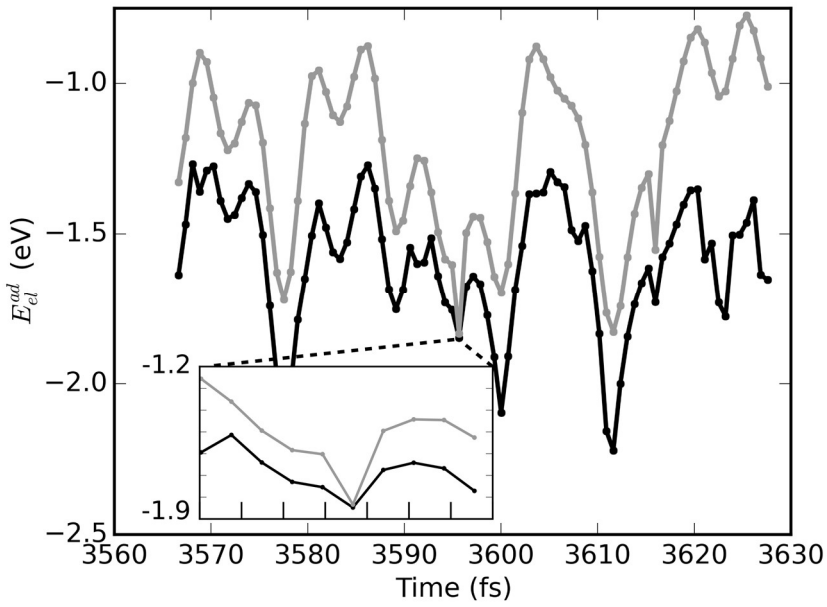

Figure 3-9 Adiabatic electronic energies of the ground (black line) and excited (gray line) states along the 600K trajectory around the time point where ultra-fast electron transfer occurs. The inset shows an expanded version of the region of intersection of the potential energy surfaces, with the intersection occurring between t=3.595 and 3.596 ps.

To study the effect of temperature on the ET dynamics, we performed ED simulations at 300K. Figure 3-8b represents the Hirshfeld charges on the polyacetylene and aliphatic parts of the radical for this temperature. The slope of the charge transfer profile is higher in the case of 600K compared to the 300K, which indicates a faster rate of ET at an elevated temperature.

In order to compare our ED simulations to time scales estimated in eReaxFF simulations we fitted an exponential to the smooth part (leaving out ultra-fast ET) of the 600 K ED time-dependent Hirshfeld charge shown in Figure 3-8a, which gives a characteristic ET time of 11 ps and agrees very well with the eReaxFF predicted ET time of ~11 ps at 600K, presented in Figure 3-5a. If we include the ultra-fast ET part in the exponential fit, the time scale is reduced to ~4 ps. Clearly many trajectories from ED simulations would have to be sampled to give a proper statistical average for a more meaningful comparison. We conclude that the qualitative trends of the ET time-scale as a function of temperature are comparable, and the estimate from the 600K ED trajectory suggests even reasonable qualitative agreement. In both simulation techniques, an accelerated ET rate is observed with increasing temperature. We speculate that at higher temperature, the potential energy surface is sampled at a higher rate thus increasing the chance of encountering the region of high coupling as we observed in the ED trajectory.

3.5 Conclusions

In this work, we developed a pseudo-classical description of an explicit electron within the framework of the ReaxFF reactive force field. In the eReaxFF development, simple, yet robust functional forms are chosen to describe electron interactions so that this method can produce significant computational gains. The capabilities of the method are demonstrated by calculating electron affinities of various types of saturated, unsaturated, and radical species which qualitatively reproduce experimental values for all the species considered in this study. We studied electron transfer dynamics as a proof of concept for this newly developed method. The eReaxFF results are

qualitatively in good agreement with results obtained from the Ehrenfest dynamics (rt-TDDFT) simulations. This agreement is very encouraging since computationally eReaxFF is several orders of magnitude faster than the Ehrenfest dynamics or other *ab initio* MD simulations. Future development of eReaxFF will be focused on the complex interfacial reactions of Li-ion batteries. Investigations are currently underway to describe reduction and oxidation reactions of the anode- and cathode- electrolyte interfaces, respectively, of Li-ion batteries with ethylene carbonate electrolytes. In these studies, we will further illustrate the dynamics of the both electron and hole. The current version of the eReaxFF method cannot describe the interactions between electron-hole pairs, and as such is unable to describe the mechanism of the photon-driven processes such as photochemistry. We hope to incorporate this capability in future versions of the method. However, we anticipate that eReaxFF would be an effective method to develop a physics-based description for piezo/ferro electric materials and their response to the application of an external field. eReaxFF should provide a powerful tool for understanding the dynamics of explicit electrons in physical and chemical systems where QC methods are still daunting computationally.

Chapter 4

Reductive Decomposition Reactions of Ethylene Carbonate via Explicit Electron Transfer from Lithium

4.1 Introduction

Lithium-ion batteries (LIB) are being widely used in portable electronics for their advantages, such as high energy density, high operating voltage and low self-discharge.[7] A typical Li-ion battery system is comprised of a graphitic anode, a transition metal oxide cathode, and a mixture of alkyl carbonate solvents and lithium salts as an electrolyte solution.[24–27] The carbonate-based electrolytes—which act as an ionic path between the electrodes—exhibit attractive properties, such as high polarity, a wide operating temperature range, low toxicity, and adequate safety features.[27]

The lowest unoccupied molecular orbital (LUMO) of the commonly used organic electrolytes is lower than the Fermi level of lithium, which drives the reduction reactions of the electrolytes.[112] It is well known that during the first charge cycle, the reductive dissociation of the electrolyte at the anode-electrolyte interface generates a thin passivating layer—consisting of different organic and inorganic compounds—which prevents the decomposition of electrolytes in subsequent cycles. This layer blocks the electron transport while simultaneously allowing Li-ions to pass through during cell operation. This passivation layer is known as the Solid Electrolyte Interphase (SEI).[30] The properties of the SEI layer significantly affect the LIBs life-cycle, capacity retention, high power density, rate capability, and safety.[32–34] Therefore, a comprehensive understanding of the formation mechanism of the SEI layer is essential for the performance improvement of LIBs.

Numerous mechanisms have been proposed to elucidate the underlying chemistry of the SEI. Ethylene carbonate (EC) and other co-solvent (such as dimethyl carbonate (DMC)) concentration dependent double layer model has been reported previously.[34] The SEI film is comprised of both the single and double electron reduction reaction products of the EC.[32,33] The inner layer compositions stemmed from the double electron reduction, and the outer layer primarily consists of singly-reduced solvent decomposition products.[113] The organic lithium bicarbonate compounds $(ROCO_2Li)_2$ (R = CH_2, CH_2CH_2)—resulted from the single electron reduction of the EC—have been observed experimentally. The dilithium ethylene dicarbonate (Li_2EDC), ethylene gas, and dilithium butyl dicarbonate (Li_2BDC), are predominant in the high EC concentration region. The Li_2EDC is highly sensitive to water.[11] Thus it has a propensity to decompose to Li_2CO_3 in the presence of water.[113,114] Dey[115] proposed an alternative pathway, where double reduction of the EC may yield Li_2CO_3 and ethylene gas. The double electron reduction reactions at a lower EC concentration region primarily generate Li_2CO_3.[40,116]

In order to study the chemical composition of SEI, extensive research efforts have been expended using a wide variety of computational and experimental techniques. Balbuena et al.[117] performed density functional theory (DFT) calculations to investigate EC reduction pathways. The electron transfer to the EC/Li^+ facilitates the ring opening of the EC, and radical EC^-/Li^+ is formed. The radical EC^-/Li^+ undergoes various termination reactions, such as the formation of Li_2BDC, Li_2EDC, and ester carbonate compounds.[118] However, the detailed chemistry and the effect of electrolyte solvent, salt, and various additives are still elusive.[7,36] Experimental studies have difficulty in performing *in situ* characterization of the SEI during a cell operation.[37] Theoretical studies based on quantum chemistry (QC) methods are computationally intensive and limited to a small length and time-scales, which are often inadequate to describe interfacial reactions. On the other hand, reactive force field based methods are unable to describe redox reactions because of the absence of explicit electrons. However, a few studies are reported in literature, wherein the

initial stages of the SEI formation mechanism are investigated using *ab initio*[53,57,59,119] and reactive force field [94,120] based molecular dynamics (MD) simulations. Previous ReaxFF[92,94,120] studies on the battery interfacial chemistry can elucidate certain aspects of the SEI; however, lack of an explicit electronic degree of freedom limits proper description of the reduction reaction. The ReaxFF method also failed to describe correct electron affinities of the EC, which resulted in a very fast reaction kinetics of the EC dissociation.[94,120] In this study, we employed our newly developed eReaxFF method to investigate the initial stages of the reduction reactions of the EC in Li-ion batteries.

4.2 Computational Methodology

eReaxFF is an extension to the standard ReaxFF method with a limited electronic degree of freedom. Like ReaxFF,[60,82] eReaxFF is also a general bond order[61,62] (BO) based classical force field method with a pseudo-classical treatment of explicit electrons that enables the description of redox reactions and electron dynamics during simulations. The general form of the eReaxFF energy terms are:

$$E_{system} = E_{bond} + E_{over} + E_{under} + E_{lp} + E_{val} + E_{tor} + E_{vdWaals} + E_{Coulomb} + E_{elec}$$

where the partial energy contributions include (indicated by the corresponding subscripts) bond, over-coordination penalty and under-coordination stability, lone pair, valence, torsion, non-bonded van der Waals, Coulomb, and electron-nuclear interactions. The basic framework of the ReaxFF method are retained in the eReaxFF method, such as the concept of BO to calculate all bonded interactions that include 2- (bond), 3- (valence angle), and 4-(torsional) body interactions. Non-bonded interactions, such as van der Waals and Coulomb are calculated between every pair of atoms. We incorporated a single floating point Gaussian function to calculate electron-nuclear interactions. A 7th order taper function is used for all the non-bonded van der Waals, Coulomb and

electron-nuclear interaction terms to circumvent any energy discontinuity. The presence of an electron and hole renders the atom valency and outer shell electrons a variable, and they are updated in every iteration. Unlike ReaxFF, in this method, the electrostatic interactions are coupled with the covalent contributions—i.e. charge is coupled with the valency of an atom type. The modified valency of an atom type affects the over- and under- coordination energy contributions. The eReaxFF uses geometry dependent charge calculation scheme – the Atom-condensed Kohn-Sham DFT approximated to second order (ACKS2) – for calculations of atomic charges.[65,86] ACKS2 method prevents unrealistic long-range charge smearing. Additional details of the eReaxFF method can be found in the original publication.[66]

4.3 Results and Discussions

4.3.1 Force Field Development and Validation

We initiated our eReaxFF force field training for describing C/H/O/Li interactions by merging previously developed standard ReaxFF parameters for the C/H/O and Li interactions.[94] The transferability of the ReaxFF parameters to the eReaxFF method allowed us to develop a force field for describing explicit electron interaction, primarily focusing on the explicit electron related parameters. We retained the ReaxFF atom parameters, and performed additional training, such as eReaxFF related Gaussian, over and undercoordination, and selected bond and angle parameters. For each of the elements, there is three additional eReaxFF atom parameters, and for each bond there is an extra bond parameter. The objective of this work is to describe the reduction reactions of the EC/Li system such as the formation of radicals and subsequent radical termination reactions. We trained our force field against the DFT-based training set data used by Bedrov et al.[94] The key reactions of the EC/Li chemistry is initiated through the oxidation of the Li, followed by the electron transfer to the EC to allow reduction reactions to occur. The reduced EC^{-}/Li^{+} complex then

undergoes EC ring opening reaction thus forms an o-EC^{-}/Li^{+} radical complex. Therefore, it is crucial for the eReaxFF method to capture both the electron transfer event and subsequent radical formation reactions. To mimic the oxidized and reduced species, the study performed by Bedrov et al.[94] imposed a charge constraint to assign +1 and -1 charges on the Li and EC, respectively. However, such a molecular charge constraint is problematic in the reactive environment because the breaking of bonds during reactions invalidate the imposed charge constraints. The explicit electrons in the eReaxFF method enabled us to describe oxidation and reduction process without such a charge constraint. We compare our eReaxFF results for the key SEI formation reaction with the seminal quantum chemistry study performed by Balbuena et al.[117] The eReaxFF results of the major reaction pathways are illustrated in Figure 4-1. The reduction of the EC/Li^{+} complex is modeled by adding an extra electron to the EC molecule. In our description, the electron is a negatively charged particle, therefore, it is mostly localized at a particular site in the molecule during geometry optimization. We chose an electron-nucleus distance dependent exponential function to determine the number of electrons in the host atom. This function also ensures that an electron can virtually split itself among its neighboring atoms, as such resembles a partial delocalization in a molecule.[66] Quantum mechanics based calculations typically indicate a higher degree of delocalization of the added electron over the EC molecule, compared to the eReaxFF method. This particular limitation is stemming from the treatment of the electron as a pseudo-classical particle. We describe Li-atom as a Li^{+} carrying an additional electron.

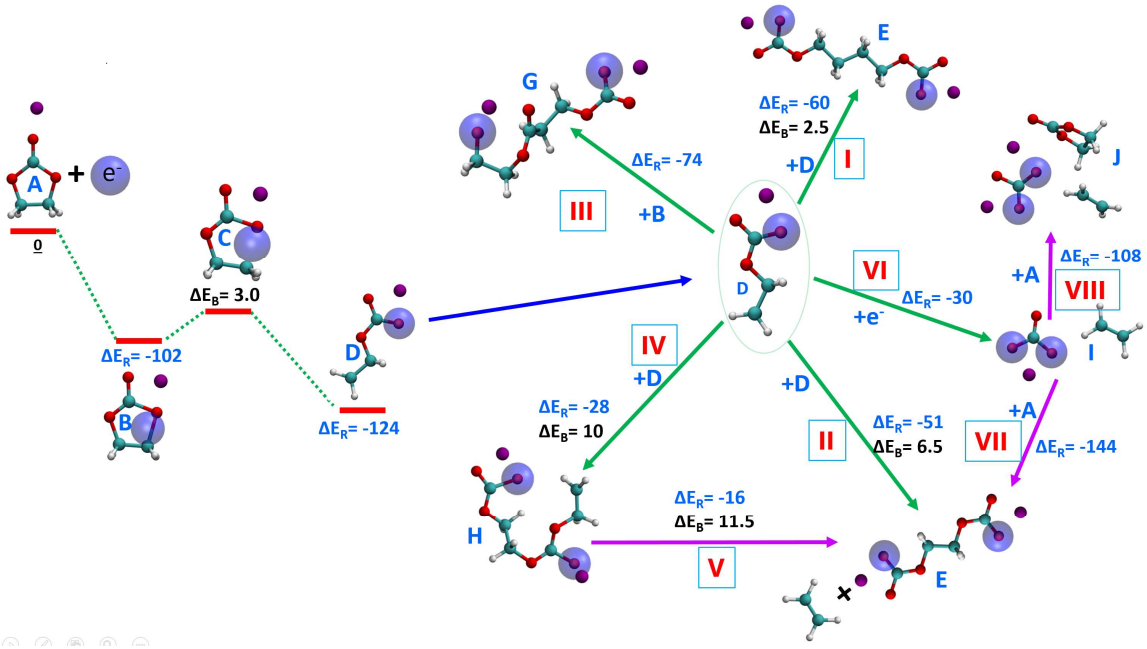

Figure 4-1 Potential energy profile for the reduction of EC/Li^+ and the radical termination reactions at various pathways. ΔE_R and ΔE_B denote reaction energy and reaction barrier, respectively. Color scheme: cyan: carbon, white: hydrogen, red: oxygen, purple: Li^+, large blue sphere: electron

eReaxFF predicts a reaction energy of -102 kcal/mol for the reduction of EC/Li^+ complex in contrast to the Balbuena et al.'s[117] reported value of -93 kcal/mol. In the EC^-/Li^+ complex, the electron localizes in between C_e-O_e atoms (e subscript indicates ether carbon and oxygen). Endo et al.[121] reported transfer of the electron to the EC/Li^+ complex rather than to the isolated EC molecule in the electrolyte solvent. The former process is exothermic as our simulation predicts while the latter is endothermic. It is well known that an isolated EC has a negative electron affinity (EA).[118] Previous ReaxFF study[94] reported a highly positive EA of an isolated EC (-61 kcal/mol) while eReaxFF predicts a negative EA value of 2.3 kcal/mol. Thus our eReaxFF calculation correctly captures the trend in the electron affinity of an isolated EC molecule. The EC^-/Li^+ undergoes an O_e-C_e bond-breaking reaction to form a radical species (D). The eReaxFF simulation gives a reaction barrier of about 3 kcal/mol and a reaction energy compared to the EC/Li^+ as -124 kcal/mol. The

reaction energy value agrees well with the QC reported value of -123 kcal/mol.[117] The reaction barrier of the EC ring opening reaction is intentionally kept lower in order to facilitate the reactions to occur within the simulation time scale. The QM reported barrier is about 11.5 kcal/mol, for which the Eyring rate equation indicates an estimated lifetime of the C_e-O_e bond breaking in the EC^-/Li^+ pair to be around 100 μs.[94] This time scale is typically inaccessible in our current eReaxFF MD simulations. In the radical EC^-/Li^+ complex (or o-EC^-/Li^+), the excess electron localizes on the O_e atom. The effect of the electron transfer on the C_e-O_e bond breaking reaction is further analyzed. Without an electron transfer to the EC, the C_e-O_e bond breaking barrier in the EC/Li^+ continuously increases with over 45 kcal/mol until 3.0 Å. However, transfer of the electron to the EC rearranges the EC/Li^+ geometry and the bond breaking barrier subsequently reduced significantly to only 3 kcal/mol, where DFT reported value is around 11.5 kcal/mol.[117] This indicates that the electron transfer has a significant effect on the interfacial electrolyte dissociation reactions.

The o-EC^-/Li^+ radical anion/cation complex can subsequently undergo various radical termination reactions. All the radical termination reactions are shown in Figure 4-1. The direct combination of two o-EC^-/Li^+ complexes yields the most probable reaction product, dilithium butyl dicarbonate $(CH_2CH_2OCO_2Li)_2$ (Li_2BDC) (path I). Using transmission electron microscope (TEM) and FTIR method, Naji et al.[122] reported the presence of the Li_2BDC in the SEI formed by the reaction products of $LiClO_4$-EC electrolyte. Our calculation predicts a reaction energy of -60 kcal/mol compared to the literature data of -81 kcal/mol. We also calculated reaction barriers for the several radical termination reactions. Reaction barriers are calculated by applying a biasing potential in between the atom pair of interest to drive the reaction along the intended reaction coordinates. The biasing potential has the following form,

$$E_{biased} = f_1(1 - e^{f_2(r_0 - r_{ij})^2})$$

where f_1 and f_2 are constants, and r_{ij} is the distance between atom pair of interest and is varied along the reaction coordinate. The eReaxFF simulation indicates a small reaction barrier of 2.5 kcal/mol for the Li_2BDC formation. Reaction barriers for the radical termination reactions are not available in literature. In Path II, the radical termination leads to the formation of dilithium ethylene dicarbonate $(CH_2OCO_2Li)_2$ (Li_2EDC). The attack of the o-EC^-/Li^+ to the O_e of another o-EC^-/Li^+ results in the formation of Li_2EDC and ethylene gas. Experimentally, both Li_2EDC and C_2H_4 are the most commonly observed anode surface SEI component.[32,113] Our calculations show a reaction barrier of 6.5 kcal/mol and an exothermic energy release of -51 kcal/mol for the pathway, which is lower than the previously reported value of -66 kcal/mol[117]. The eReaxFF simulations predict that the formation of Li_2BDC is more favorable than the generation of Li_2EDC and C_2H_4, which is consistent with the observations of Balbuena et al.[118] In Path III, the combination of an o-EC^-/Li^+ radical and the reduced intermediate (B), generates a lithium organic salt with an ester group, $LiO(CH_2)_2CO_2(CH_2)_2OCO_2Li$. The reaction energy for this pathway is calculated as -74 kcal/mol, in good agreement with the QC value of -77 kcal/mol.[117] We also investigated an alternative route for the formation of Li_2EDC and C_2H_4. In the path, IV, an o-EC^-/Li^+ accepts an additional electron thus generates a carbonate radical ($LiCO_3^-$) and C_2H_4, with an exothermic energy release of -31 kcal/mol. The carbonate radical can nucleophilically attack the EC/Li^+ to form Li_2EDC and C_2H_4 with a reaction energy of -144 kcal/mol (path VII) which is in good agreement with the literature data of -140 kcal/mol.[117] In another pathway, an o-EC^-/Li^+ reacts with another open radical to form an intermediate product (H), with a favorable reaction energy of -28 kcal/mol and a reaction barrier of 10 kcal/mol. The compound of (H), may undergo another reaction to strip off C_2H_4 and generate Li_2EDC (path V). This exothermic route, V, has a reaction energy of -16 kcal/mol and a barrier of 12 kcal/mol. The doubly reduced intermediate (I), yields Li_2CO_3 when paired up with a Li^+ from an EC/Li^+ (path VIII). The formation of Li_2CO_3 is exothermic with an energy release of -108 kcal/mol. The Li_2CO_3 is usually considered as a component of the inner

surface SEI, where the concentration of EC is low. Overall, compared to the QC data,[117] eReaxFF provides an adequate description of the energetics of the key reactions that are responsible for the SEI formation.

4.3.2 MD Simulations

We performed MD simulations to study the dynamics of the EC/Li chemistry. We considered a system with 60 EC molecules and 40 Li atoms. We used our in-house code to place the molecules randomly in a box. Next, we performed NVT (constant volume, temperature) MD-based structural relaxation simulation at 1 K temperature. The snapshot of the simulation box is presented in Figure 4-2a. We carried out MD simulations at 600 K and 300 K to investigate the dynamic evolution of the reduction reactions. To achieve the simulation temperature of 600 K, we slowly increase the system temperature from the 300 K at a rate of 0.005 K/iteration. The higher temperature is used to enhance the reaction kinetics in order to observe the electrolyte dissociation chemistry within the simulation time-scale. The temperature of the system is controlled using a Berendsen thermostat[105] with a damping constant of 100 fs. The Newton's equations of motion are integrated using the velocity Verlet algorithm. Fictitious mass of an electron is assigned as 1 a.m.u, which allows us to use a time step of 0.10 fs. All MD simulations are performed using periodic boundary conditions.

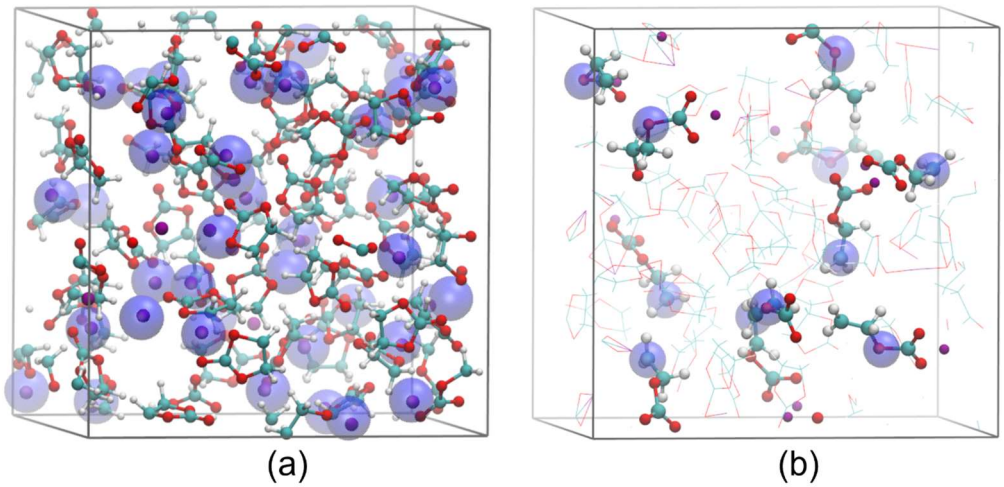

Figure 4-2 Snapshot of the simulation cell at (a) t = 0 ps, (b) the generated o-EC^-/Li^+ radicals are highlighted, t=25 ps. EC and Li which are not participated in the electron transfer event are displayed as line. Color schemes are as mentioned in Figure 4-1.

From the simulations of this system at T = 600 K, we observed at first an electron transfer event from the Li to the nearby EC molecule. Electron transfer happens when the donor Li atom approaches to the EC at a favorable orientation to donate its electron to the EC. The energetically favorable electron transfer process results in the reduction of the EC. The reduced EC^-/Li^+ complex then undergoes homolytic EC ring opening reaction. The EC ring opening has only been observed when electron transfer to the molecule has occurred. The effect of the electron transfer on the breaking of C_e-O_e bond can be explained as follows: the transferred electron delocalizes around the C_e-O_e bond of the EC. The presence of the electron decreases the valency of both the carbon and oxygen atoms. The valency modified carbon and oxygen atoms behaves like pseudo-nitrogen and fluorine atoms, respectively. Such a decrease in the valency of both of the atoms increases the overcoordination, resulting in a higher overcoordination energy penalty. Consequently, the reduction in the C_e-O_e bond order leads to bond breaking. Upon breaking of the bond, the excess electron localizes either at the O_e or C_e atom of the EC.

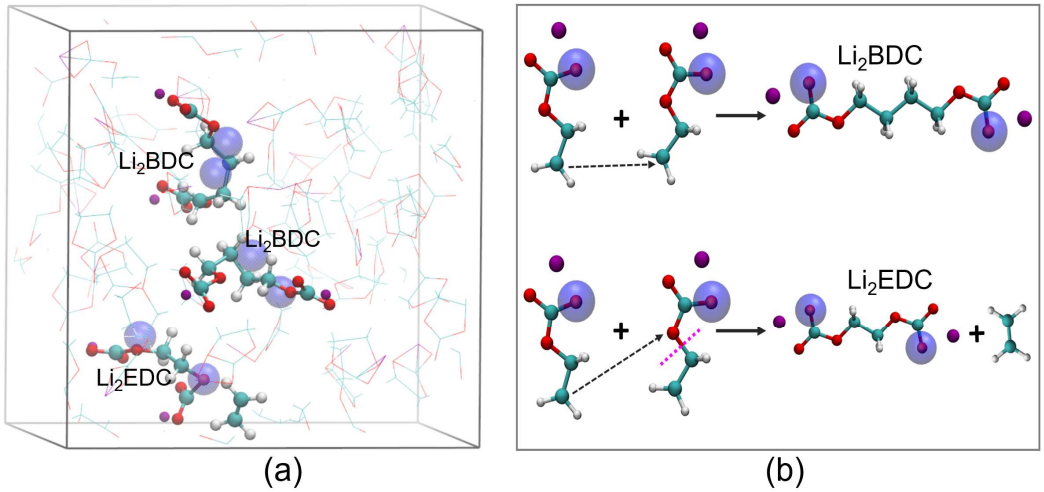

Figure 4-3: (a) The formation of Li_2BDC, Li_2EDC and C_2H_4 gas as observed in our MD simulations (b) Schematic representation of the reaction pathways as our MD simulations predicted for the formation of Li_2BDC and Li_2EDC. Delocalization of the explicit electrons are observed in the species generated during MD simulations. Color schemes are as mentioned in Figure 4-1.

In a simulation time-scale of 120 ps, we observed the formation of eleven o-EC^-/Li^+ complexes due to the electron transfer from Li atoms to EC molecules. The snapshot of the simulation cell at 25 ps with the generated o-EC^-/Li^+ radicals is shown in Figure 4-2b. The radical termination reactions have been observed during MD simulations. Because of the lowest reaction barrier of the pathway I, during the simulation, the direct combination of two o-EC^-/Li^+ is the most probable reaction to occur. Our simulation shows the formation of Li_2BDC as presented in Figure 4-3a and the corresponding pathway is shown in Figure 4-3b. The Li_2BDC formation is favored both kinetically and thermodynamically over the Li_2EDC. A few radical termination reactions have occurred because at a low concentration of the o-EC^-/Li^+ radicals, the probability that a radical will encounter another radical and undergo further reactions is rare. The spontaneous evolution of the Li_2BDC in our simulations depicts the capability of the eReaxFF method in describing the dynamics of the SEI formation mechanism. Furthermore, in order to accelerate the reaction kinetics and to

increase the probability of the radicals to find other radicals, we used a biasing potential between radicals. We took a snapshot at 50 ps of the simulation and applied a biasing potential in between the radical pair of interest. With the biased potential, we restarted and ran the simulation for another 50 ps. The application of the biasing potential made the radicals accessible and allowed the reactions to occur as such we observed the formation of the Li_2EDC and C_2H_4. Figure 4-3a highlights the formation of Li_2EDC and C_2H_4 as predicted from our simulation and the corresponding pathway is shown in Figure 4-3b. Our static calculation reveals that this reaction is thermodynamically favorable with a relatively moderate reaction barrier of 6.5 kcal/mol. Thus we predict that in the presence of a higher radical concentration and at a longer simulation timescale the spontaneous production of the Li_2EDC could be observed. In order to validate this argument, we performed several simulations with six randomly placed o-EC^-/Li^+ radicals in a cubic box of 12 Å and performed 600 K NVT MD simulations without any biasing potential. In these simulations, in a time-scale of 600 ps, we observed the formation of both of the major reaction products, namely, Li_2BDC and $Li_2EDC+C_2H_4$. However, in this study, the formation of Li_2CO_3 (path VIII) has not been observed, which can be attributed to the relatively lower concentration of lithium in the system.

In our simulation of this system at 300 K showed formation of eight o-EC^-/Li^+ radicals in a time scale of 100 ps. At lower temperatures, the probability of a favorable orientation of a Li atom to donate its electron to an EC molecule is rather less, which results in a lesser number of radical formation reactions. Furthermore, at a lower temperature the probability of the rearrangement of the radicals to facilitate radical termination reactions is also less, which is evident from the fact that no radical termination reactions have been observed in our 300 K simulation.

4.4 Conclusions

In this study, we investigated the reduction reactions of ethylene carbonate (EC) electrolyte using our newly developed eReaxFF method. The eReaxFF is the very first classical force field method that accounts for the effect of explicit electrons in describing a redox reaction. Our calculations exhibit a good agreement with available QC data for all the major reaction pathways involved in the solid electrolyte interphase (SEI) formation reactions. Our MD simulations predict the electron transfer from lithium to the EC, the formation of o-EC^{-}/Li^{+} radical, and the radical termination reactions which resulted in the generation of dilithium butyl dicarbonate, dilithium ethyl dicarbonate, and ethylene gas. The reaction products predicted in our simulations are experimentally observed as a dominant component of the SEI. Therefore, we predict that the computationally economic eReaxFF simulation tool will be a useful tool for the detailed investigation of the rechargeable battery chemistries. Currently, investigations are underway to explore the interactions of carbonate electrolytes with graphitic anode materials and the role of lithium salts on the SEI formation mechanism. While the *ab initio* based MD simulations are quite prohibitive for investigation of these reaction mechanisms, eReaxFF method with its ability to describe adequately the redox reactions is expected to enable new direction towards the study of complex interfacial reactions of lithium batteries.

Chapter 5

Influence of Teflon on the Interfacial Chemistry of Lithium- Sulfur Batteries

Part of this chapter also published in ref,[92] authored by Md Mahbubul Islam, Vyacheslav S Bryantsev, and Adri CT van Duin. Md Mahbubul Islam performed all the ReaxFF simulations, analyzed results and wrote the paper.

5.1 Introduction

Lithium-sulfur batteries has received profound attention in the rechargeable energy storage technology due to its tremendously high energy density, environmental friendliness, abundance, and low-cost.[3,42] Although Li-ion batteries are now ubiquitous in consumer electronics, their practical capacity is still inadequate for the electric vehicle (EV), and large-scale renewable energy storage systems.[123] Li-S redox-couples are deemed the most promising to meet future energy storage demands, since theoretical capacities of Li and S are 3860 and 1672 $mAhg^{-1}$, respectively.[3]

In spite of all these advantages, commercialization of Li-S batteries is plagued owing to severe shortcomings in prolonged life-cycle retention. The high electrochemical potential of sulfur cathode entails Li anode for practically realizable energy density.[112] The use of metallic lithium anode is still problematic due to its low cycling efficiency, deleterious dendrite formation, and safety concerns.[124] During charging, lithium ion reduced at the anode surface and deposit as a metallic phase. Thus, dendrite-like structure grows and further penetrates through the separator, leading to short circuit and thermal runaway.[125] Moreover, dissolved polysulfide anions migrate through the electrolyte by well-known "shuttle mechanism" and react at the anode surface to form insoluble sulfides (Li_2S and Li_2S_2) and these sulfides develop a passivation layer onto bare lithium surface. This insulating layer hinders lithium access to the anode, increases internal cell resistance resulting in poor rate-capability.[126,127]

Furthermore, the chemical potential of the lithium is higher than the lowest unoccupied molecular orbital (LUMO) of commonly used organic liquid electrolytes.[13] During charging, freshly deposited lithium on anode surface is extremely reactive and can react with most of the organic electrolytes. Therefore, electrolytes can be reduced at the Li anode, hence the reaction products may form a solid electrolyte interphase (SEI) in between electrolyte and anode.[124] SEI allows transportation of Li-ions but suppresses electron transfer, and thus it prevents further anodic reactions.[124] However, such a stable SEI formation is not commonly observed in most available ether type electrolytes. Therefore, to improve the performance of Li-anode, both *ex-situ* and *in-situ* treatments are reported in the literature. One *ex-situ* approach to abate the associated problems with the lithium metal anode is to introduce a Li-ion penetrable passivation layer in between electrolytes and anode surface to isolate highly reactive Li-anode from electrolyte solvents and polysulfides. Li-ion conducting passivation layer using Li_3N,[128] Li_2CO_3,[129] LiPON,[130] and UV cured polymerization[131] have been previously studied. These thin protective films inhibit lithium reactivity and corrosion by polysulfides; however, their fabrication process is costly.[132] Recently, *in-situ* protective layer formation during cell operation using $LiNO_3$ additives in electrolyte has been investigated.[132,133] $LiNO_3$ exhibits promising performance in protecting Li-anode via formation of a SEI layer, however, it may reduce at the carbonaceous surface of the cathode. These irreversible reduction products affect reversibility and capacity of Li-S batteries. Moreover, continuous growth of passivation film with the consumption of $LiNO_3$ has a detrimental effect on Li-anode performance.[133]

Li-S battery electrolytes should comply with the requirement of high ionic conductivity, low viscosity, good polysulfide solubility, electrochemical stability with lithium metal electrodes, and safety.[134] Ether-based electrolytes show highest polysulfides solubility and expedite electrochemical activity of sulfur reactions.[135] Myriads of experimental studies have been conducted on the electrochemical properties of various electrolytes in Li-S batteries, such as

tetra(ethylene glycol) dimethyl ether (TEGDME)[42,47–49,52,136–138] , poly(ethylene glycol) dimethyl ether(PEGDME)[43], tetrahydrofuran(THF)[48], 1,2-dimethoxyethane (DME),[139] 1,3-dioxolane(DOXL).[49–51] Especially, TEGDME has been reported as a good liquid electrolyte because of high discharge capacity at room temperature.[45,48,136,140]

However, to address the issues attributed to the current Li-S battery technologies, more profound understanding of the electrode-electrolyte interface, electrolyte dissociation chemistry, and morphology changes of electrodes during cell operation are required. Atomic and molecular level insights can effectively enlighten the underlying intricate chemistry and the limitations in the current experimental approaches. In this study, we used ReaxFF reactive molecular dynamics simulations to elucidate anode-electrolyte interfacial chemistry and the role of a protective layer on anode surface in electrolyte dissociation. Previously, ReaxFF method was successfully employed for studying electrolyte chemistry in Li-ion batteries. Using ReaxFF, Bedrov et al.[94] investigated reactions of singly reduced EC and S.-P Kim et al.[120] studied SEI formation in Li-ion batteries.

Although Li-metal anode is most prevalent in experimental Li-S batteries, in this study, in lieu of lithium metal anode, we used Li/SWCNT composite in order to preclude dendrite formation. In comparison with the Li intercalated graphite anode (LiC_6, corresponds to the capacity of 372 $mAhg^{-1}$), recent experiments reported higher lithium capacity in Li/SWCNT anode ($Li_{1.6}C_6$, corresponds to the capacity of 600 $mAhg^{-1}$).[141] Capacity reduction due to the usage of Li/SWCNT composite material instead of lithium metal might be an acceptable trade-off among improved cell-life, performance, and safety. It is known that the performance limiting parameter in state-of-the-art lithium batteries is the lower capacity of the cathode materials.

In addition, to control lithium reactivity, we employed a polytetrafluoroethylene (PTFE) or Teflon monolayer at the anode surface. Previously, Chang et al.[142] studied Teflon coated lithium anode to protect it from lithium dendrite formation. We investigate if the presence of Teflon can significantly scale down lithium reactivity with the TEGDME resulting in less electrolyte

decomposition. We also report electrolyte dissociation pathways upon interaction with the lithium ion.

5.2 Force Field Development

We began our force field development for describing C/H/O/S/Li/F interactions by merging previously published parameters. C/H/O/S and Li parameters were adopted from Castro-Marcano et al.,[143] and Bedrov et al.,[94] respectively, and fluorine parameters were developed based on the training set as described by Paupitz et al.[144]

In this work, we performed additional force field training against quantum chemistry (QC) calculations for describing bond dissociation, equation of state for Li-F interaction, and Li-binding energies on electrolyte molecules. A successive one-parameter parabolic extrapolation method[100] was used for fitting ReaxFF parameters against QC data.

Non-periodic QC calculations presented in this work were carried out in the Jaguar 7.5 program[103] using density functional theory (DFT) with the B3LYP[145,146] hybrid functional and the 6-311++G** basis set. SeqQuest code (version 2.61j)[147] was employed for the periodic calculation using a Gaussian-based linear combination of atomic orbital method and double -ξ plus polarization[148] with Perdew−Becke−Ernzerhof (PBE) generalized gradient approximation.[149] For more details regarding these DFT calculations, please refer to Ref. [150].

To parameterize ReaxFF bond energy data, we carried out QC calculations on Li-F bond dissociation in a LiF molecule. Figure 5-1a shows the comparison of the ReaxFF and QC results. In this case, we constructed ground state geometries through full geometry optimization. In order to obtain dissociation profiles, bond restraint was applied in the atom pair of interest during geometry relaxation. Bond distances were varied from 1.45 to 9Å. ReaxFF nicely reproduces full dissociation profile and in particular, near the equilibrium region it is in excellent agreement with the QC values.

The equation of state calculation was performed on LiF simple cubic crystal to obtain energy-volume relationships. Both compression and expansion with respect to the equilibrium volume were applied on the geometry, and the QC energies were calculated at different volumes. In the fitting procedure, the energies from the ReaxFF and QC optimization of each corresponding volumes are compared. Energy response to the change in volume as predicted by the ReaxFF and QC is shown in Figure 5-1b. We find that the ReaxFF method gives a proper description of the overall energy landscape in comparison with the QC method.

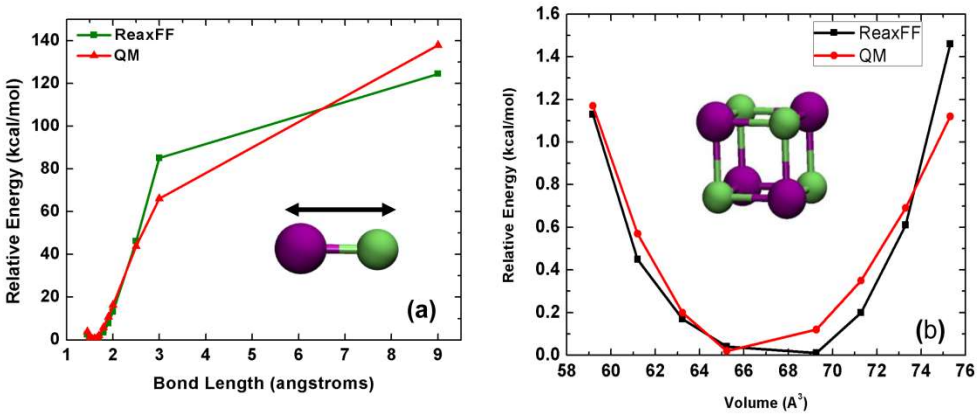

Figure 5-1 Comparison of the ReaxFF and QC data for (a) Li-F bond dissociation in LiF, and (b) LiF simple cubic crystal equation of state. Purple and lime represent lithium and fluorine atoms, respectively

Furthermore, force field parameters were also trained for the Li-binding energies in *N,N* dimethylacetamide (DMA) and *N,N*-dimethyltrifluoroacetamide (DMTFA) electrolytes at their different charged states. Table 5-1 represents the data obtained from the ReaxFF and QC method. In the first case, neutral lithium atom binds with a cluster comprise of four neutral DMA molecules, and in the second case, Li cation binding energy was calculated for the positively charged DMA cluster. Neutral Li binding energy with the neutral cluster of four DMTFA molecules was also calculated. Binding energies are calculated by subtracting individual energies of Li-atom and

electrolyte cluster from the Li-bound electrolyte composition energies. In all these cases, ReaxFF energies are in excellent agreement with the QC data that demonstrates the capability of the ReaxFF method to describe Li-electrolyte interactions.

Table 5-1 Binding energies of Li and electrolyte molecules at their different charged states

System	ΔE_{ReaxFF}(kcal/mol)	ΔE_{QC}(kcal/mol)
Li- 4DMA	-82.412	-79.77
Li^{+}-$4DMA^{+}$	-115.446	-116.36
Li-4DMTFA	-97.23	-95.53

5.3 Simulation Methodology

We utilized our developed ReaxFF reactive force field to set up full lithium-sulfur battery simulations. The Li/SWCNT anode was coupled with the α-sulfur cathode material, and TEGDME was used as the electrolyte. The anode was prepared by adding lithium atoms in (5,5) chirality armchair configuration SWCNT at a ratio close to LiC_6. Nanotube strands were placed facing their open ends toward the electrolytes. To prepare the electrolyte geometry, 54 TEGDME molecules were randomly placed in a large simulation box. An NPT (isothermal, isobaric) simulation was performed to compress the volume of the simulation cell to obtain room temperature density of the electrolyte as well as to get the periodic box dimension so that it matches with the periodic cell dimension. This simulation was carried out at 300K temperature and 100MPa pressure. A Berendsen thermostat and barostat[105] were employed to regulate the temperature and pressure of the system with damping constants of 100fs and 5000fs, respectively, and MD time step was 0.2fs.

For the first set of simulations, we placed Li/SWCNT anode, TEGDME electrolyte and α-sulfur in a simulation cell with periodic boundary condition in two directions (i.e., y and z) and the direction perpendicular to the electrode surface is set as a non-periodic boundary. A fixed graphene

wall is used in the non-periodic dimension parallel to the electrodes to prevent escaping of lithium and other generated species during MD simulations. The wall reflects back the generated species to the simulation cell. The cathode was comprised of α-sulfur with a dimension of (1x3x1 a_o^3). Simulation snapshot is shown in Figure 5-2a.

In the second set of calculations, in order to reduce lithium reactivity, a monolayer consists of short-chain Teflon was utilized as anode surface coating. Total number of atoms in the system with or without Teflon was 3684 and 3484, respectively.

For both systems, the simulation procedure began with the relaxation of the entire system using a low-temperature MD simulation. Next, 300K MD simulations were performed in the NVT (isovolume, isothermal) ensemble using a temperature damping constants of 100fs and an MD time step of 0.20 fs.

5.4 Results and Discussion

5.4.1 Li-SWCNT/TEGDME/Sulfur simulation

During anodic discharge NVT-MD simulations at 300K, lithium atoms release from the SWCNT with a positive charge (>0.5e) and interact with the TEGDME electrolytes. It was observed that release of Li from the SWCNT is a highly exothermic event. The exothermic heat flow causes local heating and increases anode-electrolyte interface temperature substantially. This high temperature enhances reaction kinetics of the lithium interaction with the electrolyte resulting in dissociation of the TEGDME molecules. Major reactive events take place within first few picoseconds of the simulation when electrolyte dissociation generates various species. Once the highly energetic lithium atoms transfer their energy to the neighboring electrolyte molecules, they become less reactive. As the dynamics proceeds, local hot spots dissipate heat to the surrounding regions, and gradually overall system temperature stabilizes to 300K, and no significant reactive

events are observed at 300K equilibrated temperature regimes. Figure 5-2b-d represents temperature distribution in the simulation cell at different time steps. These contour plots are constructed by taking an average of the atomic temperature in 10x10Å grids (in x and y-direction) over 1ps duration. These figures display high-temperature regions at the anode-electrolyte interface during initial stages of lithium discharge from the SWCNT. However, as system equilibration proceeds, local hot spots disappear and temperature distribution at 300ps exhibits more uniform temperature in the simulation cell. It was observed that no noticeable local hot-spots were present after 50ps. Figure 5-2e displays system temperature profile with time during the simulation. We note that the peak temperature in the simulation, averaged over the full simulation box, is ca. 420K because of the fast electrolyte dissociation reactions at about 1ps. This system temperature is comparable with the experimentally measured temperature range of 443-573K due to the violent reactions between lithium and electrolyte in Li-ion batteries.[151]

We investigated the dissociation pathways of a TEGDME molecule upon interaction with the lithium ions. To study these reaction pathways, we randomly placed one TEGDME molecule and six lithium atoms in a simulation cell and run NVT-MD simulation at 300K for 1ps. TEGDME dissociation reactions with Li are exothermic, and reactions occurred very rapidly within about 0.75ps. One of the reaction pathways is shown in Figure 5-3a-e. Dissociation initiated through the cleavage of C-O bond as lithium atom attacks site A and subsequent formation of Li-O bond was observed. Lithium interaction at site B breaks C-O bond to form CH_3OLi. The system interacts with other Li atom, and an energetically favorable pathway induces C-O bond breaking at site C and subsequently releases C_2H_4. Again, Li atom interacts with the Li-O bond at site D produces Li_2O and another C_2H_4 molecule. Figure 5-3f shows the potential energy profile during TEGDME dissociation reactions.

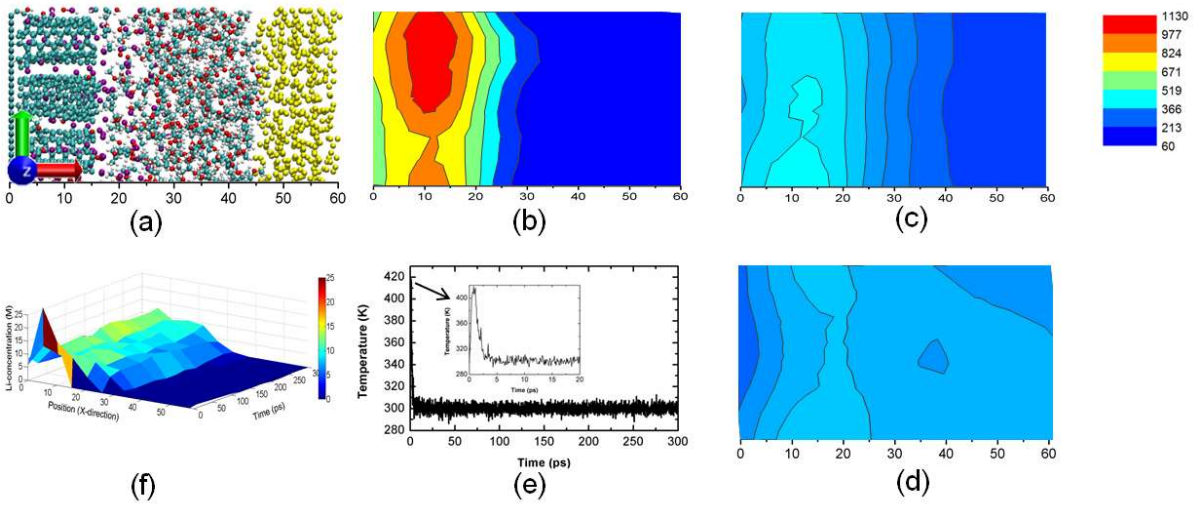

Figure 5-2 (a) simulation snapshot at 10ps; cyan, red, gray, purple represent Carbon, Oxygen, Hydrogen, Lithium atoms, respectively ;Two-dimensional temperature distributions (b), (c), and (d) at 1, 100, and 300ps, respectively. The temperature in the color bar is in K. (e) System temperature profile with simulation time, and (f) Surface plot showing Li-concentration as a function of both cell length and time.

However, the type of reaction products generated in this single-TEGDME simulation is contingent on the number of lithium atoms that are interacting with the TEGDME molecule. Cleavage of two consecutive C-O bonds through lithium interaction releases C_2H_4 gas as a reaction species. CH_3 radical formation was observed through the terminal C-O bond dissociation, however, we did not notice formation of any ethane gas via a combination of two methyl radicals. Rather, CH_3 radical occasionally reacted with the lithium atom and forms $LiCH_3$. Near the anode surface, at high lithium concentration region, TEGDME molecule undergoes multiple lithium-induced C-O bond breaking reactions, resulting in higher number density of trapped ethylene gas. Electrolyte dissociation further from the anode surface, where Li concentration is lower, typically produces higher order alkoxy lithium (R-O-Li). In this simulation, Li_xO (x=2,3,4) was not observed as a stable species rather it survived only about few hundred femtoseconds, and sometimes combined

with the available CH_3 radical to form lithium alkoxide. However, in contrast with the terminal C-O bond, intermediate C-O bond cleavages were detected at a higher frequency resulting in a large number of C_2H_4 formation compared to lithium alkoxides.

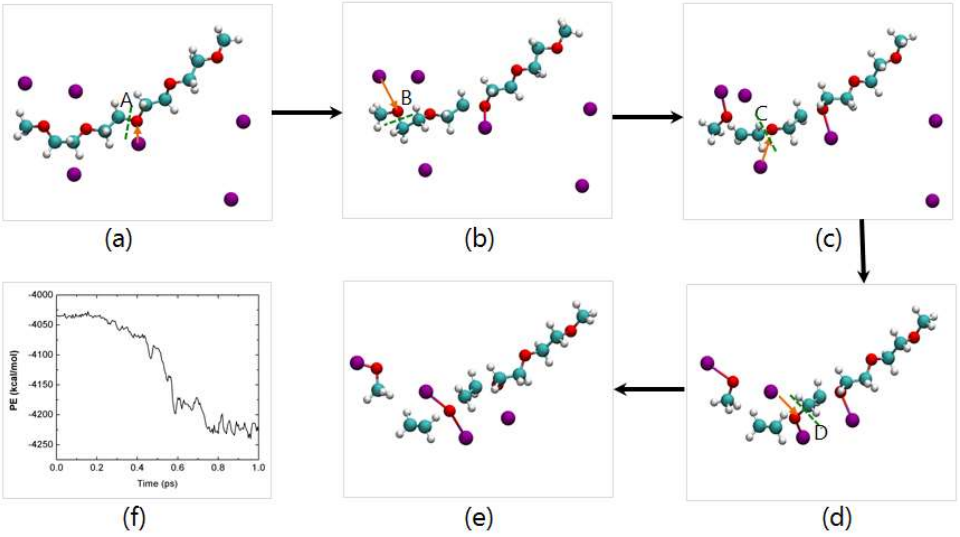

Figure 5-3 TEGDME dissociation pathways; cyan, red, gray, purple represent Carbon, Oxygen, Hydrogen, Lithium atoms, respectively (a) onset of dissociation via cleavage of C-O bond at site A (b) C-O bond breaking at site B and formation of Li-O bond (c) CH_3OLi generates and C-O bond cleavage at site C release of C_2H_4 (d) C-O bond cleavage at site D, (e) Li_2O and another C_2H_4 formation and (f) potential energy profile during dissociation reactions.

Figure 5-4 shows the statistics of the major reaction products, C_2H_4 and TEGDME during the MD simulation. Other species with lower concentration than the major reaction products, and which survived for only a short residence time, were excluded from this analysis. As shown in this figure, TEGDME dissociation and ethylene gas formation reactive events are observed until approximately 50ps. These results are correlated with our previous observation, which shows no significant local heating occurred at about 50ps or subsequent time steps.

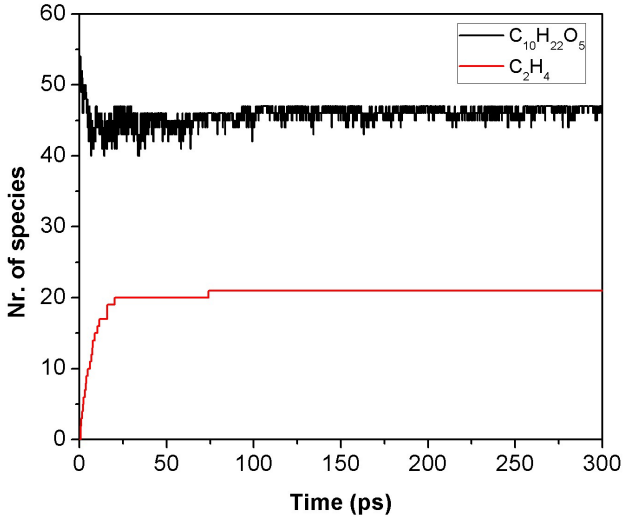

Figure 5-4 Evolution of two major species $C_{10}H_{22}O_5$ and C_2H_4 during 300K NVT-MD simulation (without Teflon)

The lithium ion density in our simulations is higher than the practical lithium-ion density during charging and discharging. In experimental studies, typical Li-ion concentration in the electrolyte is ca. 1-1.2M,[42,49] whereas in our simulation, the interfacial lithium ion concentration was about 10M, which is accountable for de-stabilizing the electrolyte and fast dissociation chemistry. Li-concentration distribution as a function of both cell length and time is shown in Figure 5-2f. In this surface plot, the first peak indicates the lithium concentration in the SWCNT anode at the beginning of the simulation. The spatial variation in the lithium concentration is contingent on the lithium diffusion through the electrolyte, and after the initial release of the lithium atoms from the anode, no significant concentration variation is observed with the time. Our overall observations on electrolyte chemistry are (i) high energetic lithium released from the Li/SWCNT anode causes local heating and thus expedite TEGDME decomposition chemistry, (ii) higher lithium concentration facilitate cleavage of multiple C-O bond leading to the formation of more ethylene gas. However, for the prolonged life cycle of Li-S batteries, it is essential to inhibit electrolyte loss via dissociation. Furthermore, gas formation during battery cycling leads to the

internal pressure build-up and potential safety concerns. To approach this issue, we discuss an *ex-situ* anodic surface treatment approach in the next section.

Table 5-2 Statistics of TEGDME electrolyte dissociation and C_2H_4 formation at 300ps simulation

Simulation	Number of remaining $C_{10}H_{22}O_5$ (out of 54)	Number of generated C_2H_4
Without Teflon	47	21
With Teflon	53	2

5.4.2 Li-SWCNT/Teflon/TEGDME/Sulfur simulation

In the previous section, we discussed high lithium reactivity induced electrolyte destruction. To reduce lithium reactivity, improve electrolyte stability, and concomitantly allowing Li-ion diffusion through the anode-electrolyte interfaces, a porous Teflon coating was used. Teflon is a fluor-carbon polymeric compound with high chemical stability and melting point. A mono-layer of Teflon is chosen for this simulation because multiple layers of Teflon will reduce the lithium diffusivity, and within the given MD time scale, the lithium-electrolyte interaction may not be achievable. In this 300K NVT-MD anodic discharge simulation, highly energetic lithium atoms that are released from the anode by an exothermic process, at first interact with the Teflon coating. Then Li dissipates its energy through transferring heat to the Teflon, and then relatively non-reactive diffusion of lower energy Li occurs through the electrolyte. Teflon effectively withstands high heat flow at the anode-electrolyte interfacial region and reduces subsequent electrolyte decomposition reactions. Figure 5-5a shows the simulation snapshot and 5-5(b-d) displays two-dimensional contour plots for the temperature distribution in the simulation cell. These contour plots were drawn following the same procedure as described in the previous section. Interfacial temperature distribution, in this case is analogous to the non-Teflon case and the system

temperature profile with time as shown in Figure 5-2e and 5-5e has an identical high-temperature peak during the simulation that indicates system undergoes a similar level of exothermic process.

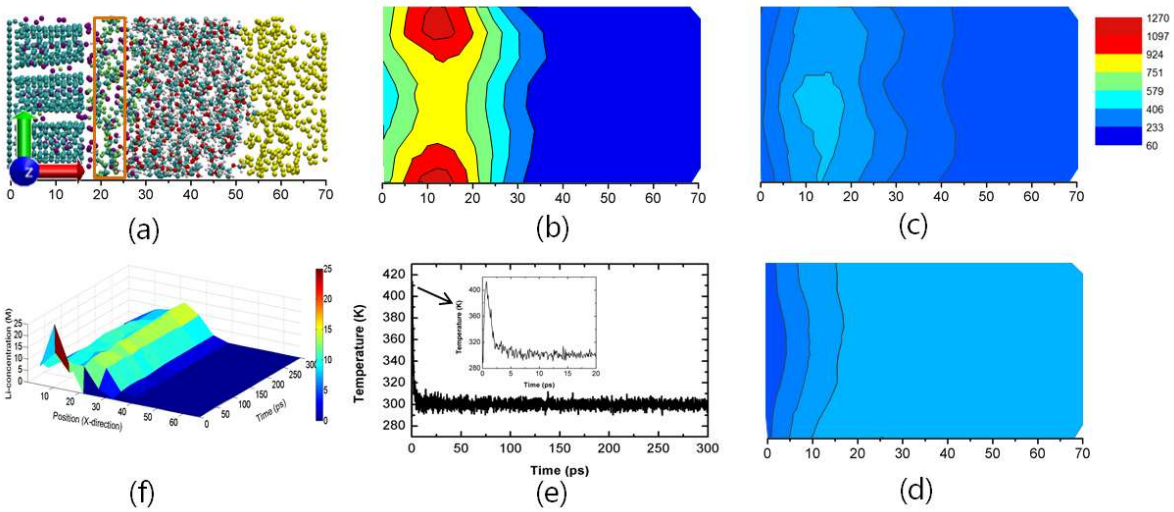

Figure 5-5 (a) simulation snapshot at 10ps; cyan, red, gray, purple represent Carbon, Oxygen, Hydrogen, Lithium atoms, respectively ;Two-dimensional temperature distributions (b), (c), and (d) at 1, 100, and 300ps, respectively. The temperature in the color bar is in K. (e) System temperature profile with simulation time, and (f) Surface plot showing Li-concentration as a function of both cell length and time.

The high-temperature region in the contour plots described in Figure 5-2b and 5-5b for without and with Teflon case, respectively, occurs at the identical spatial region, however, in with-Teflon case this region is occupied by the Teflon coating rather than the electrolyte. Therefore, a lower temperature is observed past the Teflon layer that yields improved electrolyte stability. Distribution of Li-concentration in both spatial direction and time is shown in Figure 5-5f. Usage of Teflon layer demonstrates a notable improvement in electrolyte stabilization, which can be represented by the number of electrolyte molecules dissociated during this simulation. As shown in Table 5-2, a number of dissociated TEGDME and generated C_2H_4 molecules significantly decreases with the usage of Teflon coating. We also studied lithium-Teflon interaction chemistry.

C-F bond energy in isolated Teflon is 128 kcal/mol[152], while in the lithium rich environment, we calculated C-F bond energy as about 30 kcal/mol. Therefore, in the presence of local hotspots, we observed a few C-F bond breaking in Teflon with subsequent formation of LiF. Moreover, perforated Teflon coating can also prevent precipitation of insoluble and insulating polysulfides, such as Li_2S_2, and Li_2S on the anode surface, while maintaining sufficient lithium diffusion through the coating.

5.5 Conclusions

In summary, we performed ReaxFF reactive molecular dynamics simulations to investigate the anode-electrolyte interfacial chemistry of Li/SWCNT anode and TEGDME electrolyte. We developed a ReaxFF interatomic potential through parameterization against a set of QC data for describing electrode-electrolyte interfacial chemistry. In our anodic discharge simulations, lithium ions release from the anode by an exothermic reactive process and their interaction with the electrolyte causes decomposition of a number of electrolyte molecules. We observed that lithium concentration in the electrolyte plays an important role in the reaction products distribution and electrolyte consumption. At high lithium concentration region near the anode surface, ethylene gas is found as a major reaction product. Electrolyte decomposition and subsequent gas formation have a detrimental effect on battery performance. Therefore, to circumvent electrolyte dissociation, we incorporated an *ex-situ* anode surface treatment with porous Teflon coating. Utilization of the Teflon coating dampens high reactivity of the anode discharged lithium ions and thus minimizes electrolyte destruction resulting in improved electrolyte stability.

Finally, the large-scale reactive molecular dynamics (RMD) simulations performed using ReaxFF is a step towards the fundamental understanding of the electrode-electrolyte interfacial chemistry at the atomic or molecular level. RMD simulations can assist to complement the analysis of experimental results on the interfacial phenomenon and to explore SEI formation mechanism

using a mixture of different electrolyte solvents and additives for developing high-performance Li-S batteries.

Chapter 6

ReaxFF Molecular Dynamics Simulations on Lithiated-Sulfur Cathode Materials

Part of this chapter also published in ref,[87] authored by Md Mahbubul Islam, Alireza Ostadhossein, Oleg Borodin, A Todd Yeates, William W Tipton, Richard G Hennig, Nitin Kumar, and Adri CT van Duin. Md Mahbubul Islam performed the ReaxFF and part of the DFT simulations, analyzed results and wrote the paper.

6.1 Introduction

Over the last two decades, lithium-ion batteries (LIBs) have become ubiquitous in portable consumer electronics. However, the limited capacities of LIBs impede their application in electric vehicles (EVs) and smart-grids.[7,127] Automotive applications require significant improvements in the capacity of electrode materials to allow long trips (i.e. >300km) in a single charging. [153,154] Sulfur based cathode materials for Li-S batteries are considered a very promising alternative to the conventional transition metal oxide/phosphate cathodes[3] due to their high capacity, energy density, non-toxicity, and natural abundance[42]. The theoretical specific capacity of sulfur is 1672 $mAhg^{-1}$, which is 10 times higher than that of commonly-used $LiCoO_2$ cathodes, and it has a theoretical specific energy density of 2600 $Whkg^{-1}$, assuming complete reaction to Li_2S.[42,43,153]

In current battery technologies, the capacity of the cathodes is substantially lower than that of commercially available anode materials, such as graphite. Moreover, high capacity Si and Sn-based anodes are being developed.[155–159] These materials have theoretical specific capacities of 4200 $mAhg^{-1}$ and 900 $mAhg^{-1}$, respectively.[160] However, any breakthrough in the capacity of the anode materials must be accompanied by improvements to the cathode to develop high-performance batteries to meet next generation energy demand.

Although sulfur exhibits great promise, commercialization of Li-S batteries has been thwarted by several complex problems, such as significant structural and volume changes of the cathode, the high reactivity of lithium, dissolution of intermediate polysulfides into the electrolytes, poor electronic and ionic conductivities of sulfur and Li_2S, and safety concerns.[52,161–164] Volume expansion of the sulfur composite cathode occurs during discharging (lithium intercalation) and contraction during charging (lithium de-intercalation).[165] This active material breathing induces stress in the cathode material, and the active material loses its electrical contact with the conductive substrate or with the current collector.[135] Numerous approaches have been reported in the literature to accommodate volume changes, including sulfur-coated multi-walled carbon nanotubes composite material,[166,167] graphene wrapped sulfur particles,[138] and reduced graphene oxide encapsulated sulfur.[168] These approaches demonstrate high initial capacity, but rapid capacity fading due to cathode degradation still greatly limits performance.

Furthermore, a great deal of recent studies of Li-S batteries used elemental lithium as anode material.[49,52,125,135,169] The lithium anode yields high capacity, but it has low cycling efficiency and forms lithium dendrites on the anode surface during cycling that can penetrate the separator leading to short circuit.[47,125] To inhibit dendrite formation, Li-ion conducting passivation layers using Li_3N,[128] Li_2CO_3,[129] and LiPON,[130] have been suggested. These thin protective films suppress lithium dendrite formation, but a high cost of fabrication has limited their use.[132] Lithium dendrite formation issues have not yet been fully resolved, restricting the use of Li-metal anodes in commercial batteries.[170] Recently, lithium-metal free batteries that use silicon or tin instead of elemental lithium in the anode have received much attention due to improved safety properties.[171] In these systems, neither the sulfur cathode nor the Si or Sn anode contains lithium originally, so either the cathode or the anode must be prelithiated to provide a lithium source. To this end, systems composed of Li_2S cathodes and Si anodes have been studied by several previous authors.[162,172,173] However, relatively low lithium diffusivity and high electronic resistivity cause a large potential

barrier to activate the Li_2S cathode.[172] He and coworkers[174] investigated a prelithiated sulfur composite/graphite lithium-ion cell, which was fabricated using electrochemical lithiation. Li-ion diffusivity in lithiated sulfur depends on the lithium concentration, and lithiated cathode materials possess lower specific capacity than their non-lithiated counterparts.[175]

While significant progress towards improving the performance of the Li-S battery has been achieved[163], there is a lack of understanding of mechanical and structural properties of the lithiated sulfur compounds. Molecular dynamics (MD) simulations are well suited for examination of the a-Li_xS as a function of lithiation provided an accurate representation of the intermolecular interactions, and chemical reactions are achieved. Such simulations are expected to provide a fundamental understanding of the material properties such as understanding the morphological changes a-Li_xS undergoes, and the mechanical degradation of this electrode material at the atomistic level. To the best of our knowledge, no MD simulations have been performed on a-Li_xS systems, probably due to lack of an accurate intermolecular potential. Previously[92], we reported electrolyte chemistry and an *ex-situ* anode surface treatment process for Li-S batteries. In this study, we describe the development of a Li-S ReaxFF potential to model Li-S interactions and use it to investigate the structural evolution, mechanical properties, and diffusion characteristics of a-Li_xS systems.

6.2 Force Field Development

Development of our ReaxFF force field for the Li-S system was initiated by merging previously published lithium[94] and sulfur[143] parameters. In the fitting procedure, these parameters were extensively trained against quantum mechanics (QM) data describing bond dissociation, angle distortion, equation of state, and heats of formation of crystalline phases and molecules. The optimization of the parameters was performed via a successive one-parameter search technique[100] to minimize the sum of the following error:

$$Error = \sum_{i}^{n} \left[\frac{(x_{i,QM} - x_{i,ReaxFF)}}{\sigma_i} \right]^2$$

where x_{QM} is the QM value, x_{ReaxFF} is the ReaxFF calculated value, and σ_i is the weight assigned to a data point, i.

Non-periodic QM calculations used in this study were performed in the GAMESS[176] program using second-order Møller–Plesset (MP2)[177] method in conjunction with aug-cc-pVTZ basis set.

To parameterize the ReaxFF bond energy data, we carried out QM calculations for the Li-S and S-S bond dissociation in various molecules, such as Li_2S_2, and LiSH. Figure 6-1a-c compares ReaxFF and QM results for the bond dissociation. In each case, we constructed ground state geometries through full geometry optimization. In order to obtain dissociation profiles, bond restraint was applied in the atom pair of interest while rest of the structure was allowed to relax during minimization. Bond distances between Li and S were varied from 1.5Å to 6.0 Å. The equilibrium bond lengths predicted by the QM and ReaxFF are 2.04 and 2.2Å, respectively. The ReaxFF calculated Li-S equilibrium bond length is closer to the Boldyrev et al.[178] reported the value of 2.15Å. It can be seen that in the QM energy profile the lowest energy state switches from singlet to triplet at Li-S bond stretching beyond 3.5A, and ReaxFF nicely captures this phenomenon by reproducing the lowest energy states. In the S-S bond dissociation, energy profile of Li_2S_2, the QM energy for the singlet manifold is the Spin Component Scaled (SCS) MP2, which is claimed to be more accurate for bond breaking. Likewise, the Li-S bond energy profile, in S-S bond stretching, ReaxFF predicts the ground state that corresponds to the singlet state of the QM energy landscape. ReaxFF calculated S-S bond length in D_{4d} cyclic S_8 is 2.17A, which is consistent with the value of 2.08A from the gas phase cluster calculations by Wong et al.[179] The ReaxFF dissociation energy for both Li-S and S-S bonds are within 5 kcal/mol of the QM results. Good agreement between ReaxFF and QM are also achieved for Li-S bond dissociation in the LiSH molecule.

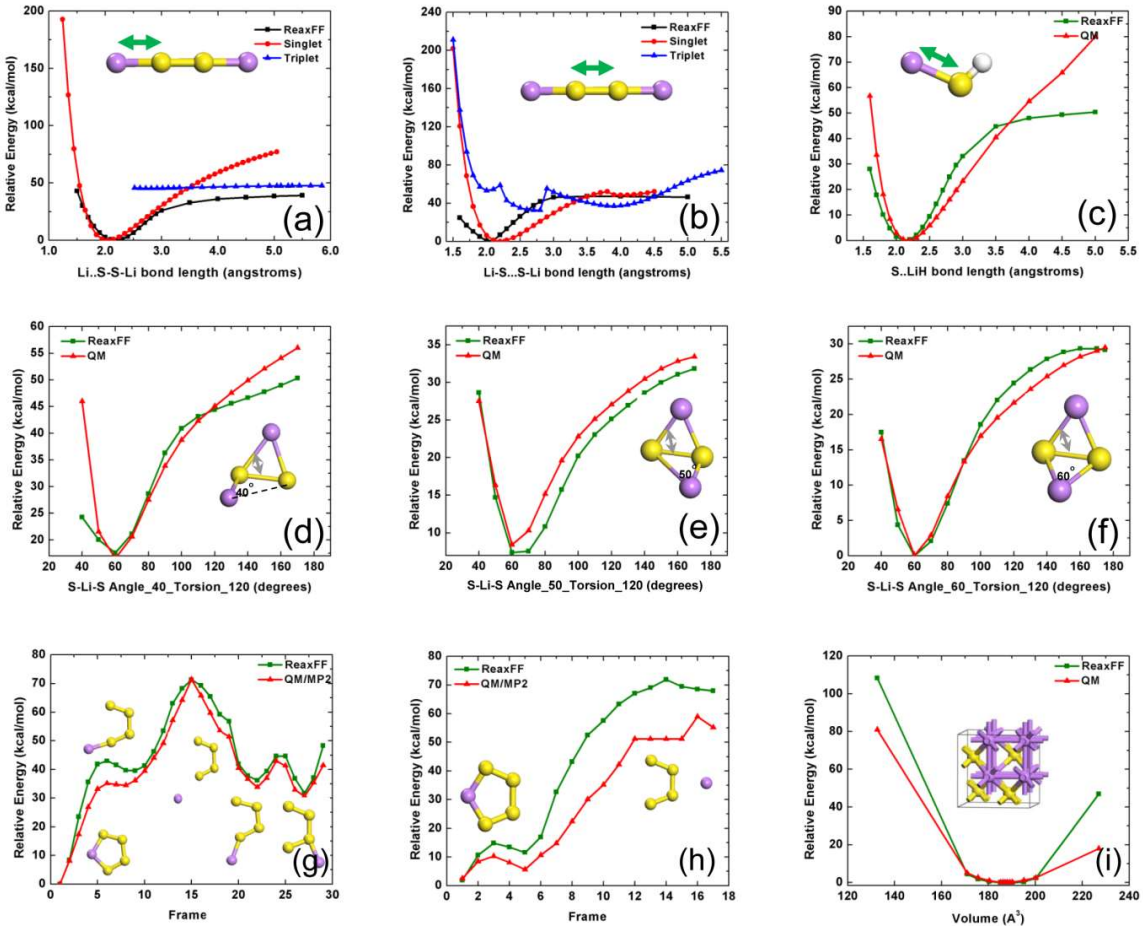

Figure 6-1 QM and ReaxFF data: bond dissociation curves for (a) Li-S bond in Li_2S_2, (b) S-S bond in Li_2S_2, (c) S-Li bond in LiSH, S-Li-S valence angle distortion in Li_2S_2 keeping S-Li-S angle at (d) 40º (e) 60º (f) 80º (g) for the migration of a Li-cation around an S_4-anion (h) for the dissociation of a Li-cation from an S_4-anion, and (i) Equation of state for Li_2S crystal structure**.** Yellow and purple represent sulfur and lithium atom, respectively. QM=MP2/aug-cc-pVTZ for (a-h) and GGA/PBE for (i)

In order to optimize S-Li-S and S-S-Li valence angle parameters, we performed QM calculations for these valence angles on the Li_2S_2 molecule at a fixed torsion angle. In each case, we kept the S-Li-S angle fixed at a value, while the S-S-Li angle was varied from 40º to 170º to get

the energy response for the angle bending. For fitting, we calculated ReaxFF energies of each of the valence angle configurations. These are shown along with corresponding QM energies in Figures 6-1d-f, and we see that ReaxFF correctly reproduces QM equilibrium angles and the overall energy profile.

An equation of state calculation was performed on crystalline Li_2S (space group no. 225). We carried out periodic QM calculation based on density-functional theory (DFT).[180,181] The Vienna *ab initio* simulation package (VASP) was used to solve the Kohn-Sham equations with periodic boundary conditions and a plane-wave basis set.[182,183] We employed Blöchl's all-electron frozen core projector augmented wave (PAW) method[184] and electron exchange and correlation is treated within the generalized gradient approximation (GGA) of PBE.[149] The energy cutoff on the wave function is taken as 600 eV and the Monkhorst-Pack scheme was used for the k-point sampling with 5x5x5 k-point grid. We applied compression and expansion with respect to the equilibrium volume of the crystal to calculate QM energies at different volume state. Next, during force field optimization, energies calculated from the ReaxFF corresponding to each volume are compared with the QM data. Figure 6-1i shows the EOS of the Li_2S crystal as predicted by ReaxFF and QM. We see that ReaxFF acceptably reproduces the QM results near the equilibrium. ReaxFF predicts the lattice constant of Li_2S crystal as 5.75A, which is within 0.5% of the reported experimental value of 5.72A.[185]

Furthermore, we trained our force field for a Li cation migration around and dissociation from an S_4 anion. The geometry of S_4^{2-} was fixed. ReaxFF parameters were fitted against the MP2/aug-cc-pVTZ level of QM results, and the data in Figure 6-1g and Figure 6-1h were obtained. We see a good agreement of the ReaxFF, and QM results for the Li-migration pathway (Figure 6-1g) and ReaxFF reasonably reproduces QM energetics for Li-dissociation (Figure 6-1h).

Heats of formation (HF) of various crystalline and gas phase lithium-sulfur species were also utilized in force field fitting. Heats of formation of Li_xS species were calculated with respect to S_8 molecule, and bcc-Li were calculated using the following relation

$$\Delta E = E_{Li_xS} - xE_{Li} - E_S$$

where E_{LixS} is the total energy of the Li-S system, x is the atomic fraction of lithium, and E_{Li} and E_S are the energies per atom of bcc-Li and sulfur, respectively. Data obtained from the ReaxFF and QM methods are presented in Table 6-1. The results in Table 6-1 indicate that ReaxFF reasonably reproduces the HF of the Li_xS species studied.

Table 6-1 Heats of formation of different Li_xS crystals and molecules as calculated from the ReaxFF and QM (MP2/aug-cc-pVTZ)

Species	ReaxFF(eV)	QM (eV))
Li_2S crystal	-3.88	-4.47
LiS crystal	-1.96	-1.89
LiS_6	-0.79	-0.75
LiS_7	-0.05	-0.67
LiS_8	-0.18	-0.74
LiS	0.95	1.37
LiS_3	-0.74	-0.65
Li_2S	-0.22	-0.59

Reaction energies of various polysulfides, Li_xS_y were calculated and ReaxFF energies are compared with the QM results reported by Assary et al.[186] and represented in Table 6-2. QM calculations were performed using coupled cluster based highly accurate G4MP2[187] with B3LYP/6-31G(2df,p) level of theory. ReaxFF qualitatively reproduces the QM reaction energies of the major polysulfides involved in Li-S battery operation. However, some of the values, e.g. reaction 3 in the

Table 6-2 differ from the corresponding QM data. These reaction pathways were not contained in the training set, and as such there are some deviations between ReaxFF and DFT, however, ReaxFF reproduces the trends in these gas phase reaction energies, which is important to describe the condensed phase simulations considered in this study. In these calculations, Li_2 and cyclic S_8 were used as a reference value.

Table 6-2 Comparison of the reaction energies of various polysulfides as calculated using ReaxFF and G4MP2 level of theory[186]

Reactions	ΔE(eV):ReaxFF	ΔE(eV):QM[186]
$S_8+2Li \rightarrow Li_2S_8$	-5.61	-6.02
$Li_2S_8 \rightarrow Li_2S_5+S_3$	1.51	1.11
$Li_2S_8 \rightarrow Li_2S_4+(1/2)S_8$	0.59	0.18
$Li_2S_4 \rightarrow Li_2S_2+(1/4)S_8$	1.03	1.14
$2Li_2S_4 \rightarrow 2Li_2S_3+(1/4)S_8$	1.35	0.96
$2Li_2S_3 \rightarrow 2Li_2S_2+(1/4)S_8$	0.72	1.32
$2Li_2S_2 \rightarrow 2Li_2S+(1/4)S_8$	3.61	2.10
$Li_2S_8 \rightarrow LiS_6+LiS_2$	1.81	2.36

Overall, ReaxFF energy descriptions are in good agreement with the QM data, which establishes the capability of the force field to describe the chemistry of lithium-sulfur interactions.

6.3 Simulation Methodology

We employed our Li-S force field to study various lithiated sulfur configurations, Li_xS (x = 0.4, 0.8, 1, 1.2, 1.6, 2.0). Initial geometries were constructed by randomly dispersing lithium atoms at the given ratios in an α-sulfur phase comprised of 2048 atoms. Lithiated sulfur geometries were relaxed using a conjugate gradient minimization scheme. We created amorphous structures by slowly heating the initial structures to 1600K and then rapidly quenching them to 300K.

Temperature and pressure were regulated using the Berendsen thermostat and barostat[105], respectively. To obtain the room temperature densities of these annealed structures, NPT (constant pressure, temperature) simulations were performed at 300K and atmospheric pressure. The temperature and pressure damping constants used in both annealing and the NPT simulations were 100fs and 2500fs, respectively. Next, final structures from the 300K NPT simulations were taken from each of the given configurations, and NVT (constant volume, temperature) simulations were performed at various temperatures (i.e. 300K, 600K, 800K, 1000K, 1200K, and 1600K). Temperature and pressure damping constants were 500 and 5000 fs, respectively, and the simulation duration was about 1 ns. High temperature NVT simulations facilitate diffusion coefficient calculations. In order to evaluate mechanical properties of the lithiated sulfur compositions, deformation simulations were carried out using the NPT ensemble in LAMMPS[188] at 300K and atmospheric pressure. The Nosé-Hoover thermostat and barostat[189] were used with temperature and pressure damping constants of 50fs and 1000fs, respectively. Periodic boundary conditions were employed in all three directions, and a MD time step of 0.25 fs was used for all the simulations in this study.

6.4 Force Field Validation

6.4.1 Phase Diagram

To verify the quality of our Li-S potential in describing the various Li_xS phases, the Genetic Algorithm for Structure and Phase Prediction (GASP)[190,191] was employed. We used it to investigate the energy landscape of our potential, to identify low-energy configurations, and thus to construct the Li-S binary phase diagram, according to the potential. A GA is a heuristic optimization algorithm modeled after the biological process of evolution, and its purpose here is to find the lowest-energy configurations at every composition between pure Li and pure S. The algorithm uses the information learned from the early guesses and makes better guesses to produce improved

structures later on. The initial structures, known as parent generation, are generated randomly within some hard constraints: maximum and minimum lattice parameters and number of atoms, interatomic distances, and number of species. New structures are evaluated by their formation energies with respect to the currently-known ground state phases. The lower this metric, the more likely a structure is to be chosen as a parent and used to generate offspring by means of mutation and mating operations. The algorithm proceeds by producing successive generations, and as it does, low energy structural motifs are likely to survive, while structures with high energy become less common.

The algorithm was run for 50 generations with 50 structures per generation, and the resulting Li-S phase diagram is shown in Figure 6-2. This diagram is constructed by plotting each structure encountered by the algorithm according to its formation energies with respect to the elements versus its composition. The lower convex bound on the points is known as convex hull and is used to determine the thermodynamic ground states and energies of the various Li-S compositions. The structures which lie on the convex hull are ground states at their composition. At compositions which have no representative on the curve, the lowest-energy configuration is actually a mixture of materials at other compositions.

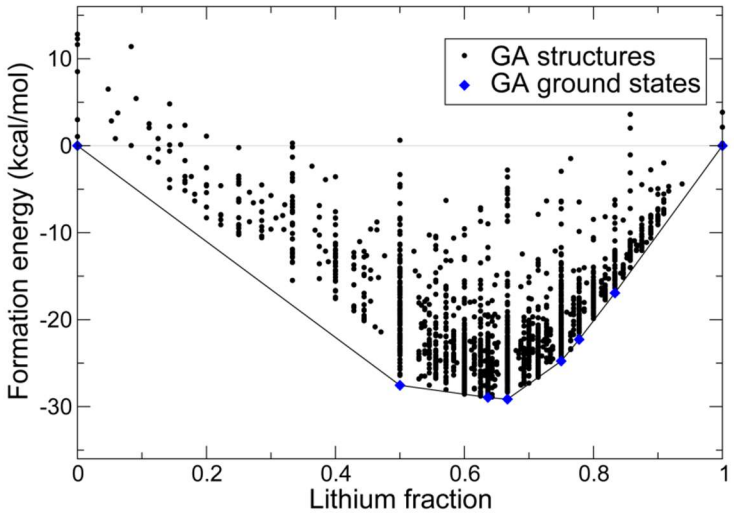

Figure 6-2 Convex hull phase diagram of Li_xS compositions.

For any structure, the vertical distance between its point and the convex hull is the energy difference between this phase and corresponding thermodynamic ground state. In the phase diagram, we identify stable binary structures with compositions LiS, Li_7S_4, Li_2S, Li_3S, Li_7S_2, and Li_5S, although all but LiS are barely stable with respect to Li_2S and the elements and are artifacts of the fitting procedure. The experimentally known binary phase, with composition Li_2S, is not the ground state according to the potential but lies only 0.24 kcal/mol above the convex hull.

6.4.2 Discharge Voltage Profile

We used the hybrid grand canonical Monte Carlo/molecular dynamics (GC-MC/MD) method described by Senftle et al.[192,193] to investigate lithium insertion into α-sulfur. We calculated heats of formation of lithiated sulfur compounds and found the corresponding open circuit voltage profile. A $TP_{\mu Li}N_S$ ensemble (constant pressure and adjustable volume) was used so that the structure could change its volume upon lithiation. The acceptance criterion used for lithium insertion into α-sulfur in this simulation is analogous to that described in Ref. [192]. Each MC trial

move was followed by a low-temperature MD-based energy minimization to allow structural relaxation. This increases the MC acceptance rate by placing Li atoms into low energy sites.

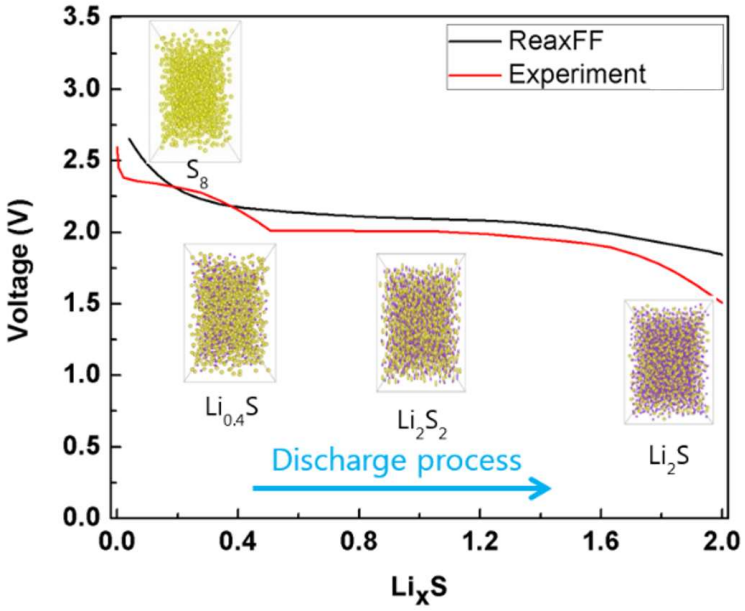

Figure 6-3 Open circuit voltage profile during lithiation of the sulfur cathode. Experimental data is from the ref.[123]. Yellow and purple represent sulfur and lithium atom respectively.

Heats of formation of the lithiated sulfur configurations as a function of lithium content with respect to α-sulfur and bcc-Li were calculated using the relation mentioned in the force field development section. Next, we calculated the open circuit voltage profile during lithiation as a function of lithium concentration. The voltage profile relative to Li/Li^+ is given by

$$V(x) = -\frac{G_{Li_xS} - xG_{Li} - G_S}{x}$$

where, G is the Gibbs free energy and x refers to the lithium concentration. Approximating enthalpic (PV) and entropic (TS) contributions are negligible; Gibbs free energy can be replaced by the ground state energy.

Discharge voltage profile corresponding to the reduction pathway of S_8 to Li_2S was calculated and is shown in Figure 6-3. The derived voltage profile is consistent with the results reported in Ref. [**42,123**] Likewise, the experimental observation, ReaxFF calculations nicely predict the initial drop in the voltage profile due to the formation of high molecular weight polysulfides and the flatter region and subsequent drop in the voltage approaching Li_2S.

6.4.3 Volume Expansion of Li_xS Compounds

The sulfur cathode undergoes significant volumetric expansion upon Li uptake. In this study, the volumes of a-Li_xS at various compositions were obtained from NPT simulations at 300 K and atmospheric pressure. The relative volume is plotted against lithium concentration in sulfur phase as shown in Figure 6-4.

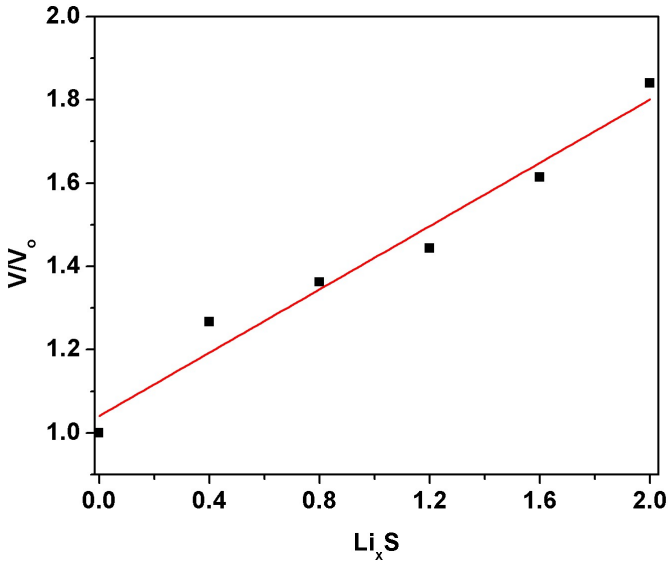

Figure 6-4 Volume expansion as a function of lithiation. V is the volume of the lithiated configurations and V_o is the volume of unlithiated sulfur.

The volume of Li-S amorphous phases increases almost linearly with x. In the case of Li_2S, ReaxFF predicts a volume expansion of 83%, which is in excellent agreement with the reported experimental prediction of 80%.[52,168,194]

6.5 Results and Discussions

6.5.1 Structural Properties

To evaluate the structural properties of lithiated sulfur compounds, we calculate radial distribution functions (RDF), g(r), and the number of atoms within first coordination shell using following formulae

$$g(r) = \frac{n(r)}{\rho\ 4\pi r^2 \Delta r} \qquad CN = \int_0^{r'} \rho . 4\pi\, r^2 . g(r)\, dr$$

where n(r) is the number of atoms within a distance r of a central atom, ρ is the bulk number density, r' is the distance to the first minima of g(r) from each atom, and CN is the coordination number. The RDFs are obtained by extracting trajectories at 0.125 pico second intervals from the 300K NVT simulations. S-S, Li-Li, and Li-S RDFs for all the a-Li_xS cases considered in this study are presented in Figure 6-5a-c.

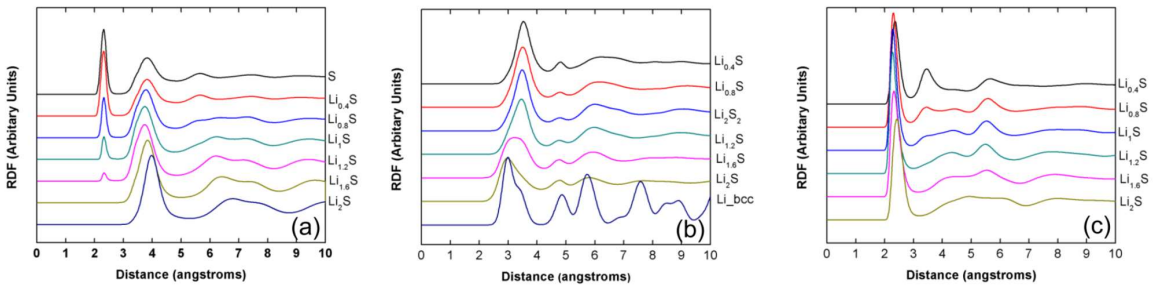

Figure 6-5 Radial distribution functions (a) S-S (b) Li-Li, and (c) S-Li atom pairs

In these RDFs, we observe peaks that are much broader than for typical crystalline materials. Along with the absence of sharp peaks at long-range, this suggests structural amorphization. In Figure 6-5a, with the increasing lithium content, the S-S first peak decreases, and the second peak increases. The first peak is attributed to the S-S covalent bond, while the second one around 4.0 Å corresponds to sulfur being bound through Li^+. Note that position of the

second peak is slightly lower than double of the Li-S first peak. During lithiation the fraction of polysulfides (Li_mS_n, $n\geq2$) decreases and fraction of Li_xS increases as indicated by the diminishing magnitude of the first peak of S-S RDF. At a high lithium content, sulfur is increasingly held together via lithium linkages as indicated by the increasing second peak located around 4.0 Å. Similarly, the Li-Li RDFs in Figure 6-5b show that at higher lithium concentrations, Li-Li interactions become stronger as bond lengths contract from 3.5Å to 3.0Å due to the formation of more Li^+-Li^+ bonding in Li_xS. The Li-Li RDFs for our model amorphous phases are also compared with the crystalline bcc-Li. The crystal's RDF indicates long-range order, and the calculated Li-Li bond length is also in conformity with reported value of 3.03Å.[195] In all the lithiated sulfur compounds, the nearest neighbor peak of Li-S atom pairs remain close to 2.2Å to 2.3Å as shown in Figure 6-5c.

6.5.2 Mechanical Properties

To characterize the mechanical behavior of the a-Li_xS compounds, we performed room temperature MD simulations and obtained the stress-strain relationship under uniaxial tensile loading. We considered five different uniaxial strain rates ($1x10^8$, $5x10^8$,$1x10^9$, $1x10^{10}$, $1x10^{11}$ s^{-1}) to investigate the effect of strain rate on the mechanical properties. Stresses are calculated based on the definition of virial stress, which is expressed as

$$\sigma_{virial}(r) = \frac{1}{\Omega}\sum_i \left[(-m_i\dot{u}_i \otimes \dot{u}_i + \frac{1}{2}\sum_{j\neq i} r_{ij} \otimes f_{ij})\right]$$

where the summation is over all the atoms occupying the total volume, m_i is the mass of atom i, is the time derivative which indicates the displacement of atom with respect to a reference position, , where is the position vector of atom , is the cross product, and is the interatomic force applied on atom i by atom j.

Figure 6-6a-c shows tensile stress-strain curves at three strain rates for all the lithiated sulfur cases considered in this work. At lower strain rates, past the elastic limit, stress rises and drops repeatedly with the strain, while under faster loading, no such fluctuations are observed. Similar trends in the stress-strain curve at other strain rates have been observed in amorphous Ni-nanowire deformation simulations.[196] The zigzag stress-strain curve after the elastic limit at lower strain rate and higher lithiation cases are due to the stress-relaxation during tensile loading. At a strain rate of 10^{11} s^{-1}, the maximum stress occurs at ~15% strain. However, at a lower strain rate, it shifts to ~10% strain. In general, stress-strain curves exhibit an initial linear region followed by a nonlinear portion and then a drop in stress. The linear portion of the uniaxial stress-strain curve corresponds to elastic deformation, and the gradient of this part is Young's modulus (YM). In this study, YM was calculated using linear regression on the initial linear portion. The yield strength was computed by plotting a line parallel to the linear part of the stress-strain curve at 0.2 percent strain offset. The intersection between this 0.2 percent offset line and stress-strain curve gives the yield strength. The ultimate strength is the maximum stress experienced during tensile loading. Effect of strain-rate on various mechanical properties and the lithiation-induced variation in strength for the a-Li_xS cases are presented in Figure 6-6d-f. We see that the strain-rate has significant consequences for all of the material properties. During tensile loading, the combination of both elastic and anelastic (time-dependent, fully reversible deformation) strains determine the mechanical behavior of the materials.

At higher loading rates, anelastic strain approaches zero resulting in entirely elastic strain, while at low-strain-rates both of them accompany the loading process that contributes to the lower strength.[197] Moreover, increases in strain rate enhance the flow stress that directly influences the mechanical behavior. The calculated Young's modulus, ultimate strength, and yield strength at low-strain-rate are lower than that at high-strain-rates. This trend is consistent with the experimental observations for amorphous materials.[198] It can be seen from Figure 6-6d-f that strain

rate converges at $1x10^{10}$ s^{-1} and the reported strength and YM values are in close proximity for the strain rate of $1x10^{10}(s^{-1})$ and lower. The calculated YM value for Li_2S is ~45GPa, which is lower than the previously reported[199] DFT-GGA results of 76.6 GPa, the discrepancy is likely due to the absence of thermal effects in DFT optimization. However, extrapolation of the Young modulus of the dense hot pressed Li_2S-P_2S_5 pellets to 100% Li_2S composition would yield values around 35GPa, which is in excellent agreement with the ReaxFF predictions.[200]

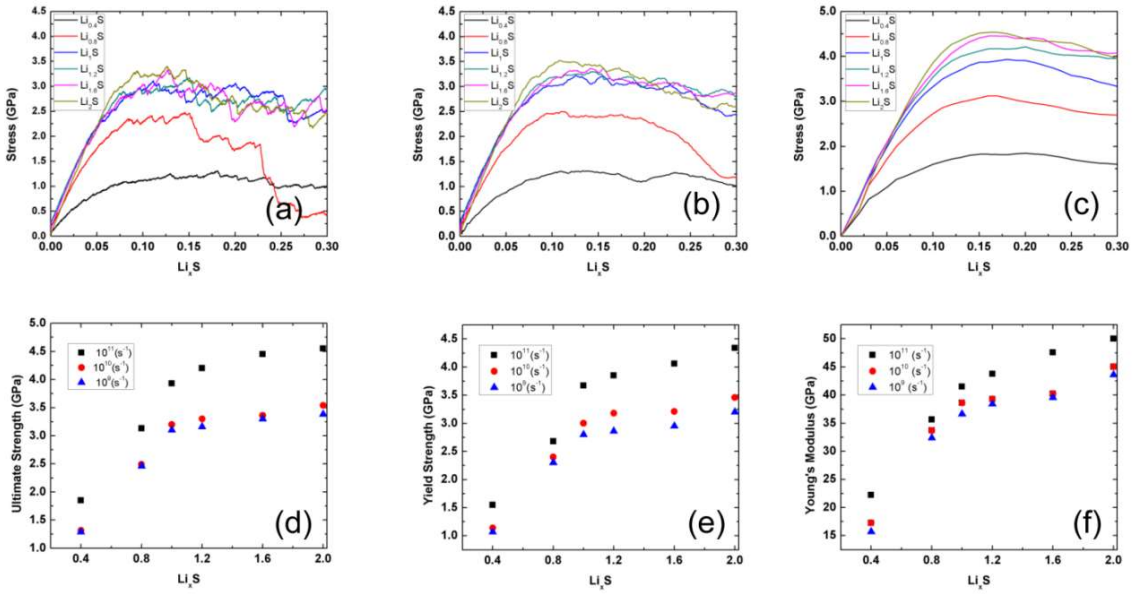

Figure 6-6 Stress-strain curve for the a-Li_xS compositions at different strain rate (a) 10^9 s^{-1} (b) 10^{10} s^{-1}, and (c) 10^{11} s^{-1}; other mechanical properties (d) Ultimate strength (e) Yield strength, and (f) Young's modulus

It is evident that lithiated sulfur compounds undergo strain hardening with increasing lithium concentration. Lithiation also augments toughness and ductility of the lithiated compounds. Toughness is the amount of energy absorbed by a material before its failure. We observe that improvement in material strength is rapid during initial lithiation, but beyond $Li_{1.2}S$ strengthening is not substantial. During initial lithium loading, Li-S bonds are formed through the cleavage of S-S bonds. This contributes to the increase in strength, while at higher lithium content, Li-Li bond

formation contributes to the strength increment to a lesser extent. Interestingly, the lithiation induced mechanical response of the a-Li_xS compounds is quite opposite of that observed for the a-Li_xSi alloys. Lithiation degrades the mechanical properties of silicon,[157,201] while in the case of sulfur; it enhances the strength of the material. Lithiation of Si causes breaking of Si-Si bonds and subsequent formation of the Li-Si bonds. The softening effect due to the lithium insertion into the Si is attributed to the decrease in the number of strong covalent Si-Si bonds as they breaks and replaced by the weaker ionic Li-Si bonds. Shenoy et al.[202] reported the elastic moduli of the amorphous-Si and Li are 92 and 20 GPa, respectively. Our ReaxFF calculations predict the elastic moduli of Li and S as 23 and 5.78 GPa, respectively. Therefore, insertion of the Li into the softer S resulting in the increase of the strength of Li_xS compositions.

In addition, we studied the failure behavior of lithiated sulfur compositions during tensile loading. Fracture initiates via the formation of small voids in the structure, followed by the coalescence of multiple voids that leads to necking. As the tensile loading continues, stress concentration at the necking region is eventually leading to rupture. This failure mode is commonly observed in amorphous materials. An example of failure behavior for $Li_{0.8}S$ is shown in Figure 6-7.

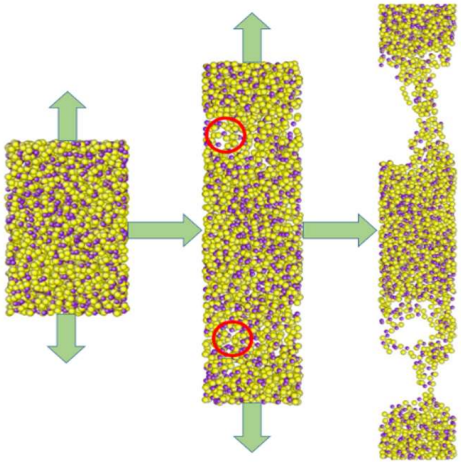

Figure 6-7 Failure behavior of $Li_{0.8}S$ composition upon tensile loading. Fracture initiates via formation of voids. Yellow and purple represent sulfur and lithium atom, respectively.

6.5.3 Diffusion Coefficients

For the analysis of the diffusion of lithium and sulfur in a-Li_xS, we carried out NVT MD simulations at several temperatures. We stored unfolded trajectories generated from the NVT MD simulations at every 0.125 ps and calculated the mean-square displacement (MSD) as a function of the position of each diffusing particle. MSDs and diffusion coefficients (DCs) were calculated using Einstein's relation

$$MSD = < |r(t) - r(0)|^2 >$$

$$D = \frac{1}{6} \lim_{\Delta t \to \infty} \frac{MSD(t + \Delta t) - MSD(t)}{\Delta t}$$

where r is the position of the particle, t is the time, and D is the diffusion coefficient.

Because of the slow rate of diffusion of both species in the Li_xS compositions, it was challenging to calculate DCs at 300K given our MD time scale. Therefore, we calculated DC at elevated temperatures using the above equations. To facilitate DC calculation at room temperature, we extrapolated our elevated temperature data through the following Arrhenius equation[203]

$$D(T) = D_o \exp(-\frac{E_a}{kT})$$

where D_0 is the pre-exponential factor, E_a is the activation energy, k is the Boltzmann constant, and T is the temperature. The activation energy and pre-exponential factors are independent of temperature and were computed using an exponential regression analysis of a D vs. 1/T plot.

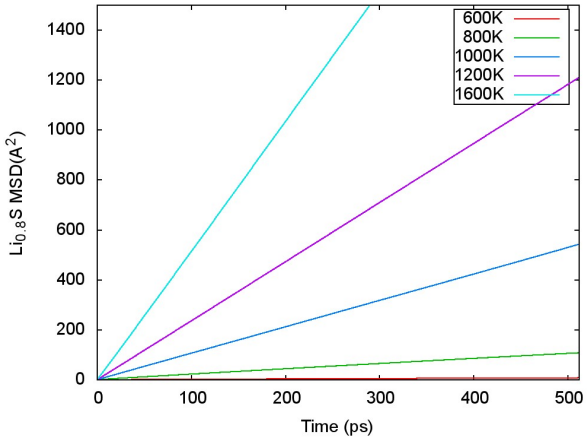

Figure 6-8 MSD of lithium atoms in the $Li_{0.8}S$ simulation at different temperatures

Figure 6-8 represent MSD vs. time plot for Li at various temperatures for the representative case of $Li_{0.8}S$. Figure 6-9 shows the relationship between diffusivity and temperature through the Arrhenius equation for the sulfur and lithium in the Li_2S case. Using the Arrhenius plot, we calculated 300K diffusion coefficients for both Li and S via extrapolation of our high-temperature data. This is presented in Figure 6-10. It is evident that diffusivity of both species depends strongly on the lithium concentration. Interestingly, lithium and sulfur DCs decrease initially with the lithiation, but this trend soon reverses. We observe that DCs of both species are of the same order of magnitude up to $Li_{1.2}S$.

However, further lithiation increases Li diffusivity to two orders of magnitude higher than that of S, which indicates that at higher lithium concentration, Li is the dominating diffusion species. The difference in DC between these two species at higher lithium concentration may be responsible for stress generation where lithium atoms have to push sulfur in order to diffuse in the cathode material. On the other hand, at lower lithium concentrations, lithium diffuses as fast as sulfur, minimizing diffusion-induced stress.

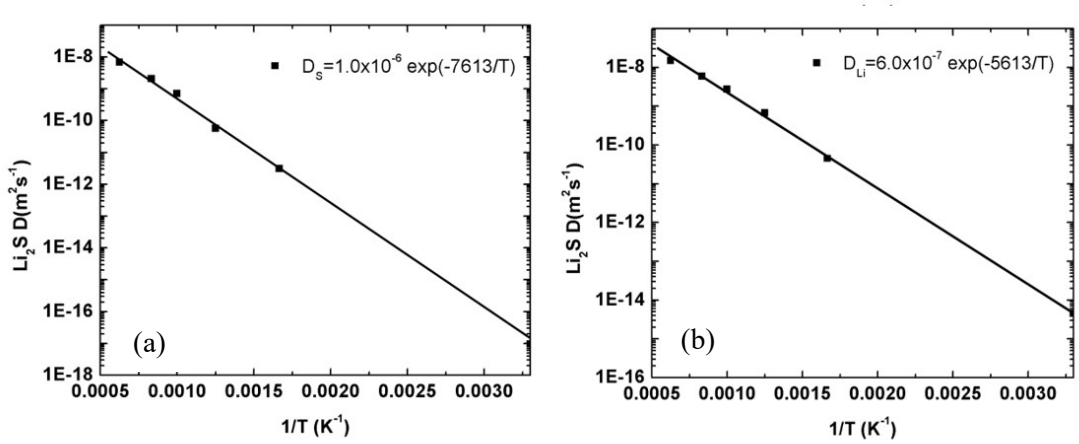

Figure 6-9 Arrhenius plot for calculating diffusion coefficient at 300K, (a) sulfur, and (b) lithium

It is evident that diffusivity of both species depends strongly on the lithium concentration. Interestingly, lithium and sulfur DCs decrease initially with the lithiation, but this trend soon reverses. We observe that DCs of both species are of the same order of magnitude up to $Li_{1.2}S$. However, further lithiation increases Li diffusivity to two orders of magnitude higher than that of S, which indicates that at higher lithium concentration, Li is the dominating diffusion species.

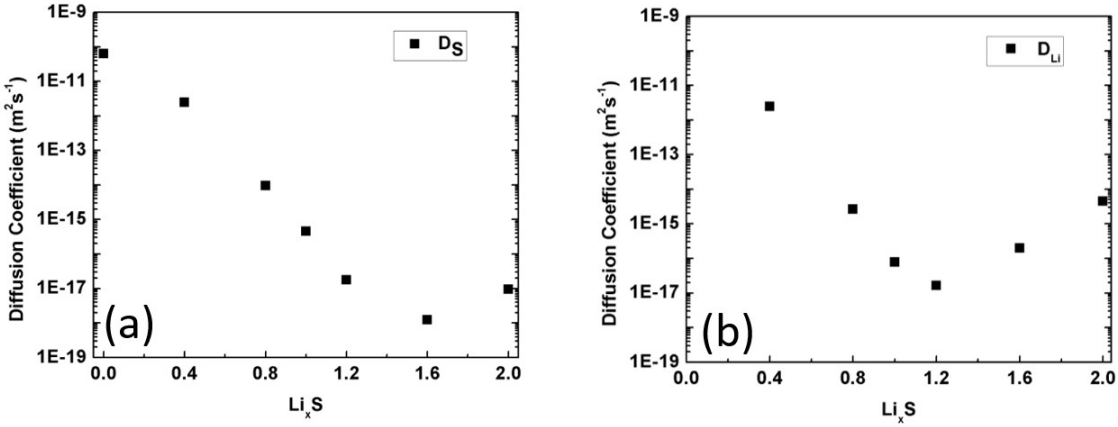

Figure 6-10 Diffusion coefficient of (a) sulfur, and (b) lithium at 300K, calculated using Arrhenius relation.

Our calculated range of the lithium DCs is comparable with the typical range of lithium diffusivity in the conventional transition metal oxide/phosphate cathodes.[204,205] However, given that the insulating characteristics of Li_xS compositions, apparently, our extrapolated data is the upper bound to the Li and S diffusion coefficients. The diffusivity of lithium or sulfur in the Li_xS compounds exhibits an opposing behavior that of the a-Li_xSi alloys. Lithiation in Si increases lithium and silicon diffusivity initially. However, with further lithiation, the diffusivity of both species dwindles.[156]

6.6 Conclusions

We developed a ReaxFF potential for describing Li-S interactions and performed MD simulations to study various structural, mechanical, and diffusion properties in a-Li_xS compounds. ReaxFF reproduces the experimental open circuit voltage profile during cell discharge. The volume expansion of the a-LixS compositions captured in our simulations matches experimental observations well. The phase diagram produced by a GA search of the potential provides information about the formation energies of the various Li_xS phases as a function of composition. GA scheme exhibits that experimentally known Li_2S structure lies in a very close proximity of the convex hull, i.e. ground state. Our simulations for calculating mechanical properties of a-Li_xS illustrate that lithiated sulfur compounds undergo strain hardening with lithiation, which results in an increase in strength and toughness. Dependence of the mechanical properties of a-Li_xS compounds on strain rate is observed: the material exhibits higher strength with increasing strain rate. Young Modulus from our calculations was found in good agreement with the extrapolated experimental values. Diffusion coefficients of both lithium and sulfur are contingent on the lithium content in a-Li_xS compositions. These demonstrate that the developed Li-S potential can accurately describe Li-S chemistry.

This newly developed Li-S potential and its application to lithiated sulfur systems provide a new perspective on lithiation induced mechanical responses of sulfur cathodes at the most fundamental atomistic level. The computed material properties will enable the development of a continuum model to further investigate the morphological evolution, degradation, and failure mechanism of lithiated sulfur during electrochemical cycling for specimens of experimental length and time scale. We believe these atomistic-level insights will play a vital role in designing cathode materials for high-performance Li-S batteries to meet future energy demand.

Chapter 7

Conclusions and Outlook

In this dissertation, we studied electrode-electrolyte interfacial chemistries and electrode material properties of Li-batteries. The following sections summarize the findings and outlook of this dissertation.

We developed a new computational method, eReaxFF, within the basic framework of the ReaxFF method for simulating redox reactions. New functionals are added into the ReaxFF to describe electron/hole interactions with the core charge and the existing over and undercoordination energy terms are modified to account the effect of explicit electrons. In contrast to the widely used polarizable electronegativity equalization method (EEM) for calculating atomic charges, we incorporated atom-condensed Kohn-Sham density functional theory approximated to second order (ACKS2) charge calculation scheme. The ACKS2 scheme eliminates two well-known shortcomings of the EEM method: (i) it assigns fractional charges to dissociated molecules even when they are well separated, and (ii) it predicts a cubic scaling of the dipole polarizability with system size.[65] The unrealistic charge smearing of the EEM method prevents the correct charge distribution of the oxidized or the reduced species. The ACKS2 method penalizes long-range charge transfer with a bond polarization energy. The bond polarizability is a function of interatomic distance, which slightly increases beyond the equilibrium bond length, however then quickly decays to zero, thus fragment neutrality is maintained.[86] The implementation of ACKS2 is very similar to the EEM method. Transferring of EEM parameters to the ACKS2 method requires reparameterization. However EEM parameter sets are usually a good starting point for deriving ACKS2 parameters. The 2-, 3-, and 4- body interaction parameters of the ReaxFF are transferable to the eReaxFF method. Although it is imperative to perform additional training for the electron

interaction with the system, the transferability of the ReaxFF parameters allows developing an eReaxFF version of a force field with a modest effort.

In order to study electron dynamics in hydrocarbon radicals, we trained our eReaxFF force field against electron affinities (EAs) data of a wide range of species, including saturated, unsaturated, and radical species. Our eReaxFF calculations demonstrated a good agreement with the corresponding literature data of the EA values, while the ReaxFF method completely failed to predict the EAs of the species considered in the training set. These simulation results establish the capability of the eReaxFF method to describe chemical species and reactions involving explicit electrons. We employed the force field in studying electron dynamics in two model hydrocarbon radicals at various temperatures. We started molecular dynamics (MD) simulations of the radical anions at their excited state via localizing an extra electron in the conjugated part of the radical. We observed temperature-dependent electron transfer rates from the conjugated to the ground state radical site during MD simulations. The eReaxFF predicted time-scale requirement for the electron transfer event agrees well with the corresponding Ehrenfest dynamics (ED) simulation results. Such an agreement is very encouraging due to the fact that the eReaxFF simulations are a few order of magnitude faster than the ED simulations.

Next, we employed our eReaxFF method in a more complex reactive environment of the anode-electrolyte interface of a Li-ion battery. The mechanism of reductive decomposition of ethylene carbonate (EC) molecules and the formation of a solid electrolyte interphase (SEI) is investigated using the eReaxFF method. In comparison to the literature data,[117] our simulations nicely reproduce the energetics of the EC reduction and the formation of o-EC^{-}/Li^{+} radicals and subsequent radical termination reactions to produce major components of the SEI. Our MD simulations demonstrated the formation of di lithium butyl dicarbonate (Li_2BDC) and di lithium ethyl dicarbonate (Li_2EDC) and ethylene gas, which are the most common reaction products found

experimentally, and usually considered as the dominant components of the anode surface SEI. These simulation results establish that the eReaxFF method can be effectively used to describe complex reactive systems involving electron flow.

Apart from the eReaxFF simulations, we also used standard ReaxFF method to study Li-S battery chemistry and sulfur cathode material properties. We observed that the usage of lithium loaded carbon nanotube (CNT) anode could prevent lithium dendrite growth during battery cycling. Our simulation indicates that the process of lithium release from the anode to electrolytes is highly exothermic. This exothermic process increases the interfacial temperature and accelerates reaction kinetics of the electrolyte dissociation. As a countermeasure to the electrolyte dissociation, we used a porous Teflon coating as an *ex-situ* passivating layer. The lithium cations released from the anode at first exchange heat with the porous Teflon coating, and the coating can withstand the increased interfacial temperature. We found that the lithium cations which are diffused through the Teflon coating and come in contact with the electrolyte are less reactive because of their lower temperature. Therefore, the diffusion of the lithium cations at a lower temperature prevent electrolyte destruction. Our simulations predicted a significant stabilization of the electrolyte molecules when a Teflon coating is employed. Therefore, these simulation results can be a guide for the future experimental studies to investigate the role of Teflon coating to improve Li-S battery performance.

We also developed a Li/S ReaxFF description to explore the structural, mechanical, and kinetic behavior of lithiated sulfur cathode materials. The force field accurately reproduces experimental open circuit voltage profile during Li-S battery discharge, captures the volume expansion of sulfur upon lithiation, and predicts Li-S phase diagram. These validation calculations demonstrate that our force field can correctly capture the chemistry of Li-S interactions. The radial distribution functions calculated from the room temperature MD simulations describe the structural evolution of lithiated sulfur compounds. We found that with the increasing lithium content

mechanical properties of the lithiated sulfur compositions improves. Our calculated Young's modulus data of Li_2S agrees well with the literature data. A recent experimental study performed by Chen et al.[206] validated our observed failure mechanism of lithiated sulfur compositions. It is found that fracture initiates via the formation of small voids, followed by the coalescence of multiple voids that leads to necking and eventually results in rupture.[206] We believe these atomistic-level insights will play a vital role in designing cathode materials for high-performance Li-S batteries to meet future energy demand.

Future work

We predict that our newly developed eReaxFF method will open a new direction of simulations towards the coupling between explicit electron flow and chemistry to describe various systems and materials. We propose following simulations as future directions:

- The cathode-electrolyte interface of Li-ion batteries undergoes oxidative decomposition reactions. The explicit hole description of the eReaxFF will enable the study of oxidation reactions and SEI formation at the cathode site.
- The capability of the eReaxFF to describe polarization behavior under the application of an external electric field is an important aspect of studying structural properties, complex domain walls and their mobility, cracks and failure, impurities, and defects of the piezo and ferro electric materials. Therefore, the eReaxFF method can be employed to study piezo and ferro electric materials, where commonly available classical force field based methods are unable to describe polarizability of these complex materials.
- Li metal anode has a very high capacity of 3868 $mAhg^{-1}$; however, the growth of dendritic structures during battery cycling raises a severe safety concern. Therefore, modeling of the dendrite growth in the presence of various electrolytes, and finding a countermeasure to prevent

dendrite formation is crucial for designing Li-batteries with the metallic lithium anode. The explicit electronic access of the eReaxFF method can adequately model lithium plating and deplating on the anode surface during battery charging and discharging, respectively.

- The ReaxFF method has difficulties in describing ionic liquid systems properly because of the devoid of explicit electron and hole description. The electron and hole degrees of freedom of the eReaxFF method allow the description of anion and cation pairs of an ionic liquid system. Thus eReaxFF will be a very useful tool for studying ionic liquid properties and associated chemistries.
- The water-splitting technology is a clean and renewable means to generate hydrogen using solar energy. The mechanism requires the splitting of the generated electron–hole pairs from light irradiation on the photo-anode. The oxidation of water by photo-generated holes on the photo-anode surface produces O_2 and H^+. The photo-generated electrons reduces the H^+ at the cathode to produce H_2.[207] To model these water splitting reactions through the separation of an electron-hole pair require an explicit electron and hole pair description. The eReaxFF can be applied to investigate these photochemical reactions exploiting its electron and hole degrees of freedom.

References

(1) Dunn, B.; Kamath, H.; Tarascon, J.-M. Electrical Energy Storage for the Grid: A Battery of Choices. *Science* **2011**, *334* (6058), 928–935.

(2) Goodenough, J. B.; M. V. Buchanan. *Basic Research Needs for Electrical Energy storage." Report of the Basic Energy Sciences Workshop for Electrical Energy Storage. Vol. 186. 2007.*

(3) Song, M.-K.; Cairns, E. J.; Zhang, Y. Lithium/sulfur Batteries with High Specific Energy: Old Challenges and New Opportunities. *Nanoscale* **2013**, *5* (6), 2186–2204.

(4) Bouchet, R. Batteries: A Stable Lithium Metal Interface. *Nat. Nanotechnol.* **2014**, *9* (8), 572–573.

(5) Pollet, B. G.; Staffell, I.; Shang, J. L. Current Status of Hybrid, Battery and Fuel Cell Electric Vehicles: From Electrochemistry to Market Prospects. *Electrochimica Acta* **2012**, *84*, 235–249.

(6) Palacín, M. R.; Guibert, A. de. Why Do Batteries Fail? *Science* **2016**, *351* (6273), 1253292.

(7) Tarascon, J.-M.; Armand, M. Issues and Challenges Facing Rechargeable Lithium Batteries. *Nature* **2001**, *414* (6861), 359–367.

(8) Daniel, C.; Besenhard, J. O. *Handbook of Battery Materials*; John Wiley & Sons, 2013.

(9) Mizushima, K.; Jones, P. C.; Wiseman, P. J.; Goodenough, J. B. LixCoO2 (0. *Mater. Res. Bull.* **1980**, *15* (6), 783–789.

(10) Lazzari, M.; Scrosati, B. A Cyclable Lithium Organic Electrolyte Cell Based on Two Intercalation Electrodes. *J. Electrochem. Soc.* **1980**, *127* (3), 773–774.

(11) Murphy, D. W.; Di Salvo, F. J.; Carides, J. N.; Waszczak, J. V. Topochemical Reactions of Rutile Related Structures with Lithium. *Mater. Res. Bull.* **1978**, *13* (12), 1395–1402.

(12) Horiba, T. Lithium-Ion Battery Systems. *Proc. IEEE* **2014**, *102* (6), 939–950.

(13) Goodenough, J. B.; Park, K.-S. The Li-Ion Rechargeable Battery: A Perspective. *J. Am. Chem. Soc.* **2013**, *135* (4), 1167–1176.

(14) Nitta, N.; Wu, F.; Lee, J. T.; Yushin, G. Li-Ion Battery Materials: Present and Future. *Mater. Today*.

(15) Ostadhossein, A.; Cubuk, E. D.; Tritsaris, G. A.; Kaxiras, E.; Zhang, S.; Duin, A. C. T. van. Stress Effects on the Initial Lithiation of Crystalline Silicon Nanowires: Reactive Molecular Dynamics Simulations Using ReaxFF. *Phys. Chem. Chem. Phys.* **2015**, *17* (5), 3832–3840.

(16) Du Pasquier, A.; Plitz, I.; Menocal, S.; Amatucci, G. A Comparative Study of Li-Ion Battery, Supercapacitor and Nonaqueous Asymmetric Hybrid Devices for Automotive Applications. *J. Power Sources* **2003**, *115* (1), 171–178.

(17) Park, J.-K. *Principles and Applications of Lithium Secondary Batteries*; John Wiley & Sons, 2012.

(18) Nitta, N.; Yushin, G. High-Capacity Anode Materials for Lithium-Ion Batteries: Choice of Elements and Structures for Active Particles. *Part. Part. Syst. Charact.* **2014**, *31* (3), 317–336.

(19) Thackeray, M. M.; de Picciotto, L. A.; de Kock, A.; Johnson, P. J.; Nicholas, V. A.; Adendorff, K. T. Spinel Electrodes for Lithium Batteries — A Review. *J. Power Sources* **1987**, *21* (1), 1–8.

(20) Sun, Y.-K.; Yoon, C. S.; Oh, I.-H. Surface Structural Change of ZnO-Coated LiNi0.5Mn1.5O4 Spinel as 5 V Cathode Materials at Elevated Temperatures. *Electrochimica Acta* **2003**, *48* (5), 503–506.

(21) Kakuda, T.; Uematsu, K.; Toda, K.; Sato, M. Electrochemical Performance of Al-Doped LiMn2O4 Prepared by Different Methods in Solid-State Reaction. *J. Power Sources* **2007**, *167* (2), 499–503.

(22) Chen, Z.; Amine, K. Capacity Fade of Li1 + X Mn2 − X O4-Based Lithium-Ion Cells. *J. Electrochem. Soc.* **2006**, *153* (2), A316–A320.

(23) Landi, B. J.; Ganter, M. J.; Cress, C. D.; DiLeo, R. A.; Raffaelle, R. P. Carbon Nanotubes for Lithium Ion Batteries. *Energy Environ. Sci.* **2009**, *2* (6), 638–654.

(24) Broussely, M.; Biensan, P.; Simon, B. Lithium Insertion into Host Materials: The Key to Success for Li Ion Batteries. *Electrochimica Acta* **1999**, *45* (1–2), 3–22.

(25) Tanaka, T.; Ohta, K.; Arai, N. Year 2000 R&D Status of Large-Scale Lithium Ion Secondary Batteries in the National Project of Japan. *J. Power Sources* **2001**, *97–98*, 2–6.

(26) Terada, N.; Yanagi, T.; Arai, S.; Yoshikawa, M.; Ohta, K.; Nakajima, N.; Yanai, A.; Arai, N. Development of Lithium Batteries for Energy Storage and EV Applications. *J. Power Sources* **2001**, *100* (1–2), 80–92.

(27) Aurbach, D.; Talyosef, Y.; Markovsky, B.; Markevich, E.; Zinigrad, E.; Asraf, L.; Gnanaraj, J. S.; Kim, H.-J. Design of Electrolyte Solutions for Li and Li-Ion Batteries: A Review. *Electrochimica Acta* **2004**, *50* (2–3), 247–254.

(28) Li, Z. Molecular Dynamics Simulation Studies of Ionic Liquids Electrolytes for Lithium Ion Batteries, The University of Utah, 2012.

(29) Sun, X.-G.; Angell, C. A. New Sulfone Electrolytes for Rechargeable Lithium Batteries.: Part I. Oligoether-Containing Sulfones. *Electrochem. Commun.* **2005**, *7* (3), 261–266.

(30) Markervich, E.; Salitra, G.; Levi, M. D.; Aurbach, D. Capacity Fading of Lithiated Graphite Electrodes Studied by a Combination of Electroanalytical Methods, Raman Spectroscopy and SEM. *J. Power Sources* **2005**, *146* (1), 146–150.

(31) Peled, E. The Electrochemical Behavior of Alkali and Alkaline Earth Metals in Nonaqueous Battery Systems—the Solid Electrolyte Interphase Model. *J. Electrochem. Soc.* **1979**, *126* (12), 2047–2051.

(32) Aurbach, D. Review of Selected Electrode–solution Interactions Which Determine the Performance of Li and Li Ion Batteries. *J. Power Sources* **2000**, *89* (2), 206–218.

(33) Aurbach, D.; Markovsky, B.; Levi, M. .; Levi, E.; Schechter, A.; Moshkovich, M.; Cohen, Y. New Insights into the Interactions between Electrode Materials and Electrolyte Solutions for Advanced Nonaqueous Batteries. *J. Power Sources* **1999**, *81–82*, 95–111.

(34) Xu, K. Nonaqueous Liquid Electrolytes for Lithium-Based Rechargeable Batteries. *Chem. Rev.* **2004**, *104* (10), 4303–4418.

(35) Glen Ferguson; Larry A. Curtiss. Atomic-Level Modeling of Organic Electrolytes in Lithium-Ion Batteries. In *Applications of Molecular Modeling to Challenges in Clean Energy*; ACS Symposium Series; American Chemical Society, 2013; Vol. 1133, pp 217–233.

(36) Xu, K.; Cresce, A. von. Interfacing Electrolytes with Electrodes in Li Ion Batteries. *J. Mater. Chem.* **2011**, *21* (27), 9849–9864.

(37) Tang, M.; Miyazaki, K.; Abe, T.; Newman, J. Effect of Graphite Orientation and Lithium Salt on Electronic Passivation of Highly Oriented Pyrolytic Graphite. *J. Electrochem. Soc.* **2012**, *159* (5), A634–A641.

(38) Besenhard, J. O.; Winter, M.; Yang, J.; Biberacher, W. Filming Mechanism of Lithium-Carbon Anodes in Organic and Inorganic Electrolytes. *J. Power Sources* **1995**, *54* (2), 228–231.

(39) Winter, M.; Besenhard, J. O. Electrochemical Lithiation of Tin and Tin-Based Intermetallics and Composites. *Electrochimica Acta* **1999**, *45* (1), 31–50.

(40) Aurbach, D.; Levi, M. D.; Levi, E.; Schechter, A. Failure and Stabilization Mechanisms of Graphite Electrodes. *J. Phys. Chem. B* **1997**, *101* (12), 2195–2206.

(41) Mikhaylik, Y. V.; Akridge, J. R. Polysulfide Shuttle Study in the Li/S Battery System. *J. Electrochem. Soc.* **2004**, *151* (11), A1969–A1976.

(42) Ji, X.; Lee, K. T.; Nazar, L. F. A Highly Ordered Nanostructured Carbon–sulphur Cathode for Lithium–sulphur Batteries. *Nat. Mater.* **2009**, *8* (6), 500–506.

(43) Shim, J.; Striebel, K. A.; Cairns, E. J. The Lithium/Sulfur Rechargeable Cell Effects of Electrode Composition and Solvent on Cell Performance. *J. Electrochem. Soc.* **2002**, *149* (10), A1321–A1325.

(44) Cheon, S.-E.; Ko, K.-S.; Cho, J.-H.; Kim, S.-W.; Chin, E.-Y.; Kim, H.-T. Rechargeable Lithium Sulfur Battery I. Structural Change of Sulfur Cathode During Discharge and Charge. *J. Electrochem. Soc.* **2003**, *150* (6), A796–A799.

(45) Cheon, S.-E.; Ko, K.-S.; Cho, J.-H.; Kim, S.-W.; Chin, E.-Y.; Kim, H.-T. Rechargeable Lithium Sulfur Battery II. Rate Capability and Cycle Characteristics. *J. Electrochem. Soc.* **2003**, *150* (6), A800–A805.

(46) Choi, N.-S.; Chen, Z.; Freunberger, S. A.; Ji, X.; Sun, Y.-K.; Amine, K.; Yushin, G.; Nazar, L. F.; Cho, J.; Bruce, P. G. Challenges Facing Lithium Batteries and Electrical Double-Layer Capacitors. *Angew. Chem. Int. Ed.* **2012**, *51* (40), 9994–10024.

(47) Hassoun, J.; Kim, J.; Lee, D.-J.; Jung, H.-G.; Lee, S.-M.; Sun, Y.-K.; Scrosati, B. A Contribution to the Progress of High Energy Batteries: A Metal-Free, Lithium-Ion, Silicon–sulfur Battery. *J. Power Sources* **2012**, *202*, 308–313.

(48) Ryu, H. S.; Ahn, H. J.; Kim, K. W.; Ahn, J. H.; Lee, J. Y.; Cairns, E. J. Self-Discharge of Lithium–sulfur Cells Using Stainless-Steel Current-Collectors. *J. Power Sources* **2005**, *140* (2), 365–369.

(49) Chang, D.-R.; Lee, S.-H.; Kim, S.-W.; Kim, H.-T. Binary Electrolyte Based on Tetra(ethylene Glycol) Dimethyl Ether and 1,3-Dioxolane for Lithium–sulfur Battery. *J. Power Sources* **2002**, *112* (2), 452–460.

(50) Kim, S.; Jung, Y.; Park, S.-J. Effects of Imidazolium Salts on Discharge Performance of Rechargeable Lithium–sulfur Cells Containing Organic Solvent Electrolytes. *J. Power Sources* **2005**, *152*, 272–277.

(51) Peled, E.; Sternberg, Y.; Gorenshtein, A.; Lavi, Y. Lithium-Sulfur Battery: Evaluation of Dioxolane-Based Electrolytes. *J. Electrochem. Soc.* **1989**, *136* (6), 1621–1625.

(52) Zheng, G.; Yang, Y.; Cha, J. J.; Hong, S. S.; Cui, Y. Hollow Carbon Nanofiber-Encapsulated Sulfur Cathodes for High Specific Capacity Rechargeable Lithium Batteries. *Nano Lett.* **2011**, *11* (10), 4462–4467.

(53) Leung, K.; Budzien, J. L. Ab Initio Molecular Dynamics Simulations of the Initial Stages of Solid–electrolyte Interphase Formation on Lithium Ion Battery Graphitic Anodes. *Phys. Chem. Chem. Phys.* **2010**, *12* (25), 6583–6586.

(54) Ganesh, P.; Kent, P. R. C.; Jiang, D. Solid–Electrolyte Interphase Formation and Electrolyte Reduction at Li-Ion Battery Graphite Anodes: Insights from First-Principles Molecular Dynamics. *J. Phys. Chem. C* **2012**, *116* (46), 24476–24481.

(55) Ganesh, P.; Jiang, D.; Kent, P. R. C. Accurate Static and Dynamic Properties of Liquid Electrolytes for Li-Ion Batteries from Ab Initio Molecular Dynamics. *J. Phys. Chem. B* **2011**, *115* (12), 3085–3090.

(56) Yu, J.; Balbuena, P. B.; Budzien, J.; Leung, K. Hybrid DFT Functional-Based Static and Molecular Dynamics Studies of Excess Electron in Liquid Ethylene Carbonate. *J. Electrochem. Soc.* **2011**, *158* (4), A400–A410.

(57) Leung, K.; Qi, Y.; Zavadil, K. R.; Jung, Y. S.; Dillon, A. C.; Cavanagh, A. S.; Lee, S.-H.; George, S. M. Using Atomic Layer Deposition to Hinder Solvent Decomposition in

Lithium Ion Batteries: First-Principles Modeling and Experimental Studies. *J. Am. Chem. Soc.* **2011**, *133* (37), 14741–14754.

(58) Leung, K. Two-Electron Reduction of Ethylene Carbonate: A Quantum Chemistry Re-Examination of Mechanisms. *Chem. Phys. Lett.* **2013**, *568–569*, 1–8.

(59) Leung, K. Electronic Structure Modeling of Electrochemical Reactions at Electrode/Electrolyte Interfaces in Lithium Ion Batteries. *J. Phys. Chem. C* **2013**, *117* (4), 1539–1547.

(60) Van Duin, A. C.; Dasgupta, S.; Lorant, F.; Goddard, W. A. ReaxFF: A Reactive Force Field for Hydrocarbons. *J. Phys. Chem. A* **2001**, *105* (41), 9396–9409.

(61) Tersoff, J. Empirical Interatomic Potential for Carbon, with Applications to Amorphous Carbon. *Phys. Rev. Lett.* **1988**, *61* (25), 2879–2882.

(62) Brenner, D. W. Empirical Potential for Hydrocarbons for Use in Simulating the Chemical Vapor Deposition of Diamond Films. *Phys. Rev. B* **1990**, *42* (15), 9458–9471.

(63) Van Duin, A. C.; Strachan, A.; Stewman, S.; Zhang, Q.; Xu, X.; Goddard, W. A. ReaxFFSiO Reactive Force Field for Silicon and Silicon Oxide Systems. *J. Phys. Chem. A* **2003**, *107* (19), 3803–3811.

(64) Mortier, W. J.; Ghosh, S. K.; Shankar, S. Electronegativity-Equalization Method for the Calculation of Atomic Charges in Molecules. *J. Am. Chem. Soc.* **1986**, *108* (15), 4315–4320.

(65) Verstraelen, T.; Ayers, P. W.; Speybroeck, V. V.; Waroquier, M. ACKS2: Atom-Condensed Kohn-Sham DFT Approximated to Second Order. *J. Chem. Phys.* **2013**, *138* (7), 74108.

(66) Islam, M. M.; Kolesov, G.; Verstraelen, T.; Kaxiras, E.; van Duin, A. C. eReaxFF: A Pseudo-Classical Treatment of Explicit Electrons within Reactive Force Field Simulations. *J. Chem. Theory Comput.* **2016**.

(67) Castro, A.; Marques, M. a. L.; Alonso, J. A.; Bertsch, G. F.; Rubio, A. Excited States Dynamics in Time-Dependent Density Functional Theory. *Eur. Phys. J. - At. Mol. Opt. Plasma Phys.* **2003**, *28* (2), 211–218.

(68) Ehrenfest Dynamcis. *G. Kolesov G, O. Grånäs, R. Hoyt, D. Vinichenko and E. Kaxiras J. Theor. Comput. Chem, 2016 12(2):466-76*.

(69) Stuart, S. J.; Tutein, A. B.; Harrison, J. A. A Reactive Potential for Hydrocarbons with Intermolecular Interactions. *J. Chem. Phys.* **2000**, *112* (14), 6472–6486.

(70) Tersoff, J. New Empirical Approach for the Structure and Energy of Covalent Systems. *Phys. Rev. B* **1988**, *37* (12), 6991–7000.

(71) Su, J. T.; Goddard III, W. A. The Dynamics of Highly Excited Electronic Systems: Applications of the Electron Force Field. *J. Chem. Phys.* **2009**, *131* (24), 244501.

(72) Su, J. T.; Goddard, W. A. Excited Electron Dynamics Modeling of Warm Dense Matter. *Phys. Rev. Lett.* **2007**, *99* (18), 185003.

(73) Kale, S.; Herzfeld, J.; Dai, S.; Blank, M. Lewis-Inspired Representation of Dissociable Water in Clusters and Grotthuss Chains. *J. Biol. Phys.* **2012**, *38* (1), 49–59.

(74) Kale, S.; Herzfeld, J. Pairwise Long-Range Compensation for Strongly Ionic Systems. *J. Chem. Theory Comput.* **2011**, *7* (11), 3620–3624.

(75) Kale, S.; Herzfeld, J. Natural Polarizability and Flexibility via Explicit Valency: The Case of Water. *J. Chem. Phys.* **2012**, *136* (8), 84109.

(76) Ekesan, S.; Herzfeld, J. Pointillist Rendering of Electron Charge and Spin Density Suffices to Replicate Trends in Atomic Properties. *Proc R Soc A* **2015**, *471* (2181), 20150370.

(77) Ekesan, S.; Kale, S.; Herzfeld, J. Transferable Pseudoclassical Electrons for Aufbau of Atomic Ions. *J. Comput. Chem.* **2014**, *35* (15), 1159–1164.

(78) Kale, S. *Reactive Force Fields via Explicit Valency*; 2012; Vol. 73–09(E).

(79) Mikulski, P. T.; Knippenberg, M. T.; Harrison, J. A. Merging Bond-Order Potentials with Charge Equilibration. *J. Chem. Phys.* **2009**, *131* (24), 241105.

(80) Nistor, R. A.; Polihronov, J. G.; Müser, M. H.; Mosey, N. J. A Generalization of the Charge Equilibration Method for Nonmetallic Materials. *J. Chem. Phys.* **2006**, *125* (9), 94108.

(81) Knippenberg, M. T.; Mikulski, P. T.; Ryan, K. E.; Stuart, S. J.; Gao, G.; Harrison, J. A. Bond-Order Potentials with Split-Charge Equilibration: Application to C-, H-, and O-Containing Systems. *J. Chem. Phys.* **2012**, *136* (16), 164701.

(82) Chenoweth, K.; van Duin, A. C. T.; Goddard, W. A. ReaxFF Reactive Force Field for Molecular Dynamics Simulations of Hydrocarbon Oxidation. *J. Phys. Chem. A* **2008**, *112* (5), 1040–1053.

(83) Liang, T.; Shin, Y. K.; Cheng, Y.-T.; Yilmaz, D. E.; Vishnu, K. G.; Verners, O.; Zou, C.; Phillpot, S. R.; Sinnott, S. B.; van Duin, A. C. T. Reactive Potentials for Advanced Atomistic Simulations. *Annu. Rev. Mater. Res.* **2013**, *43* (1), 109–129.

(84) Verners, O.; Psofogiannakis, G.; van Duin, A. C. T. Comparative Molecular Dynamics Study of Fcc-Al Hydrogen Embrittlement. *Corros. Sci.* **2015**, *98*, 40–49.

(85) Buehler, M. J.; van Duin, A. C.; Goddard III, W. A. Multiparadigm Modeling of Dynamical Crack Propagation in Silicon Using a Reactive Force Field. *Phys. Rev. Lett.* **2006**, *96* (9), 95505.

(86) Senftle, T. P.; Hong, S.; Islam, M. M.; Kylasa, S. B.; Zheng, Y.; Shin, Y. K.; Junkermeier, C.; Engel-Herbert, R.; Janik, M. J.; Aktulga, H. M.; et al. The ReaxFF Reactive Force-Field: Development, Applications and Future Directions. *Npj Comput. Mater.* **2016**, *2*, 15011.

(87) Islam, M. M.; Zou, C.; van Duin, A. C. T.; Raman, S. Interactions of Hydrogen with the Iron and Iron Carbide Interfaces: A ReaxFF Molecular Dynamics Study. *Phys. Chem. Chem. Phys.* **2015**.

(88) Zhang, Q.; Çağın, T.; van Duin, A.; Goddard III, W. A.; Qi, Y.; Hector Jr, L. G. Adhesion and Nonwetting-Wetting Transition in the Al/α- Al 2 O 3 Interface. *Phys. Rev. B* **2004**, *69* (4), 45423.

(89) Nomura, K.; Kalia, R. K.; Nakano, A.; Vashishta, P. A Scalable Parallel Algorithm for Large-Scale Reactive Force-Field Molecular Dynamics Simulations. *Comput. Phys. Commun.* **2008**, *178* (2), 73–87.

(90) Russo Jr., M. F.; van Duin, A. C. T. Atomistic-Scale Simulations of Chemical Reactions: Bridging from Quantum Chemistry to Engineering. *Nucl. Instrum. Methods Phys. Res. Sect. B Beam Interact. Mater. At.* **2011**, *269* (14), 1549–1554.

(91) Islam, M. M.; Ostadhossein, A.; Borodin, O.; Yeates, A. T.; Tipton, W. W.; Hennig, R. G.; Kumar, N.; Duin, A. C. T. van. ReaxFF Molecular Dynamics Simulations on Lithiated Sulfur Cathode Materials. *Phys. Chem. Chem. Phys.* **2015**, *17* (5), 3383–3393.

(92) Islam, M. M.; Bryantsev, V. S.; Duin, A. C. T. van. ReaxFF Reactive Force Field Simulations on the Influence of Teflon on Electrolyte Decomposition during Li/SWCNT Anode Discharge in Lithium-Sulfur Batteries. *J. Electrochem. Soc.* **2014**, *161* (8), E3009–E3014.

(93) Goverapet Srinivasan, S.; van Duin, A. C. T. Molecular-Dynamics-Based Study of the Collisions of Hyperthermal Atomic Oxygen with Graphene Using the ReaxFF Reactive Force Field. *J. Phys. Chem. A* **2011**, *115* (46), 13269–13280.

(94) Bedrov, D.; Smith, G. D.; van Duin, A. C. Reactions of Singly-Reduced Ethylene Carbonate in Lithium Battery Electrolytes: A Molecular Dynamics Simulation Study Using the ReaxFF. *J. Phys. Chem. A* **2012**, *116* (11), 2978–2985.

(95) Www.scm.com. *www.scm.com*.

(96) Cioslowski, J.; Stefanov, B. B. Electron Flow and Electronegativity Equalization in the Process of Bond Formation. *J. Chem. Phys.* **1993**, *99* (7), 5151–5162.

(97) Warren, G. L.; Davis, J. E.; Patel, S. Origin and Control of Superlinear Polarizability Scaling in Chemical Potential Equalization Methods. *J. Chem. Phys.* **2008**, *128* (14), 144110.

(98) Nistor, R. A.; Müser, M. H. Dielectric Properties of Solids in the Regular and Split-Charge Equilibration Formalisms. *Phys. Rev. B* **2009**, *79* (10), 104303.

(99) Louwen, J. N.; Vogt, E. T. C. Semi-Empirical Atomic Charges for Use in Computational Chemistry of Molecular Sieves. *J. Mol. Catal. Chem.* **1998**, *134* (1–3), 63–77.

(100) van Duin, A. C. T.; Baas, J. M. A.; van de Graaf, B. Delft Molecular Mechanics: A New Approach to Hydrocarbon Force Fields. Inclusion of a Geometry-Dependent Charge Calculation. *J. Chem. Soc. Faraday Trans.* **1994**, *90* (19), 2881.

(101) Rienstra-Kiracofe, J. C.; Tschumper, G. S.; Schaefer, H. F.; Nandi, S.; Ellison, G. B. Atomic and Molecular Electron Affinities: Photoelectron Experiments and Theoretical Computations. *Chem. Rev.* **2002**, *102* (1), 231–282.

(102) Jordan, K. D.; Burrow, P. D. Studies of the Temporary Anion States of Unsaturated Hydrocarbons by Electron Transmission Spectroscopy. *Acc. Chem. Res.* **1978**, *11* (9), 341–348.

(103) *Jaguar, Version 7.5, Schrödinger, LLC: New York*; 2008.

(104) Marcus, R. A.; Sutin, N. Electron Transfers in Chemistry and Biology. *Biochim. Biophys. Acta BBA - Rev. Bioenerg.* **1985**, *811* (3), 265–322.

(105) Berendsen, H. J. C.; Postma, J. P. M.; van Gunsteren, W. F.; DiNola, A.; Haak, J. R. Molecular Dynamics with Coupling to an External Bath. *J. Chem. Phys.* **1984**, *81* (8), 3684–3690.

(106) Meng, S.; Kaxiras, E. Real-Time, Local Basis-Set Implementation of Time-Dependent Density Functional Theory for Excited State Dynamics Simulations. *J. Chem. Phys.* **2008**, *129* (5), 54110.

(107) Kolesov, G.; Vinichenko, D.; Tritsaris, G. A.; Friend, C. M.; Kaxiras, E. Anatomy of the Photochemical Reaction: Excited-State Dynamics Reveals the C–H Acidity Mechanism of Methoxy Photo-Oxidation on Titania. *J. Phys. Chem. Lett.* **2015**, *6* (9), 1624–1627.

(108) Tritsaris, G. A.; Vinichenko, D.; Kolesov, G.; Friend, C. M.; Kaxiras, E. Dynamics of the Photogenerated Hole at the Rutile TiO2 (110)/Water Interface: A Nonadiabatic Simulation Study. *J. Phys. Chem. C* **2014**, *118* (47), 27393–27401.

(109) Ehrenfest. *U. Saalmann and R. Schmidt, Zeitschrift fuer Physik D, 1996, 38, 151-163*.

(110) Doltsinis, N. L.; Marx, D. First Principles Molecular Dynamics Involving Excited States and Nonadiabatic Transitions. *J. Theor. Comput. Chem.* **2002**, *1* (2), 319–349.

(111) Runge, E.; Gross, E. K. U. Density-Functional Theory for Time-Dependent Systems. *Phys. Rev. Lett.* **1984**, *52* (12), 997–1000.

(112) Goodenough, J. B.; Kim, Y. Challenges for Rechargeable Batteries. *J. Power Sources* **2011**, *196* (16), 6688–6694.

(113) Aurbach, D.; Ein-Ely, Y.; Zaban, A. The Surface Chemistry of Lithium Electrodes in Alkyl Carbonate Solutions. *J. Electrochem. Soc.* **1994**, *141* (1), L1–L3.

(114) Aurbach, D.; Ein-Eli, Y.; Chusid, O.; Carmeli, Y.; Babai, M.; Yamin, H. The Correlation Between the Surface Chemistry and the Performance of Li-Carbon Intercalation Anodes for Rechargeable “Rocking-Chair”Type Batteries. *J. Electrochem. Soc.* **1994**, *141* (3), 603–611.

(115) Dey, A. N.; Sullivan, B. P. The Electrochemical Decomposition of Propylene Carbonate on Graphite. *J. Electrochem. Soc.* **1970**, *117* (2), 222–224.

(116) Aurbach, D.; Moshkovich, M.; Cohen, Y.; Schechter, A. The Study of Surface Film Formation on Noble-Metal Electrodes in Alkyl Carbonates/Li Salt Solutions, Using Simultaneous in Situ AFM, EQCM, FTIR, and EIS. *Langmuir* **1999**, *15* (8), 2947–2960.

(117) Wang, Y.; Nakamura, S.; Ue, M.; Balbuena, P. B. Theoretical Studies To Understand Surface Chemistry on Carbon Anodes for Lithium-Ion Batteries: Reduction Mechanisms of Ethylene Carbonate. *J. Am. Chem. Soc.* **2001**, *123* (47), 11708–11718.

(118) Wang, Y.; Balbuena, P. B. Theoretical Insights into the Reductive Decompositions of Propylene Carbonate and Vinylene Carbonate: Density Functional Theory Studies. *J. Phys. Chem. B* **2002**, *106* (17), 4486–4495.

(119) Benitez, L.; Cristancho, D.; Seminario, J. M.; Martinez de la Hoz, J. M.; Balbuena, P. B. Electron Transfer through Solid-Electrolyte-Interphase Layers Formed on Si Anodes of Li-Ion Batteries. *Electrochimica Acta* **2014**, *140*, 250–257.

(120) Kim, S.-P.; Duin, A. C. T. van; Shenoy, V. B. Effect of Electrolytes on the Structure and Evolution of the Solid Electrolyte Interphase (SEI) in Li-Ion Batteries: A Molecular Dynamics Study. *J. Power Sources* **2011**, *196* (20), 8590–8597.

(121) Endo, E.; Tanaka, K.; Sekai, K. Initial Reaction in the Reduction Decomposition of Electrolyte Solutions for Lithium Batteries. *J. Electrochem. Soc.* **2000**, *147* (11), 4029–4033.

(122) Naji, A.; Ghanbaja, J.; Humbert, B.; Willmann, P.; Billaud, D. Electroreduction of Graphite in LiClO4-Ethylene Carbonate Electrolyte. Characterization of the Passivating Layer by Transmission Electron Microscopy and Fourier-Transform Infrared Spectroscopy. *J. Power Sources* **1996**, *63* (1), 33–39.

(123) Bruce, P. G.; Freunberger, S. A.; Hardwick, L. J.; Tarascon, J.-M. Li-O2 and Li-S Batteries with High Energy Storage. *Nat. Mater.* **2012**, *11* (1), 19–29.

(124) Aurbach, D.; Pollak, E.; Elazari, R.; Salitra, G.; Kelley, C. S.; Affinito, J. On the Surface Chemical Aspects of Very High Energy Density, Rechargeable Li–Sulfur Batteries. *J. Electrochem. Soc.* **2009**, *156* (8), A694–A702.

(125) Barghamadi, M.; Kapoor, A.; Wen, C. A Review on Li-S Batteries as a High Efficiency Rechargeable Lithium Battery. *J. Electrochem. Soc.* **2013**, *160* (8), A1256–A1263.

(126) Liang, C.; Dudney, N. J.; Howe, J. Y. Hierarchically Structured Sulfur/Carbon Nanocomposite Material for High-Energy Lithium Battery. *Chem. Mater.* **2009**, *21* (19), 4724–4730.

(127) Whittingham, M. S. Lithium Batteries and Cathode Materials. *Chem. Rev.* **2004**, *104* (10), 4271–4302.

(128) Wang, H.; Zhang, W.-D.; Deng, Z.-Q.; Chen, M.-C. Interaction of Nitrogen with Lithium in Lithium Ion Batteries. *Solid State Ion.* **2009**, *180* (2–3), 212–215.

(129) Osaka, T.; Momma, T.; Matsumoto, Y.; Uchida, Y. Surface Characterization of Electrodeposited Lithium Anode with Enhanced Cycleability Obtained by CO 2 Addition. *J. Electrochem. Soc.* **1997**, *144* (5), 1709–1713.

(130) Dudney, N. J. Addition of a Thin-Film Inorganic Solid Electrolyte (Lipon) as a Protective Film in Lithium Batteries with a Liquid Electrolyte. *J. Power Sources* **2000**, *89* (2), 176–179.

(131) Lee, Y. M.; Choi, N.-S.; Park, J. H.; Park, J.-K. Electrochemical Performance of Lithium/sulfur Batteries with Protected Li Anodes. *J. Power Sources* **2003**, *119–121*, 964–972.

(132) Liang, X.; Wen, Z.; Liu, Y.; Wu, M.; Jin, J.; Zhang, H.; Wu, X. Improved Cycling Performances of Lithium Sulfur Batteries with LiNO3-Modified Electrolyte. *J. Power Sources* **2011**, *196* (22), 9839–9843.

(133) Zhang, S. S. Role of LiNO3 in Rechargeable Lithium/sulfur Battery. *Electrochimica Acta* **2012**, *70*, 344–348.

(134) Choi, J.-W.; Kim, J.-K.; Cheruvally, G.; Ahn, J.-H.; Ahn, H.-J.; Kim, K.-W. Rechargeable Lithium/sulfur Battery with Suitable Mixed Liquid Electrolytes. *Electrochimica Acta* **2007**, *52* (5), 2075–2082.

(135) Yin, Y.-X.; Xin, S.; Guo, Y.-G.; Wan, L.-J. Lithium–Sulfur Batteries: Electrochemistry, Materials, and Prospects. *Angew. Chem. Int. Ed.* **2013**, n/a–n/a.

(136) Ryu, H. S.; Ahn, H. J.; Kim, K. W.; Ahn, J. H.; Cho, K. K.; Nam, T. H. Self-Discharge Characteristics of Lithium/sulfur Batteries Using TEGDME Liquid Electrolyte. *Electrochimica Acta* **2006**, *52* (4), 1563–1566.

(137) Elazari, R.; Salitra, G.; Talyosef, Y.; Grinblat, J.; Scordilis-Kelley, C.; Xiao, A.; Affinito, J.; Aurbach, D. Morphological and Structural Studies of Composite Sulfur Electrodes upon Cycling by HRTEM, AFM and Raman Spectroscopy. *J. Electrochem. Soc.* **2010**, *157* (10), A1131–A1138.

(138) Wang, H.; Yang, Y.; Liang, Y.; Robinson, J. T.; Li, Y.; Jackson, A.; Cui, Y.; Dai, H. Graphene-Wrapped Sulfur Particles as a Rechargeable Lithium–Sulfur Battery Cathode Material with High Capacity and Cycling Stability. *Nano Lett.* **2011**, *11* (7), 2644–2647.

(139) Wang, W.; Wang, Y.; Huang, Y.; Huang, C.; Yu, Z.; Zhang, H.; Wang, A.; Yuan, K. The Electrochemical Performance of Lithium–sulfur Batteries with LiClO4 DOL/DME Electrolyte. *J. Appl. Electrochem.* **2010**, *40* (2), 321–325.

(140) Ryu, H.-S.; Ahn, H.-J.; Kim, K.-W.; Ahn, J.-H.; Cho, K.-K.; Nam, T.-H.; Kim, J.-U.; Cho, G.-B. Discharge Behavior of Lithium/sulfur Cell with TEGDME Based Electrolyte at Low Temperature. *J. Power Sources* **2006**, *163* (1), 201–206.

(141) Gao, B.; Kleinhammes, A.; Tang, X. P.; Bower, C.; Fleming, L.; Wu, Y.; Zhou, O. Electrochemical Intercalation of Single-Walled Carbon Nanotubes with Lithium. *Chem. Phys. Lett.* **1999**, *307* (3–4), 153–157.

(142) Chang, O.-K.; Hall, J. C.; Phillips, J.; Sylvester, L. F. Cell Design for Spirally Wound Rechargeable Alkaline Metal Cell. 4,863,815, September 1989.

(143) Castro-Marcano, F.; Kamat, A. M.; Russo Jr, M. F.; van Duin, A. C.; Mathews, J. P. Combustion of an Illinois No. 6 Coal Char Simulated Using an Atomistic Char Representation and the ReaxFF Reactive Force Field. *Combust. Flame* **2012**, *159* (3), 1272–1285.

(144) Paupitz, R.; Autreto, P. a. S.; Legoas, S. B.; Srinivasan, S. G.; Duin, A. C. T. van; Galvão, D. S. Graphene to Fluorographene and Fluorographane: A Theoretical Study. *Nanotechnology* **2013**, *24* (3), 35706.

(145) Becke, A. D. Density-Functional Exchange-Energy Approximation with Correct Asymptotic Behavior. *Phys. Rev. A* **1988**, *38* (6), 3098.

(146) Lee, C.; Yang, W.; Parr, R. G. Development of the Colle-Salvetti Correlation-Energy Formula into a Functional of the Electron Density. *Phys. Rev. B* **1988**, *37* (2), 785–789.

(147) Schultz, P. A. Charged Local Defects in Extended Systems. *Phys. Rev. Lett.* **2000**, *84* (9), 1942.

(148) Mattsson, A. E.; Schultz, P. A.; Desjarlais, M. P.; Mattsson, T. R.; Leung, K. Designing Meaningful Density Functional Theory Calculations in Materials Science—a Primer. *Model. Simul. Mater. Sci. Eng.* **2005**, *13* (1), R1.

(149) Perdew, J. P.; Burke, K.; Ernzerhof, M. Generalized Gradient Approximation Made Simple. *Phys. Rev. Lett.* **1996**, *77* (18), 3865–3868.

(150) Bryantsev, V. S.; Giordani, V.; Walker, W.; Uddin, J.; Lee, I.; van Duin, A. C. T.; Chase, G. V.; Addison, D. Investigation of Fluorinated Amides for Solid–Electrolyte Interphase

Stabilization in Li–O2 Batteries Using Amide-Based Electrolytes. *J. Phys. Chem. C* **2013**, *117* (23), 11977–11988.

(151) Yang, H.; Bang, H.; Amine, K.; Prakash, J. Investigations of the Exothermic Reactions of Natural Graphite Anode for Li-Ion Batteries during Thermal Runaway. *J. Electrochem. Soc.* **2005**, *152* (1), A73–A79.

(152) Sato, Y.; Murahara, M. Protein Adsorption on PTFE Surface Modified by ArF Excimer Laser Treatment. *J. Adhes. Sci. Technol.* **2004**, *18* (13), 1545–1555.

(153) Nagao, M.; Imade, Y.; Narisawa, H.; Kobayashi, T.; Watanabe, R.; Yokoi, T.; Tatsumi, T.; Kanno, R. All-Solid-State Li–sulfur Batteries with Mesoporous Electrode and Thio-LISICON Solid Electrolyte. *J. Power Sources* **2013**, *222*, 237–242.

(154) Song, M.-K.; Park, S.; Alamgir, F. M.; Cho, J.; Liu, M. Nanostructured Electrodes for Lithium-Ion and Lithium-Air Batteries: The Latest Developments, Challenges, and Perspectives. *Mater. Sci. Eng. R Rep.* **2011**, *72* (11), 203–252.

(155) Chan, M. K. Y.; Wolverton, C.; Greeley, J. P. First Principles Simulations of the Electrochemical Lithiation and Delithiation of Faceted Crystalline Silicon. *J. Am. Chem. Soc.* **2012**, *134* (35), 14362–14374.

(156) Cui, Z.; Gao, F.; Cui, Z.; Qu, J. A Second Nearest-Neighbor Embedded Atom Method Interatomic Potential for Li–Si Alloys. *J. Power Sources* **2012**, *207*, 150–159.

(157) Zhao, K.; Tritsaris, G.; Pharr, M.; Wang, W.; Okeke, O.; Suo, Z.; Vlassak, J.; Kaxiras, E. Reactive Flow in Silicon Electrodes Assisted by the Insertion of Lithium. *NanoLetters* **2012**, *12*, 4397–4403.

(158) Scrosati, B.; Garche, J. Lithium Batteries: Status, Prospects and Future. *J. Power Sources* **2010**, *195* (9), 2419–2430.

(159) Fan, F.; Huang, S.; Yang, H.; Raju, M.; Datta, D.; Shenoy, V. B.; Duin, A. C. T. van; Zhang, S.; Zhu, T. Mechanical Properties of Amorphous LixSi Alloys: A Reactive Force Field Study. *Model. Simul. Mater. Sci. Eng.* **2013**, *21* (7), 74002.

(160) Chou, C.-Y.; Kim, H.; Hwang, G. S. A Comparative First-Principles Study of the Structure, Energetics, and Properties of Li–M (M = Si, Ge, Sn) Alloys. *J. Phys. Chem. C* **2011**, *115* (40), 20018–20026.

(161) Ji, L.; Rao, M.; Zheng, H.; Zhang, L.; Li, Y.; Duan, W.; Guo, J.; Cairns, E. J.; Zhang, Y. Graphene Oxide as a Sulfur Immobilizer in High Performance Lithium/sulfur Cells. *J. Am. Chem. Soc.* **2011**, *133* (46), 18522–18525.

(162) Yang, Y.; McDowell, M. T.; Jackson, A.; Cha, J. J.; Hong, S. S.; Cui, Y. New Nanostructured Li2S/silicon Rechargeable Battery with High Specific Energy. *Nano Lett.* **2010**, *10* (4), 1486–1491.

(163) Zhang, S. S. Liquid Electrolyte Lithium/sulfur Battery: Fundamental Chemistry, Problems, and Solutions. *J. Power Sources* **2013**, *231*, 153–162.

(164) Chen, L.; Shaw, L. L. Recent Advances in Lithium–sulfur Batteries. *J. Power Sources* **2014**, *267*, 770–783.

(165) He, X.; Ren, J.; Wang, L.; Pu, W.; Jiang, C.; Wan, C. Expansion and Shrinkage of the Sulfur Composite Electrode in Rechargeable Lithium Batteries. *J. Power Sources* **2009**, *190* (1), 154–156.

(166) Yuan, L.; Yuan, H.; Qiu, X.; Chen, L.; Zhu, W. Improvement of Cycle Property of Sulfur-Coated Multi-Walled Carbon Nanotubes Composite Cathode for Lithium/sulfur Batteries. *J. Power Sources* **2009**, *189* (2), 1141–1146.

(167) Wu, F.; Magasinski, A.; Yushin, G. Nanoporous Li2S and MWCNT-Linked Li2S Powder Cathodes for Lithium-Sulfur and Lithium-Ion Battery Chemistries. *J. Mater. Chem. A* **2014**, *2* (17), 6064–6070.

(168) Zhang, F.; Zhang, X.; Dong, Y.; Wang, L. Facile and Effective Synthesis of Reduced Graphene Oxide Encapsulated Sulfur via Oil/water System for High Performance Lithium Sulfur Cells. *J Mater Chem* **2012**, *22* (23), 11452–11454.

(169) Kim, J.; Lee, D.-J.; Jung, H.-G.; Sun, Y.-K.; Hassoun, J.; Scrosati, B. An Advanced Lithium-Sulfur Battery. *Adv. Funct. Mater.* **2013**, *23* (8), 1076–1080.

(170) Nishikawa, K.; Fukunaka, Y.; Sakka, T.; Ogata, Y. H.; Selman, J. R. Measurement of Concentration Profiles during Electrodeposition of Li Metal from LiPF6-PC Electrolyte Solution The Role of SEI Dynamics. *J. Electrochem. Soc.* **2007**, *154* (10), A943–A948.

(171) Liu, N.; Hu, L.; McDowell, M. T.; Jackson, A.; Cui, Y. Prelithiated Silicon Nanowires as an Anode for Lithium Ion Batteries. *ACS Nano* **2011**, *5* (8), 6487–6493.

(172) Yang, Y.; Zheng, G.; Misra, S.; Nelson, J.; Toney, M. F.; Cui, Y. High-Capacity Micrometer-Sized Li2S Particles as Cathode Materials for Advanced Rechargeable Lithium-Ion Batteries. *J. Am. Chem. Soc.* **2012**, *134* (37), 15387–15394.

(173) Cai, K.; Song, M.-K.; Cairns, E. J.; Zhang, Y. Nanostructured Li2S–C Composites as Cathode Material for High-Energy Lithium/Sulfur Batteries. *Nano Lett.* **2012**, *12* (12), 6474–6479.

(174) He, X.; Ren, J.; Wang, L.; Pu, W.; Wan, C.; Jiang, C. Electrochemical Characteristics of Sulfur Composite Cathode for Reversible Lithium Storage. *Ionics* **2009**, *15* (4), 477–481.

(175) Jarvis, C. R.; Lain, M. J.; Yakovleva, M. V.; Gao, Y. A Prelithiated Carbon Anode for Lithium-Ion Battery Applications. *J. Power Sources* **2006**, *162* (2), 800–802.

(176) Schmidt, M. W.; Baldridge, K. K.; Boatz, J. A.; Elbert, S. T.; Gordon, M. S.; Jensen, J. H.; Koseki, S.; Matsunaga, N.; Nguyen, K. A.; Su, S.; et al. General Atomic and Molecular Electronic Structure System. *J. Comput. Chem.* **1993**, *14* (11), 1347–1363.

(177) Head-Gordon, M.; Pople, J. A.; Frisch, M. J. MP2 Energy Evaluation by Direct Methods. *Chem. Phys. Lett.* **1988**, *153* (6), 503–506.

(178) Boldyrev, A. I.; Simons, J.; Schleyer, P. von R. Ab Initio Study of the Electronic Structures of Lithium Containing Diatomic Molecules and Ions. *J. Chem. Phys.* **1993**, *99*, 8793.

(179) Wong, M. W.; Steudel, Y.; Steudel, R. Novel Species for the Sulfur Zoo: Isomers of S< Sub> 8</sub>. *Chem. Phys. Lett.* **2002**, *364* (3), 387–392.

(180) Hohenberg, P.; Kohn, W. Inhomogeneous Electron Gas. *Phys. Rev.* **1964**, *136* (3B), B864.

(181) Kohn, W.; Sham, L. J. Self-Consistent Equations Including Exchange and Correlation Effects. *Phys. Rev.* **1965**, *140* (4A), A1133.

(182) Kresse, G.; Hafner, J. Ab Initio Molecular Dynamics for Open-Shell Transition Metals. *Phys. Rev. B* **1993**, *48* (17), 13115.

(183) Kresse, G.; Furthmüller, J. Efficient Iterative Schemes for Ab Initio Total-Energy Calculations Using a Plane-Wave Basis Set. *Phys. Rev. B* **1996**, *54* (16), 11169.

(184) Blöchl, P. E. Projector Augmented-Wave Method. *Phys. Rev. B* **1994**, *50* (24), 17953.

(185) Zintl, E.; Harder, A.; Dauth, B. Lattice Structure of the Oxides, Sulfides, Selenides and Tellurides of Lithium, Sodium and Potassium. *Z Elektrochem Angew Phys Chem* **1934**, *40* (8), 588–593.

(186) Assary, R. S.; Curtiss, L. A.; Moore, J. S. Towards a Molecular Understanding of Energetics in Li-S Batteries Using Non-Aqueous Electrolytes: A High-Level Quantum Chemical Study. *J. Phys. Chem. C* **2014**.

(187) Curtiss, L. A.; Redfern, P. C.; Raghavachari, K. Gaussian-4 Theory. *J. Chem. Phys.* **2007**, *126* (8), 84108.

(188) Plimpton, S. Fast Parallel Algorithms for Short-Range Molecular Dynamics. *J. Comput. Phys.* **1995**, *117* (1), 1–19.

(189) Hoover, W. G. Canonical Dynamics: Equilibrium Phase-Space Distributions. *Phys. Rev. A* **1985**, *31* (3), 1695.

(190) Tipton, W. W.; Bealing, C. R.; Mathew, K.; Hennig, R. G. Structures, Phase Stabilities, and Electrical Potentials of Li-Si Battery Anode Materials. *Phys. Rev. B* **2013**, *87* (18), 184114.

(191) Tipton, W. W.; Hennig, R. G. A Grand Canonical Genetic Algorithm for the Prediction of Multi-Component Phase Diagrams and Testing of Empirical Potentials. *J. Phys. Condens. Matter* **2013**, *25* (49), 495401.

(192) Senftle, T. P.; Janik, M. J.; van Duin, A. C. T. A ReaxFF Investigation of Hydride Formation in Palladium Nanoclusters via Monte Carlo and Molecular Dynamics Simulations. *J. Phys. Chem. C* **2014**.

(193) Senftle, T. P.; Meyer, R. J.; Janik, M. J.; Duin, A. C. T. van. Development of a ReaxFF Potential for Pd/O and Application to Palladium Oxide Formation. *J. Chem. Phys.* **2013**, *139* (4), 44109.

(194) Chen, H.; Dong, W.; Ge, J.; Wang, C.; Wu, X.; Lu, W.; Chen, L. Ultrafine Sulfur Nanoparticles in Conducting Polymer Shell as Cathode Materials for High Performance Lithium/Sulfur Batteries. *Sci. Rep.* **2013**, *3*.

(195) Sutton, L. E. *Tables of Interatomic Distances and Configuration in Molecules and Ions: Supplement 1956-59*; Chemical Society, 1965.

(196) Branício, P. S.; Rino, J.-P. Large Deformation and Amorphization of Ni Nanowires under Uniaxial Strain: A Molecular Dynamics Study. *Phys. Rev. B* **2000**, *62* (24), 16950.

(197) Davis, J. R. *Tensile Testing*; ASM International, 2004.

(198) Falk, M. L.; Langer, J. S. Deformation and Failure of Amorphous Solidlike Materials. *ArXiv Prepr. ArXiv10044684* **2010**.

(199) Khachai, H.; Khenata, R.; Bouhemadou, A.; Reshak, A. H.; Haddou, A.; Rabah, M.; Soudini, B. First Principles Study of the Elastic Properties in X2S (X=Li, Na, K and Rb) Compounds under Pressure Effect. *Solid State Commun.* **2008**, *147* (5–6), 178–182.

(200) Sakuda, A.; Hayashi, A.; Tatsumisago, M. Sulfide Solid Electrolyte with Favorable Mechanical Property for All-Solid-State Lithium Battery. *Sci. Rep.* **2013**, *3*.

(201) Zhao, K.; Wang, W. L.; Gregoire, J.; Pharr, M.; Suo, Z.; Vlassak, J. J.; Kaxiras, E. Lithium-Assisted Plastic Deformation of Silicon Electrodes in Lithium-Ion Batteries: A First-Principles Theoretical Study. *Nano Lett.* **2011**, *11* (7), 2962–2967.

(202) Shenoy, V. B.; Johari, P.; Qi, Y. Elastic Softening of Amorphous and Crystalline Li–Si Phases with Increasing Li Concentration: A First-Principles Study. *J. Power Sources* **2010**, *195* (19), 6825–6830.

(203) van Duin, A. C.; Merinov, B. V.; Han, S. S.; Dorso, C. O.; Goddard Iii, W. A. ReaxFF Reactive Force Field for the Y-Doped BaZrO3 Proton Conductor with Applications to Diffusion Rates for Multigranular Systems. *J. Phys. Chem. A* **2008**, *112* (45), 11414–11422.

(204) Franger, S.; Cras, F. L.; Bourbon, C.; Rouault, H. LiFePO4 Synthesis Routes for Enhanced Electrochemical Performance. *Electrochem. Solid-State Lett.* **2002**, *5* (10), A231–A233.

(205) Yuan, L.-X.; Wang, Z.-H.; Zhang, W.-X.; Hu, X.-L.; Chen, J.-T.; Huang, Y.-H.; Goodenough, J. B. Development and Challenges of LiFePO4 Cathode Material for Lithium-Ion Batteries. *Energy Environ. Sci.* **2011**, *4* (2), 269–284.

(206) Chen, L.; Rago, N. L. D.; Bloom, I. D.; Shaw, L. L. New Insights into the Electrode Mechanism of Lithium Sulfur Batteries via Air-Free Post-Test Analysis. *Chem. Commun.* **2016**.

(207) Fujishima, A. Electrochemical Photolysis of Water at a Semiconductor Electrode. *nature* **1972**, *238*, 37–38.

VITA

Md Mahbubul Islam

265 Blue Course Dr. Apt 11C, State College, PA-16803. Cell: +1-814-880-2356

EDUCATION

12/2016	**Ph.D. in Mechanical Engineering**, CGPA (3.92/4.00) The Pennsylvania State University, University Park, PA
06/2011	**Master of Science in Mechanical Engineering** Bangladesh University of Engineering and Technology, Dhaka, Bangladesh.
03/2009	**Bachelor of Science in Mechanical Engineering,** *Salutatorian* Bangladesh University of Engineering and Technology, Dhaka, Bangladesh.

PROFESSIONAL EXPERIENCE

01/2012- Present	**Graduate Research Assistant**, Dept. of ME, Penn State, Advisor: Dr. Adri van Duin
06/2015 – 08/2015	**Summer Intern**, *RxFF_Consulting, LLC*, State College, PA
05/2014 - 08/2014	**Summer Intern**, *ExxonMobil Research & Engineering*, Mentor: Dr. Sumathy Raman
08/2011 - 12/2011	**Teaching Assistant**, Dept of ME, Penn State, University Park, PA
04/2009 - 08/2011	**Lecturer**, Dept. of Mechanical Engineering, BUET, Dhaka, Bangladesh

JOURNAL PUBLICATIONS

- **M M Islam**, G Kolesov, E Kaxiras, and A C T van Duin, "*eReaxFF: A pseudo-classical treatment of explicit electrons within reactive force field simulations*", J. Chem. Theory Comput. (**2016**)
- T P Senftle, S Hong, **M M Islam**, S B Kylasaf, Y Zheng, Y K Shin, C Junkermeier, R Engel-Herbert, M J Janik, H M Aktulga, T Verstraelen, A Grama, and A C T van Duin, "*The ReaxFF reactive force-field: development, applications, and future directions*", Nature Computational Materials (**2016**)
- **M M Islam**, C Zou, A C T van Duin, and Sumathy Raman, "*Interaction of hydrogen with iron and iron carbide interfaces: A ReaxFF molecular dynamics study*", Phys. Chem. Chem. Phys. (**2016**)
- **M M Islam**, A Ostadhossein, O Borodin, T Yeats, W W Tipton, R G Hennig, N Kumar, and A C T van Duin," *ReaxFF molecular dynamics simulations of the lithiated sulfur cathode materials*", Phys. Chem. Chem. Phys. (**2015**)
- **M M Islam**, V S Bryantsev**,** and A C T van Duin, " *ReaxFF reactive force field simulations on the influence of teflon on electrolyte decomposition during Li/SWCNT anode discharge in lithium-sulfur batteries*", J. of Electrochem. Soc. (**2014**)
- S Mojumder, A A Amin, and **M M Islam**, "*Mechanical properties of stanene under uniaxial and biaxial loading: A molecular dynamics study*"; J. of Appl. Phys. (**2015**)

AWARDS

- B.Sc with **Honors** in Mechanical Engineering
- Awarded **University Merit Scholarship** for all eight semesters during undergraduate studies
- Awarded **Dean's Scholarship** for all four years during undergraduate studies

EXTRA-CURRICULAR ACTIVITIES

- Selected as top five finalist team in the Dow Chemical sponsored Sustainability Innovation Student Challenge Award (SISCA), Penn State, November, 2013
- **Team Leader**, **Bangladesh Team**, 7th Asia Pacific ROBOCON Robot Contest 2008, Pune, India